Dimitar Iliev

Numerical Algorithms for Fluid Interaction with a Thin Porous Structure

Technische Universität Kaiserslautern

Fraunhofer ITWM

Fraunhofer-Institut für
Techno- und Wirtschaftsmathematik ITWM

Numerical Algorithms for Fluid Interaction with a Thin Porous Structure

Dimitar Iliev

FRAUNHOFER VERLAG

Kontakt:
Fraunhofer-Institut für Techno- und Wirtschaftsmathematik ITWM
Fraunhofer-Platz 1
67663 Kaiserslautern
Telefon +49 631/31600-0
Fax +49 631/31600-1099
E-Mail info@itwm.fraunhofer.de
URL www.itwm.fraunhofer.de

Bibliografische Information der Deutschen Nationalbibliothek
Die Deutsche Nationalbibliothek verzeichnet diese Publikation in der Deutschen Nationalbibliografie; detaillierte bibliografische Daten sind im Internet über http://dnb.d-nb.de abrufbar.
ISBN (Print): 978-3-8396-1152-4

D 386

Zugl.: Kaiserslautern, TU, Diss., 2016

Druck: Mediendienstleistungen des
Fraunhofer-Informationszentrum Raum und Bau IRB, Stuttgart

Für den Druck des Buches wurde chlor- und säurefreies Papier verwendet.

Fraunhofer-Informationszentrum Raum und Bau IRB
Postfach 80 04 69, 70504 Stuttgart
Nobelstraße 12, 70569 Stuttgart
Telefon 07 11 9 70-25 00
Telefax 07 11 9 70-25 08
E-Mail verlag@fraunhofer.de
URL http://verlag.fraunhofer.de

TECHNISCHE UNIVERSITÄT KAISERSLAUTERN

Numerical Algorithms for Fluid Interaction with a Thin Porous Structure

Dimitar Iliev

Vom Fachbereich Mathematik der Technishen Universität Kaiserslautern zur Verleihung des akademischen Grades Doktor der Naturwissenshaften (Doctor rerum naturalium, Dr. rer. nat.) genehmigte Dissertation

1. Gutachter: Prof. Dr. Oleg Iliev[a,b]
2. Gutachter: Prof. Dr. Svetozar Margenov[c]

[a] *Fraunhofer Institut für Techno- und Wirtschaftsmathematik (ITWM)*
[b] *Technische Universität Kaiserslautern*
[c] *Institute of Information and Communication Technologies, Bulgarian Academy of Sciences*

Datum der Disputation:
23. Juni 2016

D386

Abstract

The goal of this work is to develop an efficient numerical framework for the complex multiphysical problem of fluid interacting with a thin poroelastic structure. The Fluid - Porous Structure Interaction (FPSI) problems are relevant for a large class of physical problems in filtration. Simulation of filtration processes helps designers and manufacturers of filter elements. In some cases the deformation of the porous media can not be omitted. The filtration media is usually thin and by incorporating in our FPSI mathematical model dimensionality reducing models for the poroelastic part, namely plate and shell, we are able to further increase the efficiency of the FPSI framework. We develop an efficient numerical framework for FPSI using both advanced modeling techniques and advanced numerical simulation techniques. To numerically solve FPSI problems, we first formulate and discuss the mathematical models that govern the fluid flow through plain and porous media as well as the interaction between the fluid and the porous media. The interaction of the fluid with the porous media leads to deformation of the porous material. In order to reduce the computational time and to create an efficient framework, we describe approximate mathematical models that can be used for thin porous media with low permeability. We demonstrate the validity of the numerical scheme by comparison with existing analytical and numerical solutions of the approximate and the governing equations. We show numerical grid convergence as well as numerical convergence of the iterative scheme we use. We test the limits of the mathematical models in use and show particular cases when the reduced models can not be applied. We investigate the accuracy of the fluid solver and show high accuracy on grids with very few elements. We show very good agreement between the numerical simulation and physical experiments for a rectangular channel with a poroelastic plate. In this way we demonstrate the validity of the mathematical models and numerical techniques that we use. In the case of FPSI problem including poroelastic plate we demonstrate a speedup of up to 50 times in comparison with the model involving 3D poroelasticity. We also present simulations of complex and industrially relevant problems which illustrate the potential of the developed framework in solving industrial FPSI problems.

Acknowledgments

First and foremost I would like to express my deep gratitude to my supervisor Prof. Dr. Oleg Iliev for the guidance and support during the course of my PhD studies. This thesis would not have been possible without him directing me to the right area of research when needed. His expertise on numerous topics has helped me tremendously to find the path leading to the results achieved in my thesis.

I would also like to thank Dr. Ralf Kirsch for his help in numerous occasions. It was a pleasure to work together on software development, numerical simulations and articles. I have learned a lot from him.

My grateful thanks are also extended to Prof. Andro Mikelić, Prof. Josip Tambaca, Prof. Victor Calo, Prof. Michel Lance and Dr. Marc Michard. My discussions with Prof. Mikelić and Prof. Tambaca have improved my understanding on the asymptotic analysis of poroelastic plates and shells. My conversations with Prof. Victor Calo have helped me to understand the numerical locking effects in the FEM framework. My discussions with Prof. Lance and Dr. Michard during the comparison of physical experiments and numerical simulations have increased my understanding of the physical processes which take place during deformation of filtering media due to fluid flow through it. My work with them has also widened my knowledge on the experimental techniques used to measure fluid flow and material displacement in complex configurations.

Finally I wish to thank my family, friends and girlfriend for their support and encouragement through my studies.

Contents

Chapter 1

Introduction

The Fluid-Structure Interaction (FSI) is considered to be an essential class of multiphysics problems. A few of the areas where FSI finds application are aerospace engineering (see e.g. [1], [2] and [3]), cardiovascular research (see e.g. [4], [5] and [6]) and development of wind turbines (see e.g. [7], [8] and [9]). In general it is requiring significant computational resources and sophisticated algorithms. The need to improve the computation time for FSI problems is leading to the development of parallel algorithms like the ones presented in [10] and [11]. An example of complex numerical methods developed to tackle particular FSI problems is presented in [4] where Bazilevs and co-authors develop an isogeometric framework based on non-uniform rational B-splines (NURBS) in order to accurately capture complex domains and non-linear displacements. While a lot of research is dedicated to develop and analyze algorithms for FSI problems in the case of non-permeable structures, very little is done in the case of porous structures. The goal of this work is to create a framework of efficient numerical algorithms, which solves the complex multiphysical problem of fluid-porous structure interaction (FPSI).

In [12] Richer describes in details the different ways to solve the multiphysics system of equations in the case of FSI. One of the main difficulties is that a part of the equations is in Lagrangian formulation, while the other part is in Eulerian formulation. We use this terminology because with the deflection of the porous media the domain occupied by fluid is changing. With Lagrangian formulation we refer to the deformed configuration - the result of the displacement of the porous media. With Eulerian formulation we refer to the initial configuration of the domain before any displacements take place. This is a common notation in FSI problems. Even that the fluid equations are imposed in deformed configuration, we use Eulerian description (or specification) of the fluid flow. This means that the fluid velocity is defined as a function of space and not as a function of a particular fluid particle. The equations describing the flow and the displacements are linear. However, the FSI problem is nonlinear due to the fact that the shape of the structure in the FSI problems is a part of the solution, and

is not given a priori. For small size problems one can write a monolithic scheme and use a direct method at each of the iterations needed to solve the nonlinear problem. For larger problems and for cases when the coupling is not very strong, a partitioned (sequential) approach might be preferable. In such case one can reuse existing solvers for the elastic and for the flow subproblems, and impose the interface conditions via iterations between the subproblems. However, the sequential algorithms usually do not inherit the robustness of the monolithic approach. In general, the complexity of the FSI problems does not allow to develop algorithms which are in the same time very efficient and applicable to a wide class of FSI problems. In this situation, our approach is to concentrate on a class of FPSI problems and to develop a customized algorithm to efficiently solve the mathematical models describing this class of problems.

Such a mathematically challenging and practically relevant class of problems is filtration of solid particles out of fluid. Simulation of filtration processes helps designers and manufacturers of filter elements in the acceleration of the design process and in the optimization of the designed filters. In the case of non-deformable porous media, filtration-adapted algorithms and simulation software have proven their worth in industrial applications for years (see e.g. [13] and references therein). However, in many cases the deflection of the filtering medium can not be ignored. In this work we focus on FPSI in the case of fluid flowing through thin filtering medium with small permeability.

In the work of Badia and co-authors in [14] and the works of Bukač and co-authors in [15, 16], FPSI is considered in cases where the fluid flow is parallel to the free flow–porous media interface. Also one fluid–porous medium interface is considered. In many industrial oil filters (see e.g. Fig. 1.1) the so called dead end filtration takes place. In this case all of the fluid to be filtered goes trough the porous media. For porous media with low permeability the fluid flow near the porous structure is predominantly perpendicular to the plain fluid–porous media interface. Thus, for deformable as well as for non-deformable media in dead end filtration the Beavers-Joseph-Safmann boundary condition, used in these works, can not be applied. Additionally we have to consider at least two fluid-porous interfaces. The first task of this thesis is to formulate a set of mathematical models, along with boundary and interface conditions, which accurately represents the physical phenomenon of FPSI in dead end filtration. We are interested in the numerical simulation of physically relevant geometries. Thus, we aim to use mathematical models which can be practically applied in such configurations. For example a microscopic, pore scale, description of the porous structure is not applicable for the numerical simulation of a full-scale filter element.

In many of the industrial oil and air filters the filtration media is thin (see Fig. 1.1). For thin elastic bodies plate and shell models can be used in order to reduce the computational time of numerical simulations. The second task of this thesis is to incorporate plate and shell models in the FPSI mathematical models in order to increase the computational efficiency of the FPSI framework.

The third task of this thesis is to develop a robust customized numerical algorithm for the mathematical models describing the FPSI occurring in dead end filtration. This numerical algorithm should tackle the multiphysics nature of the FPSI phenomenon. As we consider macroscopic description of the porous media, we introduce a sharp interface between the region of plain fluid flow and the porous media. The characteristics of the fluid flow through this interface change rapidly and the interface is also changing with the deformation of the porous material. The numerical algorithm should resolve this interface accurately and should handle the rapid change of physical parameters through it. It also has to be feasible for practically relevant geometries and magnitudes of displacement.

We consider approximate plate and shell models in order to increase the numerical efficiency of the FPSI framework. It is very important to test the validity of this approximations in practically relevant geometries. The next task of this thesis is to validate the mathematical models in use. We aim to create a framework that can be used for simulation of a class of filters. Thus we aim not only to test the models validity for particular geometries, but also to find the limits of the models. In this way one will know when the mathematical models can be used to describe the FPSI phenomenon in filtration and when not. We also aim to validate the numerical framework against a physical experiment.

The FPSI framework consist of both the mathematical models and the numerical methods in use. Once we have tested the limits of the mathematical models, we set the task to validate the numerical methods.

As we aim to develop a practically useful framework, the last task of this thesis is to apply the FPSI framework to industrially relevant configurations. Our aim is to perform simulations of the filter media deformation in two physically relevant types of filters. The first part of this task is to consider a pleated filter, such as the left one in Fig. 1.1. The second part of this task is to consider a filter with a flat porous media such as the right one presented in Fig. 1.1.

After the clarification of the goals of this work let us discuss its structure. The thesis is organized as following:

In Chapter 2 we describe and discuss a set of mathematical models governing the physical phenomenon of fluid interacting with permeable porous media. We start with a description of the classical model of the Navier-Stokes equations for flow through plain region. Next we show and discuss two different models for flow through rigid porous media. We present the classical and widely used Darcy model as well as the more flexible Navier-Stokes-Brinkman system of equations. Further on we present the governing equations for flow through deformable porous media - the Biot's system. This model describes the deformations of a porous media due to fluid flow through it. This system also incorporates the backwards coupling - the effect of displacements of

Figure 1.1: left - an industrial oil filter for purification of the oil running through a car's engine, right - a virtual model of an oil filter for purification of the oil running through an automatic transmission

the porous media on the fluid flow. Later in Chapter 2 we discuss in detail the choice of interface conditions between the plain free flow region and the region occupied by the porous media. At the end of the chapter we summarize the full 3D model that describes the governing equations for FPSI.

In Chapter 3 we describe approximate models that can be used to improve the numerical efficiency of the framework. As the deflection itself takes very little time compared to the operation of the filter with already deformed media, we focus on the steady state solution of the system. This allows us to decouple the equation for the effective pressure from the equations of motion in Biot's system. Because of this we can be more flexible with the choice of the model describing the elastic behavior of the porous media. As in this work we focus on thin porous materials, we make use of poroelastic shell and plate models. We first describe an elastic shell model which can be used for a larger class of geometries as the porous material does not have to be initially flat. Later we present a poroelastic plate model which can be used for initially flat filtering media. In particular scenarios the use of the poroelastic plate model is preferable as it can further improve the numerical efficiency of the framework. At the end of this chapter we summarize the equations describing FPSI when plate or shell models are describing the elastic behavior of the porous media.

In Chapter 4 we present the numerical algorithm that we use in order to solve the mathematical models describing FPSI. Firstly we discuss how we solve the coupled system of equations. To describe the fluid motion in the plain and porous regions we use the Navier-Stokes-Brinkman system of equations. To describe the deformation

of the porous material we use poroelastic shell or plate models. We solve these two systems separately using different solvers. In order to impose the interface conditions between plain region and the porous region we use an iterative scheme running the two solvers sequentially. Later we present the discretization techniques used to solve the different systems of equations. We use the Finite Volume (FV) method with Multi-Point Flux Approximation (MPFA) to numerically solve the Navier-Stokes-Brinkman system of equations. For the numerical solution of the Biot's system and the poroelastic plate system of equations we use the Finite Element Method (FEM). In order to solve the elastic shell model numerically, we use a Finite Difference (FD) scheme and a FEM scheme. Further on we show the computational grids that we use in order to solve the different systems of equations. To solve efficiently the fluid flow system of equations we develop a special boundary- and interface- fitted quadrilateral grid. To avoid artificial numerical locking effects and to be able to use consistently the solutions of the 3D Biot's system as reference solutions, we use triangular prism elements for this model.

In Chapter 5 we perform a numerical validation of the mathematical models and the numerical techniques we use. As we use the approximate plate and shell models, we test the validity of the approximations for different geometries and boundary loads. To test the shell model we consider a circular arch and a poroelastic pleat. We examine the behavior of the shell model for uniform and non-uniform boundary loads. As a reference solution we use the solution of the 3D Biot's system. To test the validity of the poroelastic plate model we consider a thin porous disc. We compare the numerical solutions of the poroelastic plate model against the Biot's system for thin cylinders (disks) with different thicknesses under a range of boundary loads. Further on, we validate the accuracy of the numerical methods used to solve the Navier-Stokes-Brinkman system of equations. We very coarse consider grids as well as very fine grids. We compare the numerical results calculated on the different grids with the Darcy law prediction. We consider different domains, fluids with different viscosities and densities as well as medias with different permeabilities. To test the accuracy of the elasticity solver and the grid effects on the solution, we compare numerical simulations with an analytical solution. We also compare the computational efficiency of the poroelasic plate solver to the computational efficiency of the Biot's system solver. We test the convergence of the iterative scheme for a poroelastic pleat and for initially flat porous media. The first example incorporates the shell model. The second example let us test the convergence rate when the poroelastic plate model is being used. At the last section of this chapter we compare numerical simulations to a physical experiment. We first describe the experimental setup. Then we explain how the numerical framework that we develop can be used for parameter identification. Lastly we compare the numerical and physical experiments for different inlet velocities.

In Chapter 6 we present further applications of the numerical algorithms we develop. We show how taking the filter deformation into account can improve the simulations of filter elements. We demonstrate how the grid generation techniques we use can be

applied in the simulation of industrial filters. In the last section of this chapter we show how the poroelastic plate model can be used in complex geometries.

Finally, in Chapter 7 we summarize the contributions of this thesis.

Chapter 2

Mathematical models

In this chapter we discuss the models governing fluid flow through plain and porous media. We consider both rigid and deformable porous media. It is important to note that we aim to capture the two way coupling between the fluid flow and the deflection of the porous media. Meaning that we are interested both in the flow induced deformation and the effect of the deformation on the fluid flow.

Naturally the fluid flow equations are imposed in deformed configuration, while the elasticity equations are written in the initial configuration. For this reason we use different notations for variables and domains in the initial configuration and deformed configuration. Let us denote by Ω_p the region occupied by the porous filtering medium in non-deformed configuration, by Ω_f the region occupied by the pure fluid in non-deformed configuration, and by $\tilde{\Omega}_p$, $\tilde{\Omega}_f$ the respective domains in the deformed configuration. In Fig. 2.1 we present a schematic representation of the initial and the deformed domains. In this figure we consider a rectangular channel with an initially flat filtering media. Due to flow from the left to the right side of the channel the porous media is deflecting. Further on, let $\Omega = \Omega_p \cup \Omega_f = \tilde{\Omega}_p \cup \tilde{\Omega}_f$ be the total computational domain (which remains unchanged in the cases considered in this work), and $\partial\Omega$ be its (external) boundary. Finally, $\partial\tilde{\Omega}_{pf}$ stands for the interface between the plain and the porous media in deformed configuration. In Fig. 2.1 we demonstrate schematically the interfaces with red lines. In order to write the interface conditions on $\partial\tilde{\Omega}_{pf}$ we will use Ω_f as a reference domain. Let $T : \Omega_f \to \tilde{\Omega}_f$ (see Fig. 2.1) be a C^2 – diffeomorphism and $F = \nabla T$. In this work we denote vectors with bold symbols. The unknowns defined in deformed configuration we denote with tilde. The unknowns defined in the initial configuration we denote without tilde. Unknowns defined in the plain fluid region and in the porous region are equipped with the subscripts f and p, respectively.

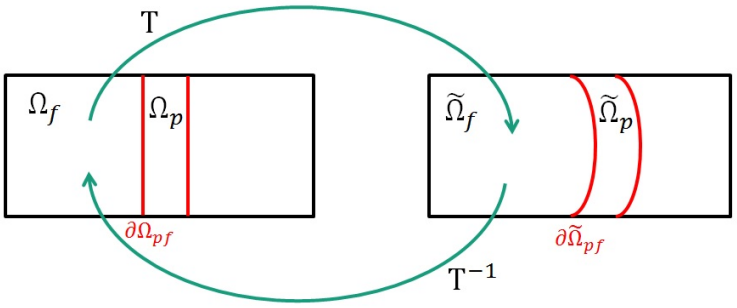

Figure 2.1: Schematic representation of the initial and the deformed configuration in FPSI

The following assumptions hold for the practical problem we are interested in, and are accounted for the model selection. The flow is single phase, incompressible, Newtonian and in a steady state. The filtering media is thin with constant thickness and it is an isotropic porous media (i.e. the permeability is a scalar and not a tensor). We consider the pore size of the porous media to be significantly smaller than the thickness of the media and thus homogenized (macroscale) models can be used to describe the flow through the porous media and its deformation. We do not consider problems with change in the topology of the domains of interest (e.g. no contact problems are considered). We also focus on the so called dead end filtration. In this case all the fluid to be filtered goes through the porous media. An alternative mechanism of filtration is the cross flow filtration when part of the flow is parallel to the filtering medium and never crosses it. We do not account for the effect of gravity as it is not relevant for the typical designs of dead end filters. We focus on laminar and not very fast flows, so that Darcy law holds for the flow through porous media. For the fluid we assume to be incompressible and Newtonian. The incompressibility of the fluid is not restrictive for filtration in the case of liquid-solid separation. Incompressibility can not be always considered in gas-solid separation. However. in many industrial applications air is being filtered under room temperature and atmospheric pressure and incompressibility can be considered. Motor oils (as well as other oils) could inhibit non-Newtonian behavior in low temperatures. However, we are interested in the long-term behavior of the filtering elements and the steady state of the system. In the long run the motor oil operates under normal and high temperatures.

2.1 Flow through plain fluid region

Let us first discuss the flow through the plain fluid region outside the filtering media. The incompressible laminar Navier-Stokes equations (see e.g. [17] or [18]) describe the fluid motion.

$$\rho\frac{\partial\tilde{\mathbf{v}}_f}{\partial t}+\rho\left(\tilde{\mathbf{v}}_f\cdot\nabla\right)\tilde{\mathbf{v}}_f-\nabla\cdot\left(\mu\nabla\tilde{\mathbf{v}}_f\right)=-\nabla\tilde{p}_f+-\nabla\tilde{f},\qquad\nabla\cdot\tilde{\mathbf{v}}_f=0\ \text{ in }\tilde{\Omega}_f.\tag{2.1}$$

The equations are written in deformed configuration. The notations $\tilde{\mathbf{v}}_f$ and $\tilde{p}_f$ stand for the fluid velocity and pressure in the region $\tilde{\Omega}_f$, respectively. With μ we denote the dynamic viscosity of the fluid and with ρ its density. The function f stands for the density of the external body forces. As we do not consider the effect of gravity, $f=0$ in our case. We are looking for the steady state solution of the considered FPSI problem. Thus, we can drop the time derivatives from the above equations (2.1). Under the described assumptions the Navier-Stokes equations take the following form

$$\rho\left(\tilde{\mathbf{v}}_f\cdot\nabla\right)\tilde{\mathbf{v}}_f-\nabla\cdot\left(\mu\nabla\tilde{\mathbf{v}}_f\right)=-\nabla\tilde{p}_f,\qquad\nabla\cdot\tilde{\mathbf{v}}_f=0\ \text{ in }\tilde{\Omega}_f.\tag{2.2}$$

In order to close the system of equations (2.2), we have to impose boundary conditions. In this section we discuss the boundary conditions on the external boundary of the domain $\partial\tilde{\Omega}_f=\tilde{\Gamma}_{wall}\cup\tilde{\Gamma}_{in}\cup\tilde{\Gamma}_{out}$. The interface conditions on $\partial\tilde{\Omega}_{pf}$ we discuss in detail in section 2.4. We distinguish between three different parts of the external boundary $\partial\tilde{\Omega}_f$. With $\tilde{\Gamma}_{in}$ we denote an inlet, with $\tilde{\Gamma}_{out}$ an outlet and with $\tilde{\Gamma}_{wall}$ a supporting structure. As the boundaries $\tilde{\Gamma}_{in}$, $\tilde{\Gamma}_{out}$ and $\tilde{\Gamma}_{wall}$ have different physical meanings there is no overlapping between any of this regions.

When we consider simulations of a filter element, the supporting structure is the housing of the filter element. When we perform simulations of an experimental setup, the supporting structure consists of the walls of an optically clear channel. We consider supporting structures made out of metal, plastic or other composite materials. These are the materials used in the production of industrial filters and in test–benches. In addition we consider the casings to have no special coating and no specially generated micro- or nano- structure that would give it special wetting properties or roughness. For this reason on $\tilde{\Gamma}_{wall}$ we impose the no-penetration, no-slip boundary condition

$$\tilde{\mathbf{v}}_f=0\ \text{ on }\tilde{\Gamma}_{wall}.\tag{2.3}$$

In this work we focus on the simulation of a part of a filtering system, mainly the filter element. For example in the case of a car, the filtering system is circulating the motor oil using a pump of some kind. Usually the pump is placed not directly in front of a filter element, but it is connected to the filter element via a tube or a system of tubes. In this case we can neglect the direct effect of the pump on the flow. Thus, we consider a part of the tube as an inlet for the filter element. If we choose the very end of the tube to be the inlet for our simulation we should impose Poiseuille flow as an inlet condition. We chose a slightly different approach. We take the inlet on

a distance from the filter element and impose a given constant velocity as boundary condition on $\tilde{\Gamma}_{in}$.

$$\tilde{\mathbf{v}}_f = -v_{in}\tilde{\mathbf{n}} \quad \text{on } \tilde{\Gamma}_{in}. \tag{2.4}$$

We denote by v_{in} the given magnitude of the inlet velocity. We use $\tilde{\mathbf{n}}$ to denote the outer normal vector with unit length on the boundary of the domain. In this case the domain of interest is $\tilde{\Omega}_f$ and the boundary of interest is $\tilde{\Gamma}_{in}$. As in the tube we have channel flow, Poiseuille flow develops in this region. As long as the inlet is far enough from the filtering media, the boundary conditions (2.4) have no negative effects on the overall accuracy of the simulation.

On the outlet $\tilde{\Gamma}_{out}$ we impose the 'do-nothing' boundary condition (see [19])

$$\mu\frac{\partial\tilde{\mathbf{v}}_f}{\partial\tilde{\mathbf{n}}} - \tilde{p}_f\tilde{\mathbf{n}} = 0 \quad \text{on } \tilde{\Gamma}_{out}. \tag{2.5}$$

In equation (2.5), $\tilde{\mathbf{n}}$ is once again the outer unit normal vector (this time for the boundary $\tilde{\Gamma}_{out}$). We consider outlets far enough from the filtering media, so that the flow is laminar and stable near this boundary. Therefore, the velocity vector $\tilde{\mathbf{v}}_f$ does not change in the normal direction of $\tilde{\mathbf{n}}$ and the 'do-nothing' boundary condition simplifies to the following equations

$$\tilde{p}_f = 0, \qquad \frac{\partial\tilde{\mathbf{v}}_f}{\partial\tilde{\mathbf{n}}} = 0 \quad \text{on } \tilde{\Gamma}_{out}. \tag{2.6}$$

We consider a plain flow region next to a deformable porous media. Therefore, the domain $\partial\Omega_f$ as well as the interface $\partial\Omega_{pf}$ change with the deflection of the porous media. On the other side we consider the filter casing to be rigid and we focus on particular inlet and outlet regions. Thus the external boundary of the domain does not change with the deformation of the porous media:

$$\tilde{\Gamma}_{wall} \equiv \Gamma_{wall}, \quad \tilde{\Gamma}_{in} \equiv \Gamma_{in}, \quad \tilde{\Gamma}_{out} \equiv \Gamma_{out}. \tag{2.7}$$

2.2 Fluid flow through rigid porous media

Before describing models for flow through deformable media, we first describe models for flow through rigid porous media ($\tilde{\Omega}_p \equiv \Omega_p$). We are interested in simulations of a

whole filter element. Modeling the flow through porous media on micro level resolving the filter fibers (or other micro structure) would be extremely computationally expensive. Instead of resolving the micro structure, we use a homogenized macro-scale model. Under the assumptions that we have for the flow and the porous media, the flow through saturated porous media is usually described by the Darcy equation coupled with the continuity equation (see [20]):

$$\tilde{\mathbf{v}}_p = -\frac{K}{\mu}\nabla\tilde{p}_p, \qquad \nabla\cdot\tilde{\mathbf{v}}_p = 0 \ \text{ in } \tilde{\Omega}_p \equiv \Omega_p. \tag{2.8}$$

The notations $\tilde{\mathbf{v}}_p$ and $\tilde{p}_p$ stand for the effective fluid velocity and the effective pressure in the porous media, respectively. We use μ to denote the effective fluid viscosity. The notation K stands for the permeability of the porous media. The coefficient K is only dependent on the microstructure of the porous media. In the most general case the permeability is a tensor. As we focus on isotropic materials, K is scalar in our studies. For the numerical examples presented in this paper we consider uniform materials and the permeability is considered to be constant within the porous media. Instead of focusing on the permeability of the porous media one can also consider the inverse coefficient K^{-1}. This coefficient also has a physical meaning - the resistivity of the porous material. The more permeable a material is, the less resistance it has for the fluid flowing through it.

Although the Darcy equation is widely used in filtration problems, this model has its limitations. One particular limitation is on the type of boundary conditions one can use. As we focus on dead end filtration problems, the porous media has an area where fluid is entering the media and another area where it is leaving it. On these areas particular flow, fluid pressure or a combination of them should be prescribed. In order for the filtering media not to be washed away by the fluid, it has to be fixed on some other areas. On the latter areas the filtering media is glued (or fixed in another way) to a wall and then no-slip Dirichlet type of boundary conditions are to be prescribed for the fluid velocity. Even for simple geometry like a cube, imposing these different boundary conditions would result in a mathematical problem with no solution if the Darcy model is used. If periodic or symmetry boundary conditions are prescribed instead of the no-slip boundary conditions such a problem has a solution. In this case linear pressure and constant velocity would satisfy the system (2.8). For dead end filtration problems the requirements for boundary conditions are different and one can not satisfy all of the boundary conditions with such a low order model. For such cases or when the filtering media is highly porous, the Navier-Stokes-Brinkman system of equations (see [20]) could be used instead of the Darcy system of equations 2.8.

$$\rho\frac{\partial\tilde{\mathbf{v}}_f}{\partial t}+\rho\left(\tilde{\mathbf{v}}_f\cdot\nabla\right)\tilde{\mathbf{v}}_f-\nabla\cdot(\mu\nabla\tilde{\mathbf{v}}_f)+\bar{\mu}K^{-1}\tilde{\mathbf{v}}_p = -\nabla\tilde{p}_f+-\nabla\tilde{f}, \quad \nabla\cdot\tilde{\mathbf{v}}_f = 0 \ \text{ in } \Omega. \tag{2.9}$$

Note, that the Navier-Stokes-Brinkman system of equations (2.9) could be used to describe the motion of the fluid not only in the porous domain $\tilde{\Omega}_p$, but in the whole domain of interest Ω as long as one specifies the permeability also in the free flow domain $\tilde{\Omega}_f$. As in the free flow region there is no flow resistivity, we set the resistivity K^{-1} as follows:

$$K^{-1} = \begin{cases} 0 & \text{in } \tilde{\Omega}_f, \\ \text{const} \neq 0 & \text{in } \tilde{\Omega}_p. \end{cases} \tag{2.10}$$

By $\bar{\mu}$ we denote the effective fluid viscosity in the porous region. In some studies different values are used for the effective fluid viscosity $\bar{\mu}$ and the fluid viscosity μ (e.g. [21]). However, the numerical studies by Iliev and Laptev in [22] show that the use of effective viscosity $\bar{\mu} = \mu$ is preferable for filtration problems. We use $\tilde{f}$ to denote the density of the external mass forces acting to the system. As we do not take into account the effect of gravity, $\tilde{f} = 0$. As in section 2.1, we consider the steady state of the system and we drop the time derivatives from the equation (2.9). Taking into account the later remarks, the Navier-Stokes-Brinkman system of equations simplifies to:

$$\rho\left(\tilde{\mathbf{v}}_f \cdot \nabla\right)\tilde{\mathbf{v}}_f - \nabla \cdot (\mu \nabla \tilde{\mathbf{v}}_f) + \mu K^{-1} \tilde{\mathbf{v}}_p = -\nabla \tilde{p}_f, \qquad \nabla \cdot \tilde{\mathbf{v}}_f = 0 \ \text{ in } \Omega. \tag{2.11}$$

It should be noted that for filtration problems the term μK^{-1} is usually very large within the porous media. The permeability is often of order 10^{-10} or less. Therefore the above system of equations (2.11) can be considered as a perturbation of the Darcy system of equations (2.8), where the viscous and convective terms are omitted.

The boundary conditions that we impose to the system (2.11) are the same as in the previous section 2.1. On the inlet we impose the given velocity boundary condition (2.4), on the outlet we impose the 'do-nothing' boundary condition (2.6) and the wall of the supporting structure we impose the no-penetration and no-slip boundary condition (2.3). The only difference is that in this section we extend the domain of interest from $\tilde{\Omega}_f$ to Ω. Naturally the boundary Γ_{wall} extends with the boundary of $\tilde{\Omega}_p$ which is in contact with the case of the filter element.

2.3 Deformable porous media:fluid flow and poroelasticity

In the works [24] and [25] Biot has derived the consolidation theory of poromechanics. He has done that by taking two different systems of equations describing different phenomenons and creating one coupled system describing both of these behaviors.

Biot has used the linear theory of elasticity to describe the deformations of porous media and the Darcy equation to describe flow in porous region. The quasi steady state Biot's system of equations reads as follows

$$-\text{ div } \sigma_p = -\hat{\mu}\Delta \mathbf{u}_p - \left(\hat{\lambda} + \hat{\mu}\right) \nabla \text{ div } \mathbf{u}_p + \alpha \nabla p_p = 0 \text{ in } \Omega_p, \tag{2.12}$$

$$\frac{\partial}{\partial t}\left(\beta p_p + \alpha \text{ div } \mathbf{u}_p\right) - \frac{K}{\mu}\Delta p_p = 0 \text{ in } \Omega_p. \tag{2.13}$$

The stress tensor σ_p has the following form:

$$\sigma_p = 2\hat{\mu}\left(\nabla \mathbf{u}_p + (\nabla \mathbf{u}_p)^T\right) + \left(\hat{\lambda} \text{ div } \mathbf{u}_p - \alpha p_p\right) \mathrm{I}. \tag{2.14}$$

With $\mathbf{u}_p$ we denote the vector field of effective displacements in the porous region and with p_p the effective pore pressure. The parameters $\hat{\lambda}$ and $\hat{\mu}$ are the first and second Lamé constants, α is the effective stress coefficient and β is the inverse of the Biot's modulus. It is important to note that this system describes the deformation in the porous solid body due to the flow through it and due to external forces, as well as the effects of the movement of the solid structure to the fluid flow.

As we consider the stationary solution of the system, the time derivative in the equation (2.13) vanishes. Thus, the equation (2.13) simplifies to:

$$\triangle p_p = 0 \text{ in } \Omega_p. \tag{2.15}$$

In addition to the equations (2.12) and (2.15) one should also add closing boundary or interface conditions. In this work we consider two setups for a deformable porous media. In one scenario we consider an isolated porous media. In the other case we consider the porous media as a part of a numerical simulation of a filter during filtration regime.

Let us first consider the case of an isolated porous media. We use this setup to compare reduced models for the displacement of porous media against the governing Biot's system. In this case all of the boundaries $\delta\Omega_p$ of the domain Ω_p are external and we set boundary conditions. We consider part of the media to be clamped and no flow to go through this part of the boundary Γ_{wall}:

$$\mathbf{u}_p = 0, \quad \frac{\partial p_p}{\partial \mathbf{n}} = 0 \text{ on } \Gamma_{wall}. \tag{2.16}$$

On the other part of the boundary $\Gamma_{pf} \equiv \delta\Omega \setminus \Gamma_{wall}$ we allow deformation. On Ω_{pf} we prescribe the normal component of the stress tensor (a particular load) as well as the effective pressure:

$$\sigma_p \cdot \mathbf{n} = \mathbf{S}(\mathbf{x}), \quad p_p = P(\mathbf{x}) \text{ on } \Gamma_{pf}. \tag{2.17}$$

In our numerical studies of isolated porous media we consider $\mathbf{S}(\mathbf{x})$ and $P(\mathbf{x})$ to be a given constant or to be piecewise-constant.

The conditions (2.16) and (2.17) are only one class of boundary conditions that is closing the system of equations (2.12), (2.15). We choose this particular type of boundary conditions as we can express the boundary and interface conditions in the case of FPSI in the same manner. The boundary condition (2.16) represents strong clamping (or gluing) to a wall. We use this boundary condition on the part of the filter strongly clamped to the filter casing. In the case of filter simulation, Γ_{pf} is the porous media-free flow interface $\delta\Omega_{pf}$. In the next section 2.4 we discuss in detail how to set $\mathbf{S}(\mathbf{x})$ and $P(\mathbf{x})$ in the case of FPSI ensuring conservation of mass and conservation of momentum.

2.4 Interface conditions

The choice of interface conditions between flow in a plain region and flow in homogenized (macroscopic) porous media is a topic of continued research. Hanspal and co-authors in [26] and Showalter in [27] consider cross-flow filtration. In this case, in addition to the continuity of the velocity and the normal component of the stress tensor, the Beavers-Joseph-Safmann conditions can be applied. In [28] Cao and co-authors use more general Beavers-Joseph type conditions for a dynamic system. However the generalized Beavers-Joseph and the Beavers-Joseph-Safmann conditions can be applied only in the case of flow parallel to the fluid-porous media interface. In this case it produces discontinuity of the velocity for cross-flow filtration regimes. In [29] Bars and Worster formulate a single domain approach for analytically trackable cases in order to avoid this discontinuity. Their approach, however, is limited to simple geometries. In [30] Marciniak-Czochra and Mikelić suggest a different type of interface conditions imposing jump of the pressure. With Carraro and Goll in [31] they show numerical results for a cross-flow and specific 2D porous media consisting of periodical circular or ellipsoidal obstacles. When ellipsoidal obstacles are used the authors show the need of using a pressure jump interface law in the homogenized macroscopic models. However, for isotropic porous mediums such as the ones we consider, the pressure is continuous along the plain flow-porous medium interface (see [30]).

For the case of deformable porous media, much less research has been done. In the work of Badia and co-authors in [14] and the works of Bukač and co-authors in [15, 16],

FPSI is considered in cases where the fluid flow is parallel to the free flow–porous media interface. Also only one fluid–porous medium interface in considered. These works follow the classical approaches for fluid–porous structure interface. As interface conditions in addition to the continuity of the velocity of the fluid and continuity of the normal component of the stress tensor, Beavers-Joseph-Safmann conditions are applied. For dead end filtration the porous medium has two separate interfaces of inflow and outflow of fluid. On these interfaces and inside the porous medium the flow is predominantly normal to the interfaces. Thus, for deformable as well as for non-deformable media in dead end filtration the Beavers-Joseph-Safmann can not be applied. In addition to the continuity of the fluid velocity and the normal component of the stress tensor, we impose continuity of the fluid pressure.

We define the Navier-Stoke-Brinkman system of equations (2.11) describing the fluid flow in the deformed configuration. The porous medium displacement in Biot's model (2.12) is defined in the initial configuration. In order to write the interface conditions for these two models defined in different coordinates, we use the Arbitrary Lagrangian-Eulerian (ALE) approach (see e.g. [12]). We make use of the transformation T and more specifically its inverse T^{-1} to write the interface conditions in the initial configuration.

The first of the interface conditions that we impose is the conservation of mass. For dead end filtration this condition is satisfied when the normal component of the fluid velocity is continuous along the interface between the plain flow region and the porous medium $\partial\tilde{\Omega}_{pf}$. Let $\overline{\mathbf{v}}_f$ be the fluid velocity in the plain fluid region mapped in the initial domain Ω_f

$$\overline{\mathbf{v}}_f = T^{-1}\left(\tilde{\mathbf{v}}_f\right). \tag{2.18}$$

Let $\mathbf{v}_p$ be the fluid velocity in the porous domain Ω_p. From the assumption of Darcy law in the porous domain we have:

$$\mathbf{v}_p = -\frac{K}{\mu}\nabla p_p. \tag{2.19}$$

Using the equations (2.18) and (2.19) we can write the mass conservation interface condition on the interface in the non-deformed configuration $\partial\Omega_{pf}$:

$$-\frac{K}{\mu}\nabla p_p \cdot \mathbf{n} = \overline{\mathbf{v}}_f \cdot \mathbf{n} \quad \text{on } \partial\Omega_{pf}. \tag{2.20}$$

To satisfy the continuity of the momentum we impose continuity of the normal component of the stress tensor. Once again we make use of the ALE approach to write

the equation in the initial configuration. In order to do this we use the transformation T^{-1} to map the fluid stress tensor σ_f from the deformed domain $\tilde{\Omega}_f$ to the initial domain Ω_f. Let us use the following notations

$$\overline{p}_f = T^{-1}\left(\tilde{p}_f\right), \quad \overline{\sigma}_f = T^{-1}\left(\tilde{\sigma}_f\right). \tag{2.21}$$

Using these notations we have:

$$\overline{\sigma}_f = \overline{p}_f \mathrm{I} + \mu\left(\nabla \mathbf{v}_f F^{-1} + F^{-T} \nabla \mathbf{v}_f{}^T\right). \tag{2.22}$$

The continuity of the normal component of the stress tensor in the initial configuration reads:

$$\sigma_p \cdot \mathbf{n} = \overline{\sigma}_f \cdot \mathbf{n} \text{ on } \partial\Omega_{pf}. \tag{2.23}$$

The last interface condition that we impose is the continuity of the pressure

$$p_p = \overline{p}_f \text{ on } \partial\Omega_{pf}. \tag{2.24}$$

The equations (2.23) and (2.24) are consistent with the form of the equation (2.17). Thus in the case of FPSI, the $\mathbf{S}(\mathbf{x})$ and $P(\mathbf{x})$ should be chosen in the following manner:

$$\mathbf{S}(\mathbf{x}) = \overline{\sigma}_\mathbf{f} \cdot \mathbf{n}, \quad \mathbf{P}(\mathbf{x}) = \overline{\mathbf{p}}_\mathbf{f}. \tag{2.25}$$

Note that for filtering mediums with small permeability for some geometries (for example initially flat filters in large cages) the velocity is nearly constant along the interface $\partial\tilde{\Omega}_{pf}$. In such cases the pressure $\overline{p}_f$ is dominating in the fluid stress tensor $\overline{\sigma}_f$ and the equations (2.23) and (2.24) become nearly identical.

2.5 Summary

To summarize, the full FPSI model for simulation of a deformable filter consist of the Navier-Stokes-Brinkman system of equations (2.11), the Biot system of equations (2.12), (2.15) and the interface conditions (2.20), (2.23) and (2.24). The boundary conditions which we impose on the fluid flow are the inlet boundary condition (2.4),

the outlet boundary condition (2.6) and the no-slip boundary condition (2.3). Note that the interface conditions which we impose depend on the solutions of the Biot's system and the Navier-Stokes-Brinkman. Thus, the full model is a nonlinear system.

If we consider alone the Biot's system of equations, we impose the boundary conditions (2.16) and (2.17).

Chapter 3

Approximate models

Solving the 3D Biot model requires significant computational efforts. In many of the industrial oil and air filters the filtration media is thin (see Fig. 1.1). In such cases the porous structure can also be modeled as a poroelastic plate or a poroelastic shell in order to increase the computational efficiency of the FPSI framewok. In this chapter we describe how to incorporate poroelastic plates and shell in the FPSI framework. In subsection 5.2.2 we demonstrate how using such plate or shell models can substantially decrease the computational time.

Let us denote by h the thickness of the porous media. We consider h to be constant and also to be small comparing to a characteristic length L. For different domains we define the characteristic length in a different matter. In Chapter 2 all of the equations are defined on domains with the same dimensionality. If we consider Ω to be a 3D domain, all of its sub-domains are also 3D. If we consider a plain-strain example and a 2D cross-section of a 3D body, the domain Ω is 2D and all of its sub-domains defined so far are also 2D. In this chapter instead of defining the elasticity equations on the 3D/2D domain Ω_p, we define the elasticity equation on the 2D/1D middle surface $\hat{\Omega}_p$ of the domain Ω_p. As we consider dead end filtration the interface $\partial\Omega_{pf}$ consist of two separate parts - the one is a boundary in the inlet region and the other is boundary in the outlet region of the filter element. We define $\hat{\Omega}_p$ as the set of points in the domain Ω_p on equal distance from the two parts of the interface Ω_{pf}. Let $\mathbf{n}$ be a vector, normal to $\hat{\Omega}_p$. We can define the region of the porous media in the way $\Omega_p = \hat{\Omega}_p \times \left\{-\frac{h}{2}, \frac{h}{2}\right\}$. Let $\varepsilon = \frac{h}{L}$ be a small parameter. Therefore we consider a thin porous media.

3.1 Decoupling of the pressure equation in the Biot's system

Let us first discuss the Biot's model. As we are interested in the steady state of the system, the pressure equation simplifies to (2.15). For thin porous media we can analytically determine the effective pressure p_p. To illustrate this, let us consider a thin and flat porous media. Let us consider an orthonormal coordinate system O_{xyz} in which $\hat{\Omega}_p$ is in the plane $\{z = 0\}$. As the filtering media is thin, its z-dimension is small. Let us rescale the z-dimension by defining $z = \varepsilon\bar{z}$. Now in the coordinate system $O_{xy\bar{z}}$ the porous media has comparable dimensions in all directions. The equation (2.15) in $O_{xy\bar{z}}$ has the following form:

$$\frac{\partial^2 p_p}{\partial x^2} + \frac{\partial^2 p_p}{\partial y^2} + \frac{1}{\varepsilon^2}\frac{\partial^2 p_p}{\partial \bar{z}^2} = 0 \text{ in } \Omega_p. \tag{3.1}$$

If we multiply by ε^2 and perform asymptotic analysis on the equation (3.1), we drop all of the terms of order ε^2. This leads to p_p being a linear function in z-direction. In the general case, p_p is linear in the direction which is locally normal to $\hat{\Omega}_p$. This can be shown by rewriting equation (2.15) in local coordinates and performing the same asymptotic analysis. The boundary conditions (2.17) define p_p on Ω_{pf}. Taking into account the linearity of p_p, we can compute it analytically in terms of the given function $P(\mathbf{x})$. When considering FPSI, we can compute p_p in terms of the pressure p_f. Thus, the pressure decouples from the displacement in the poroelastic model. We use this decoupling to write an approximation of the Biot's system which we solve numerically significantly more efficient. Within the porous media the displacement and the fluid flow decouple. However, in the FPSI framework both the displacement and the fluid flow in the porous media are coupled to the fluid velocity in the plain fluid region. Thus, the fluid flow and porous media displacement in the porous media are not independent in the FPSI problem.

3.2 Poroelasticity: shell model

A rigorous derivation of the poroelastic flexural three-dimensional shell model from the Biot's system through asymptotic analysis was done by Mikelić and Tambača in [42]. However, as we are interested in the equilibrium state of the system and the elastic part from the Biot's system decouples from the flow part, we are free to choose a different type of shell model to represent the displacements in the porous media. Instead of flexural shell we use a Naghdi type (see [32] and [33]) of shell described in detail by Zang in [34]. This type of shell describes not just the normal and tangential displacements w and u but also the rotation θ of the line perpendicular to the middle

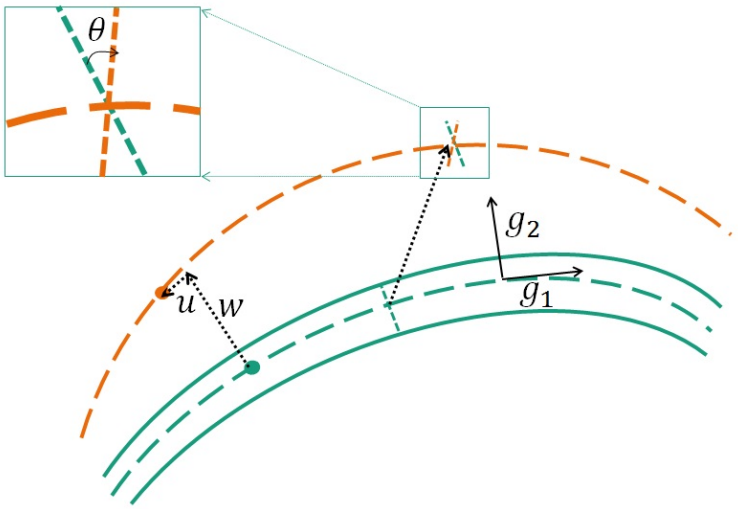

Figure 3.1: Normal and tangential displacement as well as the rotation of a cross section in the framework of cylindrical elastic shell

surface. Without the Kirchoff hypothesis of small rotation θ this model could be used for a wider area of applications. The Naghdi-type shell model also accounts not just for the flexural energy, but also for the membrane and shear energy. This results in membrane and shear deformation along with the flexural deflection - see Fig. 3.2. In this work we present the cylindrical elastic shell, also referred to as cylindrical elastic beam. It is worth noting that poroelastic beam models (without them being cylindrical) have also been derived. In this more simple case even large deformation cases are considered. For example in [35] Li and co-authors derive a mathematical model for large deflection of poroelastic beams. Further work was done by Yang and Wang in [36]. Going back to the cylindrical poroelastic shell model let θ be the rotation of the line perpendicular to the middle surface, u be the tangential component of the displacement of a point of the middle surface and w be the normal component of this displacement (see Fig. 3.1). Following the derivations in [34] for shorter notations let us define the functions ρ, γ and τ the following way:

$$\rho(\theta,u,w)=\theta'+b\left(u'-bw\right),\quad \gamma(u,w)=u'-bw,\quad \tau(\theta,u,w)=\theta+bu+w'. \tag{3.2}$$

Using the above notations, the weak formulation of the Naghdi elastic shell model presented in [34] is the following:

$$\begin{aligned}&\frac{1}{3}h^2\left(2\mu+\lambda^*\right)\int_0^L\rho(\theta,u,w)\,\rho(\phi,\psi,\zeta)\,dx\\ &+\left(2\mu+\lambda^*\right)\int_0^L\gamma(u,w)\,\gamma(\psi,z)\,dx+\frac{5}{6}\mu\int_0^L\tau(\theta,u,w)\,\tau(\phi,y,\zeta)\,dx\\ &=f_0(\phi,\psi,\zeta)+h^2f_1(\phi,\psi,z),\forall(\phi,\psi,\zeta)\in H.\end{aligned} \tag{3.3}$$

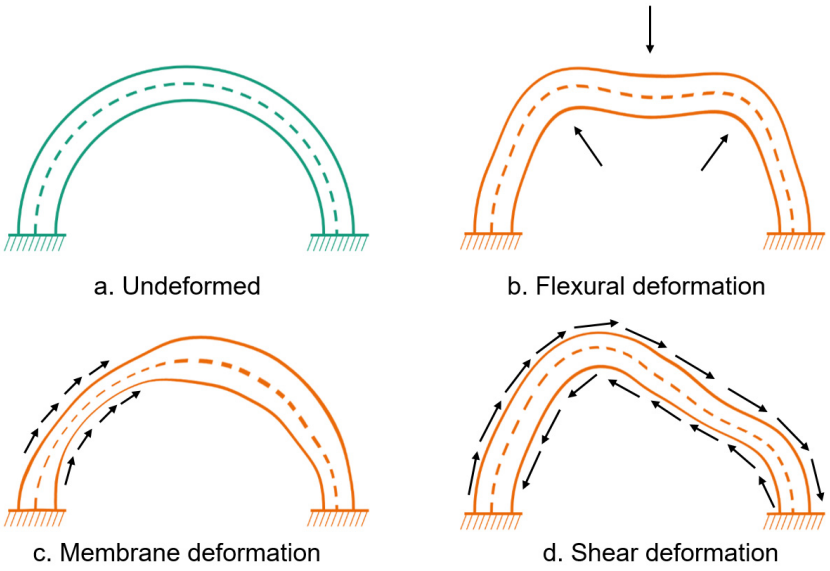

Figure 3.2: Schematic illustration of flexural, membrane and shear deformation

The first, second and third integral terms in the left hand side of the equation (3.3) are respectively the flexural, membrane and shear energies. The functions ϕ , ψ and ζ are test functions respectively for the rotation θ and the displacements u and w. The test functions are defined in the Hilbert space $H = \left[H_0^1(0,L)\right]^3$. For more details see [34]. The right hand side is defined by the loading functionals f_0 and f_1 :

$$\begin{aligned} f_0(\phi,\psi,\zeta) &= \frac{5}{6}\int_0^L p_o^1 \tau(\phi,\psi,\zeta)\,dx - \frac{\lambda}{2\mu+\lambda}\int_0^L p_o^2 \gamma(\psi,\zeta) \\ &\quad + \int_0^L \left[\left(p_e^1 + q_a^1 - 2bp_0^1\right)\psi + \left(p_e^2 + q_a^2 + p_0^{2\prime}\right)\zeta\right] dx, \\ f_1(\phi,\psi,\zeta) &= -\frac{1}{3}\int_0^L \left[\left(bq_a^1 + 3bp_e^1 - q_m^1\right)\phi + bq_m^1\psi + bq_m^2\zeta\right] dx \\ -\frac{\lambda}{3(2\mu+\lambda)}&\int_0^L \left(p_e^2 + bp_o^2\right)\rho(\phi,\psi,\zeta)\,dx - \frac{1}{6}b\int_0^L p_e^1\tau(\phi,\psi,\zeta)\,dx. \end{aligned} \tag{3.4}$$

With b we denote the curvature of the middle surface of the porous media and with h its thickness. In the case of cylindrical shell we choose the characteristic length L to be the length of middle line. That is why we use the letter L to define the middle surface on the reference domain $[0,L]$. To define the boundary conditions for the poroelastic displacements p_0^2 and p_e^2, we distinguish between the interfaces in the inlet and outlet region $\partial\Omega_{pf} = \partial\Omega_{pf+} \cup \partial\Omega_{pf-}$. We use the notations $\sigma_{f+} = \sigma_f$ on $\partial\Omega_{pf+}$, $\sigma_{f-} = \sigma_f$ on $\partial\Omega_{pf-}$, $\mathbf{n}_+ = \mathbf{n}$ on $\partial\Omega_{pf+}$ and $\mathbf{n}_- = \mathbf{n}$ on $\partial\Omega_{pf-}$. Let $\mathbf{t}_+$ and $\mathbf{t}_-$ be unit vectors perpendicular to $\mathbf{n}_+$ and $\mathbf{n}_-$ respectively. Also let the couples $\mathbf{n}_+, \mathbf{t}_+$ and

$\mathbf{n}_-, \mathbf{t}_-$ be positively oriented. Let us write the normal component of the stress tensor in local coordinates on the inlet and outlet interfaces.

$$\begin{aligned}\sigma_{f+}\cdot\mathbf{n}_+ &= f_n^+\frac{1}{1-bh}\mathbf{n}_+ + f_t^+\frac{1}{1-bh}\mathbf{t}_+,\\ \sigma_{f-}\cdot\mathbf{n}_+ &= f_n^-\frac{1}{1+bh}\mathbf{n}_- + f_t^-\frac{1}{1+bh}\mathbf{t}_-.\end{aligned} \tag{3.5}$$

Using the local coordinates we define p_0^2 and p_e^2 in the following way:

$$p_0^2 = \frac{f_n^+ - f_n^-}{2}, \quad p_e^2 = \frac{f_n^+ + f_n^-}{2h}. \tag{3.6}$$

The functions $q_{\{a,m\}}^{\{1,2\}}$ are rescaled integrals of the body force densities acting on the elastic structure (for more details see [34]). In dead end filtration the gravity effects are usually negligible and we consider in our studies $q_{\{a,m\}}^{\{1,2\}} = 0$. In [34] for the derivation of the Naghdi elastic shell model (3.3) it is assumed for the functions $p_{\{o,e\}}^{\{1,2\}}$ and $q_{\{a,m\}}^{\{1,2\}}$ to be indebpendent of the thickness of the media h. As we do not consider mass forces, the assumption is valid for $q_{\{a,m\}}^{\{1,2\}}$. The assumption on the boundary forces implies small forces which would lead to small deformations. In chapter 5 we test numerically how restrictive are the assumptions of small forces and thin porous media for deformable porous filters.

To build a discretization of the equations (3.3) we use the strong formulation of the problem. To obtain the strong formulation we consider first the set of test functions $\{(\phi,0,0)\in H\}$.

$$\begin{aligned}&\frac{1}{3}h^2\left(2\mu+\lambda^*\right)\int_0^L\left(\theta'+bu'-b^2w\right)\phi' dx + \frac{5}{6}\mu\int_0^L\left(\theta+bu+w'\right)\phi dx\\ &= \frac{5}{6}\int_0^L p_o^1\phi dx - \frac{1}{3}h^2\int_0^L 3bp_e^1\phi dx - \frac{\lambda}{3}\left(2\mu+\lambda\right)h^2\int_0^L\left(p_e^2+bp_o^2\right)\phi' dx\\ &\qquad -\frac{1}{6}h^2\int_0^L bp_e^1\phi dx.\end{aligned} \tag{3.7}$$

We perform integration by parts on the terms with the derivative ϕ'.

$$\begin{aligned}\int_0^L\left(\theta'+bu'-b^2w\right)\phi' dx = &\left[\left(\theta'+bu'-b^2w\right)\phi\right]\Big|_0^L\\ &-\int_0^L\left(\theta'+bu'-b^2w\right)'\phi dx,\end{aligned} \tag{3.8}$$

$$\int_0^L \left(p_e^2 + bp_o^2\right)\phi' dx = \left[\left(p_e^2 + bp_o^2\right)\phi\right]\Big|_0^L - \int_0^L \left(p_e^2 + bp_o^2\right)'\phi dx. \tag{3.9}$$

As we have chosen the test space H such that $\phi(0) = \phi(L) = 0$, the first terms in the right-hand side of the equations (3.8) and (3.9) drop out. Using (3.8) and (3.9) the equation (3.7) is equivalent to

$$\begin{aligned} -\frac{1}{3}h^2\left(2\mu+\lambda^*\right)\int_0^L \left(\theta' + bu' - b^2 w\right)'\phi dx + \frac{5}{6}\mu\int_0^L \left(\theta + bu + w'\right)\phi dx \\ = \frac{5}{6}\int_0^L p_o^1\phi dx - \frac{1}{3}h^2\int_0^L 3bp_e^1\phi dx + \frac{\lambda}{3}\left(2\mu+\lambda\right)h^2\int_0^L \left(p_e^2 + bp_o^2\right)'\phi dx \\ -\frac{1}{6}h^2\int_0^L bp_e^1\phi dx. \end{aligned} \tag{3.10}$$

As each function $\phi \in H$ satisfies the equation (3.10) we have

$$\begin{aligned} -\frac{1}{3}h^2\left(2\mu+\lambda^*\right)\left(\theta' + bu' - b^2 w\right)' + \frac{5}{6}\mu\left(\theta + bu + w'\right) = \frac{5}{6}p_o^1 - h^2 bp_e^1 \\ +\frac{\lambda}{3}h^2\left(2\mu+\lambda\right)\left(p_e^2 + bp_o^2\right)' dx - \frac{1}{6}h^2 bp_e^1. \end{aligned} \tag{3.11}$$

By performing the same procedure for the sets of functions $\{(0,\psi,0) \in H\}$ and $\{(0,0,\zeta) \in H\}$, from equation (3.3) we derive the following two equations

$$\begin{aligned} -\frac{1}{3}h^2\left(2\mu+\lambda^*\right)\left[b\theta' + b^2\left(u' - bw\right)\right]' - \left(2\mu+\lambda^*\right)\left(u' - bw\right)' \\ +\frac{5}{6}\mu\left(\theta + bu + w'\right)b = \frac{5}{6}p_o^1 b + \frac{\lambda}{2\mu+\lambda}p_o^{2\prime} + \left(p_e^1 - 2bp_o^1\right) + \\ \frac{\lambda}{3\left(2\mu+\lambda\right)}h^2\left(bp_e^2 + b^2 p_o^2\right)' - \frac{1}{6}b^2 h^2 p_e^1, \end{aligned} \tag{3.12}$$

$$\begin{aligned} -\frac{1}{3}h^2\left(2\mu+\lambda^*\right)\left(\theta' + bu' - bw\right)b^2 - \left(2\mu+\lambda^*\right)\left(u' - bw\right)b \\ -\frac{5}{6}\mu\left(\theta + bu + w'\right)' = -\frac{5}{6}p_o^{1\prime} + \frac{\lambda}{2\mu+\lambda}p_o^2 b + \left(p_e^2 + p_o^{2\prime}\right) \\ +\frac{\lambda}{3\left(2\mu+\lambda\right)}h^2\left(p_e^2 + bp_o^2\right)b^2 + \frac{1}{6}h^2\left(bp_e^1\right)'. \end{aligned} \tag{3.13}$$

The system of equations (3.11), (3.12) and (3.13) is the strong formulation of the Nagdi elastic shell model described in [34]. All of the ODE equations derived above are

defined on the open interval $(0, L)$. In order to close the system of the equations (3.11), (3.12) and (3.13) we have also to prescribe boundary conditions. As we have three equations of second order respectively for σ, u and w we should prescribe two boundary conditions for each of these parameters. We impose the following no displacement boundary conditions:

$$\theta(0) = \theta(L) = 0, \quad u(0) = u(L) = 0, \quad w(0) = w(L) = 0. \tag{3.14}$$

3.3 Poroelasticity: plate model

An heuristic derivation of a poroelastic plate model can be found in [39] and [40]. A mathematically rigorous derivation of this poroelastic plate model, based on asymptotic homogenization method, was later done by Mikelić in [41]. The rigorous poroelastic plate model reads as following:

$$D\Delta^2 w - \alpha B \Delta M = f_n^+ + f_n^- + \frac{h}{2}\nabla \cdot \left(f_{t1}^+ - f_{t1}^-, f_{t2}^+ - f_{t2}^-\right) \quad \text{in } \hat{\Omega}_p, \tag{3.15}$$

$$\left(\gamma + \frac{\alpha^2 B}{2G}\right)\frac{\partial}{\partial t}\left(p_p + \frac{2}{h}N\right) - \frac{K}{\mu}\frac{\partial^2 p_p}{\partial z^2} = \alpha B z \frac{\partial}{\partial t}\Delta w \quad \text{in } \Omega_p. \tag{3.16}$$

As in the elastic shell model, with w we denote the normal component of the displacement. In this model the Kirchoff hypothesis is assumed. This means that the rotation of the line, perpendicular to the middle surface, is negligibly small. It is also presumed the tangential displacement to be negligible in comparison to the normal displacement w. The functions $f_{t1}^{\pm}$, $f_{t2}^{\pm}$, $f_n^{\pm}$ are the effects of the boundary condition (2.17). The parameters D, B, N and M are defined as follows:

$$D = \frac{h^3 G}{6(1-\nu))}, \quad B = \frac{1-2\nu}{1-\nu}, \quad N = -\frac{1}{2}\int_{-\frac{h}{2}}^{\frac{h}{2}} p_p dz, \quad M = -\frac{1}{2}\int_{-\frac{h}{2}}^{\frac{h}{2}} p_p z dz. \tag{3.17}$$

The parameter D is the flexural rigidity of the plate, B is the elasticity parameter rescaling the Poisson's ratio ν, N is the effective stress resultant and M is the bending moment to the variation in the effective pore pressure across the plate thickness. In the above form of the poroelastic plate equations the deformation is defined on the middle surface $\hat{\Omega}_p$. However, the pressure equation is still defined in the full-dimensional domain Ω_p. The system (3.15), (3.16) is an integro-differential system of equations

and it is coupled both ways. The equation (3.15) has the bending moment M which is an integral term of the effective pressure p_p. The equation (3.16) incorporates the Laplacian of the deformation w. As we are interested in the steady-state solution of the above system, we can drop the terms with a time derivate in them. In this case the equation 3.16 has the following form:

$$\frac{\partial^2 p_p}{\partial z^2} = 0 \quad \text{in } \Omega_p. \tag{3.18}$$

Again as discussed in section 3.1, when we consider the steady state solution, the displacement and the pressure equations decouple and the pressure is a linear function with respect to z. Thus, we can calculate the integral in M using the interface conditions for the pressure:

$$M = -\frac{h^2}{24}\left(f_n^+ - f_n^-\right). \tag{3.19}$$

Thus the equation (3.15) becomes the biharmonic equation:

$$D\Delta^2 w = -\frac{h^2}{24}\alpha B\Delta\left(f_n^+ - f_n^-\right) + f_n^+ + f_n^- + \frac{h}{2}\nabla\cdot\left(f_{t1}^+ - f_{t1}^-, f_{t2}^+ - f_{t2}^-\right) \quad \text{in } \hat{\Omega}_p. \tag{3.20}$$

If the poroelastic medium is uniformly loaded and the functions $f_{\{n,t1,t2\}}^{\{+,-\}}$ are constant, the biharmonic equation further simplifies to:

$$D\Delta^2 w = f_n^+ + f_n^- \quad \text{in } \hat{\Omega}_p. \tag{3.21}$$

We would like to note that in the papers of Taber [39] and [40], the right-hand side of the above equation is the difference of the two loads instead of their sum. This is only due to the choice of the normal vectors on the boundaries of the porous media. We follow the notations of Mikelić and use normal vectors in direction outside of the porous region Ω_p. In this case the normal vectors on the two opposite sides of the porous media have opposite directions. Taber, however, poses the same boundary conditions using normal vectors in the direction of the z-axis. In this case the normal vectors on the two opposite sides of the porous media have the same direction. This difference in the orientation of the normal vectors leads to the different sign in the equation (3.21).

In order to close the biharmonic equation we need to prescribe boundary conditions to the system. For the purpose of different numerical experiments we impose different

boundary conditions. Let the boundary of the domain of interest $\hat{\Omega}_p$ consist of three parts - Γ_{weak}, Γ_{strong} and Γ_{symm}. We impose weak support boundary conditions on Γ_{weak}, strong support (clamping) boundary conditions on Γ_{strong} and symmetry boundary conditions on Γ_{symm}:

$$\begin{aligned} w = \frac{\partial^2 w}{\partial \mathbf{n}^2} = 0 \text{ on } \Gamma_{weak}, \\ w = \frac{\partial w}{\partial \mathbf{n}} = 0 \text{ on } \Gamma_{strong}, \\ \frac{\partial w}{\partial \mathbf{n}} = \frac{\partial^2 w}{\partial \mathbf{n}^2} = 0 \text{ on } \Gamma_{symm}. \end{aligned} \tag{3.22}$$

As the boundaries Γ_{weak}, Γ_{strong} and Γ_{symm} have different physical meanings, there is no overlapping of any of these regions. The weak support boundary condition allows for the plate to rotate. However, no displacements are allowed. This represents a hinge bond or a plate which is supported only from one side by a fixed body. The strong support boundary condition is the result of a plate being supported from two sides by fixed bodies. We use the symmetry condition to simulate a small part of a large filter element. In order to use Finite Elements Method (FEM) to numerically solve the biharmonic equation (3.21) we also consider the weak form of this equation:

$$D \int_{\hat{\Omega}_p} \Delta^2 w \zeta dz = \int_{\hat{\Omega}_p} \left(f_n^+ + f_n^- \right) \zeta dz, \forall \zeta \in \hat{H}. \tag{3.23}$$

The test function ζ is defined in the Hilbert space $\hat{H}$ where

$$\hat{H} = \left\{ z \in L^2 \left(\hat{\Omega}_p \right) : z = 0 \text{ on } \Gamma_0; \quad \frac{\partial z}{\partial \mathbf{n}} = 0 \text{ on } \Gamma_n; \quad \frac{\partial^2 z}{\partial \mathbf{n}^2} = 0 \text{ on } \Gamma_{n2} \right\}. \tag{3.24}$$

The boundary parts Γ_0, Γ_n and Γ_{n2} we define in the following way:

$$\Gamma_0 = \Gamma_{weak} \cup \Gamma_{strong}, \quad \Gamma_n = \Gamma_{strong} \cup \Gamma_{symm}, \quad \Gamma_{n2} = \Gamma_{weak} \cup \Gamma_{symm}. \tag{3.25}$$

Let us divide the equation (3.23) by the constant D and apply two times iteration by parts for the first integral. As on the boundary $\partial \hat{\Omega}_p$ the test functions along with their derivatives vanish, we are left with the following equation

$$\int_{\hat{\Omega}_p} \Delta w \Delta \zeta dz - \int_{\hat{\Omega}_p} \frac{f_n^+ + f_n^-}{D} \zeta dz = 0, \forall \zeta \in \hat{H}. \tag{3.26}$$

By applying integration by parts, we transfer some of the derivatives from the displacement w to the test function ζ. In the weak formulation of the poroelastic plate model, we impose the boundary conditions (3.22) weakly in the following matter:

$$\int_{\hat{\Omega}_p} \Delta w \Delta \zeta dz + C_1 \int_{\Gamma_0} w dz + C_2 \int_{\Gamma_n} \frac{\partial w}{\partial \mathbf{n}} dz + C_3 \int_{\Gamma_{n2}} \frac{\partial^2 w}{\partial \mathbf{n}^2} dz - \int_{\hat{\Omega}_p} \frac{f_n^+ + f_n^-}{D} \zeta dz = 0, \forall \zeta \in \hat{H}. \tag{3.27}$$

The constants C_1, C_2 and C_3 are penalization parameters.

3.4 Summary

To summarize, the approximate 3D-2D (or 2D-1D) model consist of flow part, elastic part, interface conditions and boundary conditions. The flow part is the Navier-Stokes-Brinkman system of equations (2.11). The elastic part is either the elastic shell model (3.11), (3.12) and (3.13) or the poroelastic plate model (3.20). We impose the interface conditions (2.20), (2.23) and (2.24). The boundary conditions which we impose on the fluid flow are the inlet boundary condition (2.4), the outlet boundary condition (2.6) and the no-slip boundary condition (2.3). When using the elastic shell model, we impose the boundary conditions (3.14). When using the poroelastic plate model, we impose the boundary conditions (3.22).

Chapter 4

Numerical algorithm

In Chapter 2 and Chapter 3 we described mathematical models for FPSI in the context of dead end filtration. In this chapter we show how we solve the mathematical models numerically. First we discuss the general strategy of the framework that we create. Then we discuss in detail the discretization techniques. In the last section of this chapter we describe the computational grids in use along with the strategy for grid stretching without remeshing.

4.1 Solving the coupled system

In his work [12] Richter describes the main techniques used to solve FSI problems. The main challenge in this multi-physics problem is the different configurations in which the fluid equations of motion and the displacement equations are defined. While the deformation equations are given naturally in the initial (non-deformed) configuration, the fluid flow is naturally defined in the deformed configuration. In the context of FPI, the equations written in original configuration are also referred to as Lagrangian formulation of a problem. To the equations written in the deformed configuration one might refer to as Eulerian formulation. There are two main strategies to solve FSI problems.

One approach is the fully Eulerian formulation of the problem. In this case the elasticity equations are defined on the deformed domain. This requires mapping of the domain Ω_p to $\tilde{\Omega}_p$. In this case the solution of the elasticity problem is giving such a mapping and the elasticity equations become highly non-linear. For more information on the fully Eulerian approach see [23].

Figure 4.1: Initial shape of a single pleat

The other main approach is to use the Arbitrary-Lagrangian-Eulerian approach (ALE). In this method, a transformation T is used to map the initial reference domain Ω_f onto the deformed domain $\tilde{\Omega}_f$ (see Fig. 2.1). Then the inverse mapping T^{-1} is used to write the interface condition in the initial Lagrangian configuration. In dynamic systems using the initial domain as a reference domain imposes a limitation on the robustness of the method. In such cases the domain at a previous time is used as a reference domain and it is changing with the dynamics of the system. However, we are interested in the steady state solution of the system and using the initial domain as a reference domain does not limit the performance of the method.

While the fully Eulerian approach is more robust for large displacements, the ALE approach has the benefit of introducing non-linearities only in the interface conditions. From mathematical point of view both of the methods describe the FSI problem accurately. The practical difference is in the numerical methods which are used in order to solve the resulting system of equations. For the FPSI problem we use the ALE approach. This allows us to reuse previously developed numerical algorithms which solve efficiently the flow subproblem as well as the elasticity subproblem. In addition, we can use different models for the elasticity without the need to transfer the equations in different configuration. For particular configurations and small deflection of the porous media we can also use an approximation of T^{-1} which does not require additional computational time.

Let us now discuss the general FPSI framework based on the ALE approach. To help illustrate the algorithm we use as an example the deflection of a single porous pleat in a rectangular channel - see Fig. 4.1. In this example the blue colored domain represents the plain fluid region, while the red colored domain represents the initial configuration of a the porous media – a single pleat. For this experiment we set the left side of the rectangular domain to be inlet, the right one to be outlet and the top and bottom sides to be supporting structure with the no-penetration and no–slip boundary condition. Due to fluid flow from the left to the right side of the channel the pleat is deflecting - see Fig. 4.2.

The FPSI numerical framework we use is the following:

1. We start with a given initial geometry – e.g. Fig. 4.1. On this domain we create a boundary- and interface- capturing grid (see e.g. Fig. 4.4).

Figure 4.2: The shape of the single pleat after displacement

2. Having a grid resolving the plain flow domain as well as the porous medium, we numerically solve the Navier-Stokes-Brinkman system of equations (2.11) with the inlet boundary condition (2.4), the outlet boundary condition (2.6) and the no-slip boundary condition (2.3). At this stage we treat the porous media as rigid. On the first iteration we solve the flow problem on the initial (non-deformed) domain. On every other iteration we solve the flow problem on the deformed domain.

3. Now that we have solved the Navier-Stokes-Brinkman system of equations, we have numerically calculated the fluid velocity $\tilde{\mathbf{v}}_f$ (see Fig. 6.1 and Fig. 6.2) and the fluid pressure $\tilde{p}_f$ (see Fig. 5.17 and Fig. 5.18). Using these values we can calculate the fluid stress tensor $\tilde{\sigma}_f$. This tensor is defined in the deformed configuration. In order to calculate the stress tensor $\overline{\sigma}_f$ we need to apply the transformation T^{-1}. In the most general case we have to numerically solve an equation to find the transformation T and then numerically invert this transformation in order to use T^{-1}. One can use the Poisson's equation or a biharmonic equation to extend the deformation of the domain Ω_p on the domain Ω_f and find a mapping T. In our particular case this is not needed. As we focus on porous media with low permeability, in close proximity to the interface $\partial\tilde{\Omega}_{pf}$ the fluid flow is orthogonal to the interface. Also, the magnitude of the fluid velocity is nearly constant along $\partial\tilde{\Omega}_{pf}$. Therefore, we can approximate the stress tensor with the dominating pressure term $\overline{\sigma}_f \approx \overline{p}_f I$. Using this approximation we only need to map the fluid pressure $\tilde{p}_f$ from the interface $\tilde{\Omega}_{pf}$ to the interface Ω_{pf}. As we deform the grid using the elasticity deformation, this mapping we obtain in a trivial way.

4. After we have calculated the normal component of the stress tensor σ_f, we use it as the given force $\mathbf{S}(\mathbf{x})$ to solve the elasticity equations. In the general case one can solve the Biot's system of equations (2.12), (2.15) with the boundary conditions (2.16) and (2.17). In this work we use the plate model or the shell model instead. For summary of the equations and the boundary conditions governing the poroelastic plate and shell models see section 3.4. The effect of the fluid flow on the displacement of the porous media is covered either by interface conditions in the case of the Biot system or through the right-hand-side of poroelastic plate and shell systems.

5. From the plate and shell models we get as a result the displacement of the middle surface $\hat{\Omega}_p$. In order to reconstruct the full porous domain $\tilde{\Omega}_p$, we use the assumption that the thickness of the media does not change with the deflection of the porous material. For each (numerical) point of the deformed domain middle surface we calculate the normal vector. On the distances $-\frac{h}{2}$ and $\frac{h}{2}$ we have the (numerical) position of the interface $\partial\tilde{\Omega}_{pf}$ in the inlet- and outlet-regions, respectively.

6. After calculating the displacement of the porous media $\mathbf{u}_p$ we update the computational domains $\tilde{\Omega}_p$ and $\tilde{\Omega}_f$ (see Fig. 4.2). This captures the effect of the displacement on the fluid flow. In the general case we have to numerically solve an equation in order to update the computational grid for the plain fluid region $\tilde{\Omega}_f$. One can once again use the Poisson's equation or a biharmonic equation to find the mapping T and use this mapping to move the grid vertices. Alternatively one can also create a new grid (remesh), but this approach is even more computationally expensive. We use special grids which allow us to update the grid using interpolation. In section 4.3 we discuss in detail the construction of these special grids.

7. After we have updated the grid (see Fig. 4.7), we go back to step 2. We repeat the steps 2. to 6. until convergence. Convergence is achieved when there is no change in domains $\tilde{\Omega}_p$ and $\tilde{\Omega}_f$ from one iteration to the next one.

As we use an iterative approach to solve the equations describing FPSI, we write independently the discretizations of the flow equations and the elasticity equations. This allows us to use different solvers for the algebraic systems that we obtain from the discretization of the two systems of equations. We even use a special approximation in order to avoid additional computations for the mapping T and its inverse. An alternative approach would be to use a monolithic discretization. Although the monolithic solvers are known to be more stable, they do have their disadvantages. In a monolithic discretization the algebraic system of equation is much larger as it is incorporating in the same time the fluid velocity and pressure, the effective pore pressure, the displacement of the porous media and the coupling mapping T. Such a matrix also has a different structure from the matrices of the independent flow and elasticity problem. There is no guarantee that solvers which work well for the subproblems would also give accurate solutions of the large monolithic system. Although the monolithic system solves the fluid problem and the deformation problem together, it does solve a non-linear problem (as the interface conditions depend on the solution of the system). Therefore, one would have to perform Newton iterations in order to accurately solve the system. Thus, the monolithic discretizations are more stable, but they generally require more computational time and a more complex solver for the linear system of equations.

4.2 Discretization

In this section we discuss in more details how we discretize the different systems of equations.

4.2.1 Discretization of the Brinkman system of equations

In order to accurately capture the local conservation of mass in the Navier-Stokes-Brinkman system of equations, we use the Finite Volume Method (see e.g. [53] and [54]) to discretize the flow problem. Although solving the incompressible Navier–Stokes system of equations is not an easy task, this is a classic problem and FV numerical schemes are well studied and used in wide area of applications (see e.g. [55] and [56]). However, the Darcy term in the Navier-Stokes-Brinkman system of equations creates an additional complexity. The permeability of the filtering media in oil filter elements is often of order 10^{-10} while we set the permeability of the plain fluid domain to infinity. This creates a jump in the flow resistivity K^{-1} of 10 orders of magnitude through the interface $\tilde{\Omega}_{pf}$.

In the framework of FPSI we increase the numerical complexity of the problem even further. Even if we have an initial grid with good properties, after the deformation of the porous media the updated computational grid can have stretched elements. To ensure a robust discretization of the equations with a large jump of the permeability on complex (rough) grids, we use multipoint flux-approximation method (MPFA). This method was originally proposed for a scalar equation by Aavatsmark in [37]. It was modified for the Stokes-Brinkman problem in [38] by Iliev and co-authors. The main problem that MPFA solves is the approximation of the fluid flux $\nabla\tilde{\mathbf{v}}_f$. When using FV on a general quadrilateral grid the pressure and velocity variables are defined in the center of the quadrilateral elements (see Fig. 4.3). The line connecting the centers of two adjacent grid elements in the general case is not perpendicular to the edge which these two elements share. Thus, using only two elements to approximate the flux through a particular edge leads to an inaccurate numerical solution. The MPFA method gives accurate approximation of the flux through an edge by using multiple elements to perform the approximation of such terms. While the pressure and velocity variables are still defined in the centers of the primary grid (in Fig. 4.3 with red), a second so called dual grid is used (in Fig. 4.3 with blue) in order to approximate the flux on the edge of a dual element. As a result the discretization scheme is more accurate and robust.

To obtain the steady state solution of the Navier-Stokes-Brinkman system of equations, we solve the dynamic system of equations (2.9) until the steady state is achieved. However, we use the time variable as a stabilizing parameter instead of considering it as a physical time. This is why we call the discrete time steps fictitious time steps.

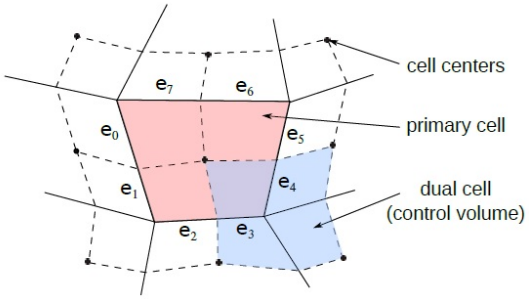

Figure 4.3: Schematic illustration of primary and dual cells in MPFA. Figure from [37]

For the fictitious time discretization we use a Chorin-type projection method. This method is a fractional-time-step method. For each time step we first compute the fluid velocity in an intermediate fictitious time using an implicit scheme for the velocity and using the pressure from the previous time step. As a second step, we compute the pressure correction on the next fictitious time step using the obtained fractional time step velocity. We use this pressure to correct the intermediate solution for the fluid velocity to the numerical solution on the next time step. For this reason the method is also called a pressure correction method. For more information on the MPFA and the Chorin-type method we use, see [37].

The linear systems at each fictitious time step we solve with a robust algebraic multigrid method available in a commercial software. We use the implementation of the SCAI Fraunhofer institute - see [43], [44] and [45] or visit the SCAI SAMG web page [46].

4.2.2 Discretization of the Biot's system of equations

To validate the accuracy and validity of the poroelastic plate and shell models, we numerically solve the Biot's system to use as a reference solution. For this simulations we make use of the commercial software COMSOL Multiphysics version 4.2. This software provides implementation of the Finite Element Method for discretization. We use linear elements for the pressure and quadratic elements for the displacement field. It is important to note that for certain geometries, boundary conditions and computational grids, it is necessary to use higher order elements for the displacement field in order to avoid non-physical locking effects. To avoid such locking effects we use triangular prism elements instead of tetrahedral elements - see Fig. 4.12. The resulting linear algebraic system of equations we solve using the iterative Generalized Minimal Residual method (GMRES) implemented in COMSOL Multiphysics.

4.2.3 Discretization of the linearly elastic shell system of equations

To discretize the system of equations (3.11), (3.12) and (3.13) we use a Finite Difference (FD) discretization. We use a grid $\{x_i, i = 1, 2, ..., n\}$ and the notation $F_i := F(x_i)$ for every function in the discretization. Let us denote $h_i = x_i - x_{i-1}$ for $n = 2, 3, ..., n$. We describe in detail the discretization of the equation (3.11). The equations (3.12) and (3.13) we discretize in the same manner. As ϵ, μ, λ and λ^* are constants we will omit them from the discretization of the separate terms. In the left-hand side of equation (3.11) we have the following terms containing derivatives:

$$\theta_i'' \approx \left(\frac{\theta_{i+1} - \theta_i}{h_{i+1}} - \frac{\theta_i - \theta_{i-1}}{h_i} \right) \frac{1}{\left(\frac{h_{i+1}+h_i}{2} \right)}, i = 2, 3, ..., n-1, \tag{4.1}$$

$$\left(bu'\right)_i' \approx \left(a_i \frac{u_{i+1} - u_i}{h_{i+1}} - a_{i-1} \frac{u_i - u_{i-1}}{h_i} \right) \frac{1}{\left(\frac{h_{i+1}+h_i}{2} \right)}, i = 2, 3, ..., n-1, \tag{4.2}$$

$$\left(b^2 w\right)_i' \approx \frac{b_{i+1}^2 w_{i+1} - b_{i-1}^2 w_{i-1}}{h_i + h_{i+1}}, i = 2, 3, ..., n-1, \tag{4.3}$$

$$w_i' \approx \frac{w_{i+1} - w_{i-1}}{h_i + h_{i+1}}, i = 2, 3, ..., n-1. \tag{4.4}$$

For the terms without derivatives we do not use any averaging. The values a_i are an approximation for $b_{i+0.5} = b(x_i + 0.5h_{i+1})$. We use the harmonic mean for an approximation.

$$a_i = \frac{2 b_i b_{i+1}}{b_i + b_{i+1}}, i = 2, 3, ..., n-1. \tag{4.5}$$

We approximate the right-hand side terms containing derivatives in the following matter:

$$\left(p_e^2\right)_i' \approx \frac{p_{e(i+1)}^2 - p_{e(i-1)}^2}{h_i + h_{i+1}}, i = 2, 3, ..., n-1, \tag{4.6}$$

$$\left(bp_o^2\right)_i' \approx \frac{b_{i+1} p_{o(i+1)}^2 - b_{i-1} p_{o(i-1)}^2}{h_i + h_{i+1}}, i = 2, 3, ..., n-1. \tag{4.7}$$

In order to ensure the Dirichlet boundary conditions (3.14) we impose:

$$\theta_1 = \theta_n = 0, \quad u_1 = u_n = 0, \quad w_1 = w_n = 0. \tag{4.8}$$

To solve the resulting linear system of equations we use the direct solver of the commercial software MATLAB version R2013.

For one example in this work we provide an additional numerical solution of the poroelastic shell model using COMSOL Multiphysics version 4.2. In this case we use a FEM discretization with second order element. As in the FEM method we use the weak formulation of the poroelastic shell model (3.3), we impose the boundary conditions also weakly by penalization terms. This allows us to impose more boundary conditions and to test a particular hypothesis. In order to solve the resulting linear system of equations we use the Multifrontal Massively Parallel Sparse direct Solver (MUMPS) implemented in COMSOL.

4.2.4 Discretization of the poroelastic plate equation

For the discretization of the biharmonic equation 3.20 we once again make use of the commercial software COMSOL Multiphysics version 4.2. We use the Finite Element Method to discretize the equation (3.27). As we discuss in section 3.3, we impose the boundary conditions weakly. We use the quintic Argyris triangular elements in order to avoid locking effects near the boundary. These elements have six degrees of freedom in each vertex and one degree of freedom per edge of a triangular element. The choice of the degrees of freedom allows for C^1 continuity of the solution with C^2 continuity at the vertices of the triangular elements. These elements were described by Argyris in [47] and initially called TUBA elements. In this work they were used to solve plate bending problems. When interested in the steady state solution, the elastic and poroelastic Kirchoff type plate models differ only in the right-hand side of the biharmonic equation. When the plates are uniformly loaded, the right hand sides of the biharmonic equations for elastic and poroelastic media only differ by a factor. For this reason we are using the quintic Argyris triangular elements to solve the poroelastic plate equation.

4.3 Computational grids

In this section we discuss the computational grids that we use in order to discretize the different systems of equations. For visualization we use the commercially available software COMSOL Multiphisics version 4.2 and the open-source software ParaView version 4.1.0 64-bit.

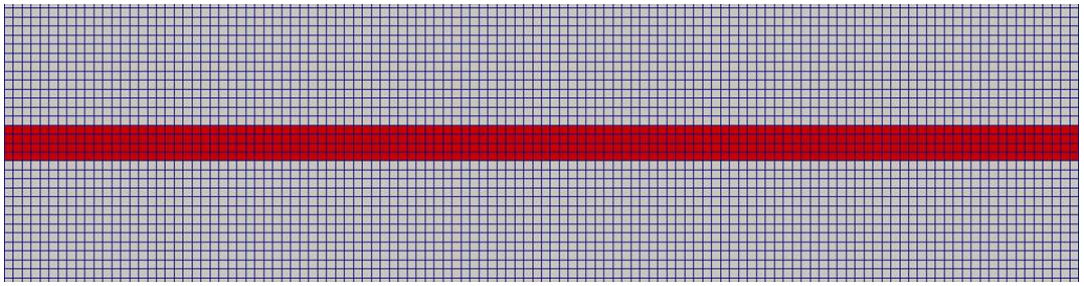

Figure 4.4: Initial grid for a rectangular channel

4.3.1 Computational grids for the Brinkman system of equations. Flat media

In this work we consider two different types of geometries on which we solve the Navier-Stokes-Brinkmamn system of equations. The first geometry is a section of a rectangular channel (see 5.19). For this simple geometry we use a Cartesian grid to mesh the initial domain Ω. A segment of such a Cartesian grid near the porous media is shown in Fig.4.4. With blue color we represent the free flow region and with red color the poroelastic media.

As discussed in 4.1, we deform this grid with the deformation of the porous media. Let us first discuss the inlet region. For the grid vertices on the inlet we consider no change in their coordinates. After we obtain the numerical solution of the elasticity problem, we know the deformation of the grid nodes inside the porous media. In the case of initially flat filtering media we use the poroelastic plate model. It provides the displacement of the middle line. In this model we assume the Kirchoff's hypothesis. This means that the line perpendicular to the middle surface stays perpendicular after displacement. Thus having the position of the middle surface and calculating the normal vector, we can obtain the position of all of the grid nodes after displacement. Let us focus on a vertical line of grid nodes in the upper plain flow region. We set the most top node not to have any displacement and the most bottom one to have a given deformation (obtained from the elasticity solution). The grid displacements of the grid nodes in between we obtain by linear interpolation between the two fixed values. Note that this is only a simple calculation and it does not require solving of an additional system. Such a method can be referred to as grid stretching. The displacements of the outlet region we handle the same way. In Fig. 4.5 we show how the grid from Fig. 4.4 is being stretched with the deformation of the porous media.

4.3.2 Computational grids for the Brinkman system of equations. Poroelastic pleat

The second geometry which we consider is a single poroelastic pleat in a rectangular channel - see Fig. 4.1. For this more complex geometry we create a special boundary-

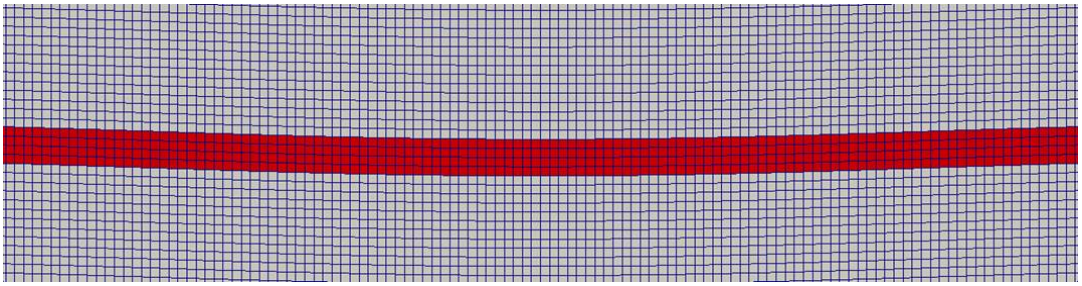

Figure 4.5: Deformed grid for a rectangular channel

Figure 4.6: Initial grid for a channel with a pleated filtering media

and interface- fitted grid - see Fig. 4.6. Firstly we discuss how we handle the change of the domain with the deformation of the porous media and then we will discuss how we construct the numerical grid itself.

The geometry of a single pleat (see Fig. 4.6 and Fig. 4.1) is more complex than a flat filtering media. However, in Chapter 5 we demonstrate that under uniform load, the deformation of the pleat is primarily in the straight part of the pleat. Next to the straight parts of the pleat we use a Cartesian grid. Thus, we can once again apply the our strategy for grid stretching that we use for initially flat filtering media. We move only points inside the Cartesian region having in mind the symmetry of the domain and the loads. In this configuration we fix the top and the middle vertical lines of vertices. After calculating the displacement of the nodes in the top straight part of the filtering media, we interpolate them between the top and the middle line to update the position of the vertices in the grid. In a similar manner we fix the middle and the bottom line of vertices. Then, knowing the displacement of the vertices in the bottom half of the porous media, we interpolate them between the middle and bottom vertical lines in order to obtain the new position of the bottom half of the grid vertices. An example of a grid after displacement of the porous media takes place is presented in Fig. 4.7.

In Fig. 4.8 we show only a section of the grid presented in Fig 4.7 in order to give a more detailed representation of the computational grid. The porous media that we consider is in a shape of a pleat with constant thickness along its length. When the filtering media is with small permeability, the flow through it is primarily perpendicular to the surface of the pleat. In order to accurately capture such flows we use a

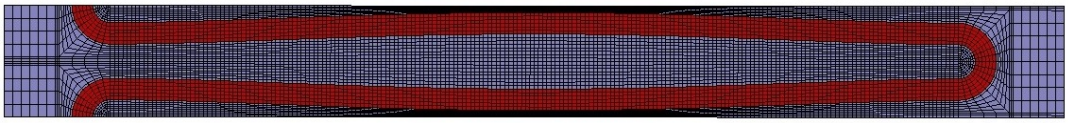

Figure 4.7: Deformed grid for a channel with a pleated filtering media

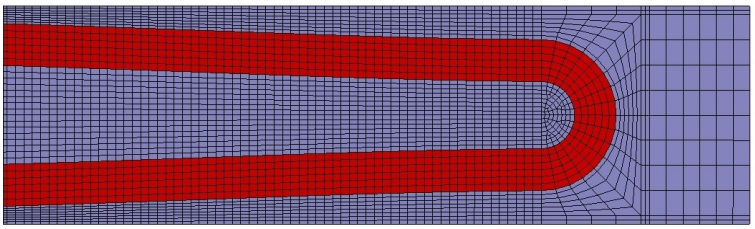

Figure 4.8: Detailed view of a deformed grid for a channel with pleated filtering media

locally orthogonal grid for the filtering media. In the straight parts we use a Cartesian grid. In the tip of the pleat (sector of a circular domain) we use a regular cylindrical grid (see Fig. 4.8). In the regions of free flow next to the straight parts of the filtering media, we also use a Cartesian grid.

The subregions that are not trivial to mesh are around the tip of the pleat. Let us first discuss the sub-domain outside of the circular part of the filtering media. For each eighth of a circle we have a quadrilateral sub-domain with three straight sides and one curved concave side. In these curved-boundary quadrilateral sub-domains we use locally Cartesian grids.

Let us now discuss the sub-domain inside the circular part of the filtering media (see Fig.4.9). For each fourth of a circle we have a topologically triangular domain with two straight sides and one curved side. In order to create the grid in this region we consider multiple grid layers. In the most outer layers we create a locally orthogonal grid next to the curved interface. As we create the layers closer to the center of the circular sub-domain, we reduce the number of the quadrilateral elements. In Fig. 4.9 we have 8 elements in the most outer layers for a quarter circle. Using a layer with diamond-type elements we reduce the elements in a layer from eight to four. Near the center of the circle we use a diamond-type grid element to reduce the four grid elements in a layer to one. In a more general scenario we start with an even number of elements in the most outer layer. We reduce them to one using multiple layers containing diamond-type grid elements. In Fig. 4.6, Fig. 4.7 and Fig. 4.8 we also introduce additional layers to control the number of elements that a vertex has (dual connectivity of a vertex). In the latter grids the dual connectivity of each vertex is between three and five. This restriction on the number of dual elements is not always required and for some examples we do not create these additional layers.

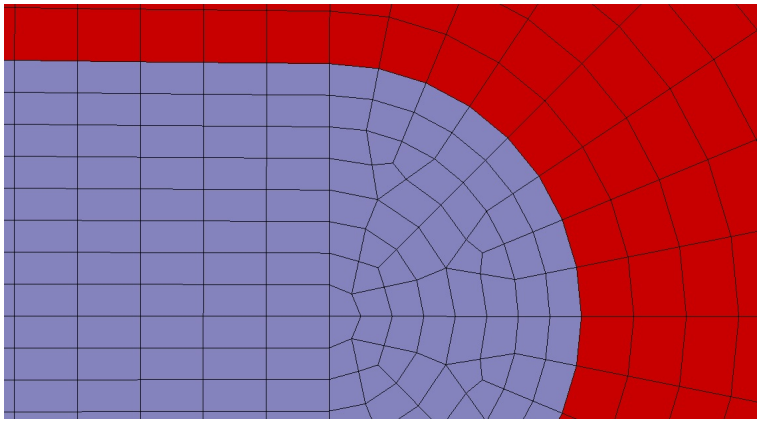

Figure 4.9: Deformed grid in the inner region of a tip in a single pleat

We also extend the grid generation to more complex geometries of multiple pleats. In Fig. 4.10 we demonstrate a domain which has 60 pleats and is resembling a cross section of a filter of the same type as the industrial oil filter presented in the left side of Fig. 1.1. In this geometry we consider the domain around a single pleat to be a sector of a circle rather than a rectangular box. In this case some of the rectangular sub-domains are now quadrilateral subregions with one or two curved boundaries. In Fig. 4.11 we present a segment of the grid that we have created to perform numerical simulations on the domain presented in Fig. 4.10. One result of these numerical experiments we present in section 6.2.

4.3.3 Computational grids for the Biot's system

We use the solutions of the Biot's system as a reference solution for the poroelastic plate and shell models. As computational grids for the Biot's system when comparing with the poroelastic plate model, we use triangular prism grid elements - see Fig. 4.12. The choice of this grid elements (and FEM elements) is partially in order to avoid numerical locking effects. On the other side with this geometry we have a triangulation of the top circle of the domain. We use this triangulation as a grid in the numerical solutions of the poroelastic plate model. The use of such similar grids helps us with the control of the approximation errors. The grid shown in Fig. 4.12 is with a low number of elements - 1800. This grid we use only for ease of visualization. For accurate numerical experiments we use grids with as much as 70 000 prism elements.

When we use the Biot's system as a reference solution for the elastic shell models, we perform 2D simulations for plain strain simulations (we set all of the derivatives in one direction to 0). We perform such experiments on a geometry of circular segment (see Fig. 4.13) and 2D pleat cross-section (see Fig. 4.14). For the latter examples we use triangular grids ensuring at least 3-4 elements through the thickness of the media.

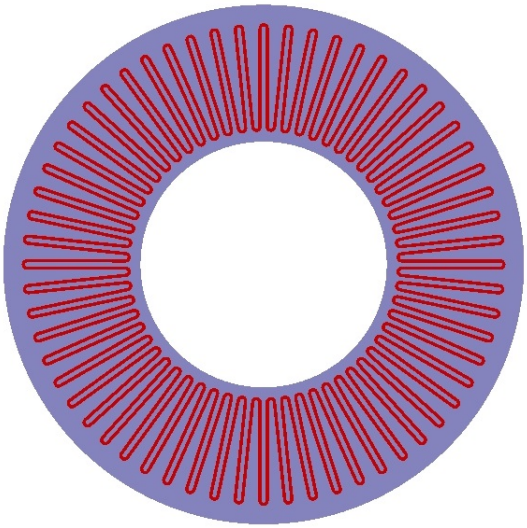

Figure 4.10: Cross-section of a round filter housing with 60 pleats

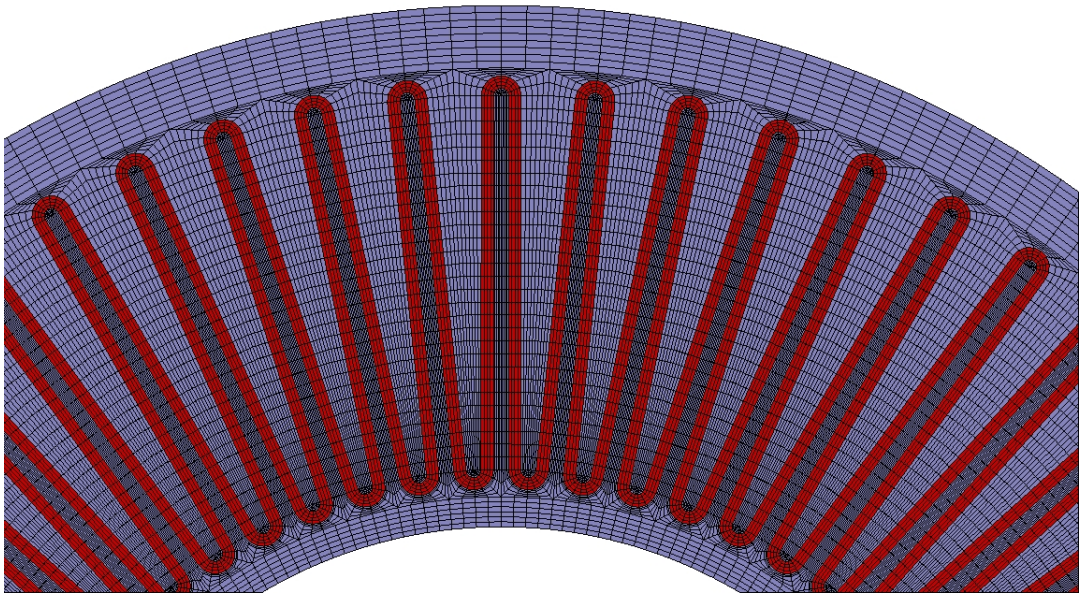

Figure 4.11: Segment of a grid for a filtering media with 60 pleats

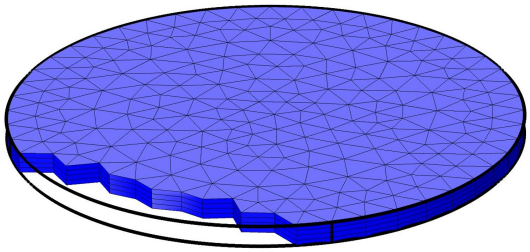

Figure 4.12: Grid consisting of triangular prism elements

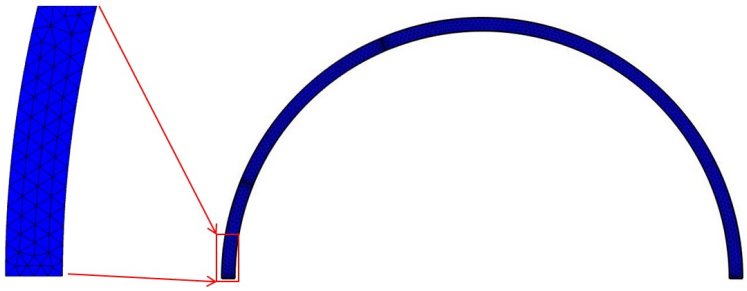

Figure 4.13: Triangular grid for a circular arch

If one would have only two layers of triangular elements, there might be a vertex in which two boundary conditions are imposed weakly. If such a vertex exists, one can observe decrease of the accuracy of the solution or numerical instability.

4.3.4 Computational grids for the linearly elastic shell model

We use two different grids to discretize the middle line of a thin poroelastic body. For greater numerical accuracy we use regular grids with a large number of points. We make use of those grids to test the accuracy and the validity of the poroelastic shell model.

For more practically relevant simulations we use a different discretization approach. We take the initial grid from the filtering media for the flow problem. It is locally orthogonal and it is resolving the middle surface of the porous media. Instead of using these grid nodes, we use the center points of each line as a grid point for the elasticity grid. This allows us to transfer the pressure and the normal component of the stress tensor from the flow simulation to the elasticity problem with no need of interpolation.

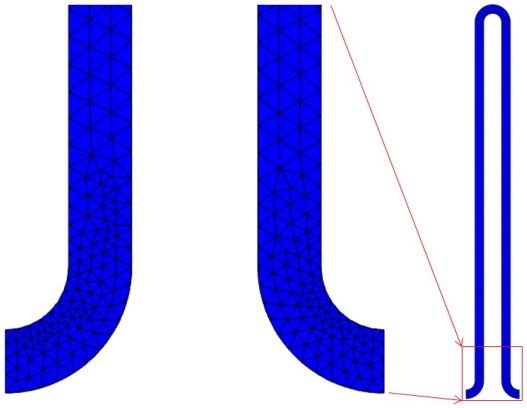

Figure 4.14: Triangular grid for a 2D pleat

4.3.5 Computational grids for the poroelastic plate model

As we discussed in subsection 4.3.3, we use as a grid for the poroelastic plate model a triangulation inherited from the grid used in the Biot's system. As we consider a cylindrical domain, we can use the triangulation of the top of the cylinder as a grid for the middle surface.

Chapter 5

Numerical validation

In this chapter we test the accuracy and the validity of the different mathematical modes we use. We also measure the accuracy of the numerical algorithms. Whenever possible, we make use of available analytical solutions. However, most of the problems are very complex and no analytical solutions are available. In these cases we use numerical solutions of the governing equations or numerical solutions on very fine grids as reference solutions. At the end of this chapter we preform the ultimate validation, testing numerical solutions against a physical experiment.

For visualization of the results in this chapter we use the commercially available softwares COMSOL Multiphisics version 4.2 and MatLab version R2013 as well as the open-source software ParaView version 4.1.0 64-bit.

5.1 Validation and range of validity of the mathematical models

In this section we perform numerical experiments to validate the accuracy and validity of the mathematical models we use. As we use the approximate poroelastic plate and shell models it is very important to show when they give accurate solutions and when not. While plates and shell models in linear elasticity have been analytically and numerically studied, in poroelasticity such studies have not been done yet.

5.1.1 Validation of the shell model

In this subsection we validate the linearly elastic shell model against the governing 3D Biot's system. We consider a material with the mechanical properties of Young's modulus $E = 500KPa$ and Poisson's ratio $\nu = 0.33$. As presented in section 4.2.3,

we use a FD discretization for the linearly elastic model. We have developed a C++ code to build the matrix and the right-hand of the linear system of equations and we use the MatLab direct solver. As presented in subsection 4.2.2, we use a FEM discretization for the Biot's system. We build the linear system of equations and we solve it in COMSOL (using the build in MUMPS direct solver). In this section we consider a 2D plain-strain system. We exclude the derivatives in one spatial direction from the Biot's equation assuming that the media is infinite in this direction. Also no strain or stress is generated from bending with respect to this chosen direction. The resulting Biot's system is two-dimensional. The resulting elastic shell model is a cylindrical shell (also known as a cylindrical beam). In this section we focus on the model effects and not on the discretization errors. For this reason we consider only very fine Cartesian grids for the linearly elastic shell.

Uniformly loaded pleat

Let us first consider a relevant geometry for filtration processes. We present numerical simulations for the geometry of a single pleat - see Fig. 5.1 left. We consider a pleat with thickness $h = 1\ cm$, straight part of 40 cm and inner radius of the tip $r = 1\ cm$. We fix the pleat in the left and right straight parts. In the Biot's system we consider a uniform load along the inner side of the pleat. In Fig. 5.1 left we present with a blue line the boundary Γ_1 on which we apply load. Let the rest of the boundary (the outer side of the pleat) be Γ_2. As boundary conditions in the Biot's system we use

$$\mathbf{S}(\mathbf{x}) = \begin{cases} 10\ Pa\ \mathbf{n}, & \mathbf{x} \in \Gamma_1 \\ 0\ Pa\ \mathbf{n}, & \mathbf{x} \in \Gamma_2 \end{cases}, \quad P(\mathbf{x}) = \begin{cases} 10\ Pa, & \mathbf{x} \in \Gamma_1 \\ 0\ Pa, & \mathbf{x} \in \Gamma_2 \end{cases}. \tag{5.1}$$

On the outer boundary of the pleat we have $\mathbf{S}(\mathbf{x}) = 500\ Pa\ \mathbf{n}$ and $P(\mathbf{x}) = 500\ Pa$. This represents no load and no resistance. Thus we have uniform load along the pleat.

In the shell model the latter conditions are accounted for in the right-hand side of the system of equations. For the Biot's system we use a triangulation with 1746 elements. For the linearly elastic shell model we use a Cartesian grid with 3000 grid points. The numerical results from the Biot's system are presented in Fig. 5.1 middle. The colors represent the magnitude of displacement. Dark blue color stands for smallest displacements and dark red stands for the largest displacements. Once again we consider loads leading to displacements of the order of the thickness of the media. For such cases the use of the Biot's system based on linear elasticity is justified. For larger displacements one might need to make use of non-linear elasticity models. The x-axis, y-axis and the magnitude of displacement are displayed in cm. We can see how the displacement of the media are largely in the straight part of the pleat. We use this effect to update the computational flow grid in the case of FPSI without the need of remeshing.

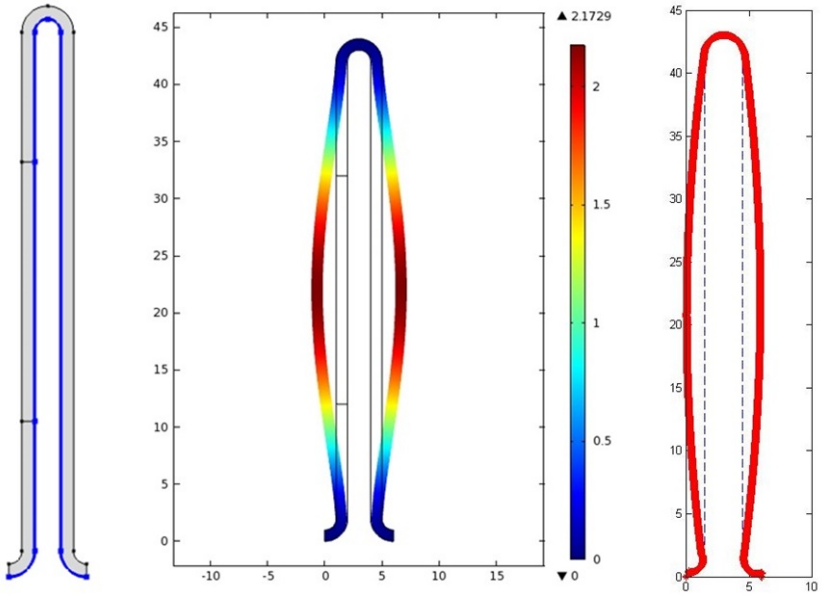

Figure 5.1: left - pleat geometry, middle - displacement obtained using the linear elasticity model, right - displacement obtained using the linearly elastic shell model

The numerical results from the shell model are presented in Fig. 5.1 right. The blue dashed line represents the initial position of the pleat's middle line and the thick red line represents the position of the pleat's middle line after deformation. In this case the numerical result for the linearly elastic shell model shows the same deformations as the Biot' system.

This example shows good agreement between the numerical results obtained with the shell model and the Biot's system.

Uniformly loaded circular arch

Let us also consider the deformation of a circular arch (see Fig. 5.5). We consider this geometry as the curvature of the middle line of the porous media is a constant. In this case the shell model simplifies and we can focus on the physical behavior of the system. We do not have to consider errors coming from the discretization of terms with varying coefficients. Let the arch have inner radius $r = 1.9\ cm$ and thickness $h = 0.1\ cm$. Let the arch be fixed at the bottom straight sides. We consider a uniform load on the inner boundary of the circular arch. We present this inner boundary Fig. 5.5 with a blue line and denote this sector with Γ_1. Let us denote the rest of the curved boundary (the outer boundary of the circular arch) with Γ_2. In the Biot's system we consider the following loads:

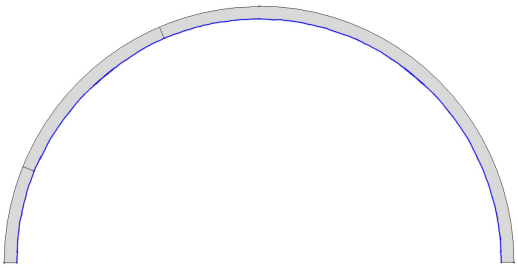

Figure 5.2: Circular arch. The blue line represents the boundary under load

$$\mathbf{S}(\mathbf{x}) = \begin{cases} 500\ Pa\ \mathbf{n}, & \mathbf{x} \in \Gamma_1 \\ 0\ Pa\ \mathbf{n}, & \mathbf{x} \in \Gamma_2 \end{cases}, \quad P(\mathbf{x}) = \begin{cases} 500\ Pa, & \mathbf{x} \in \Gamma_1 \\ 0\ Pa, & \mathbf{x} \in \Gamma_2 \end{cases}. \tag{5.2}$$

On the outer boundary of the circular arch we have $\mathbf{S}(\mathbf{x}) = 500\ Pa\ \mathbf{n}$ and $P(\mathbf{x}) = 500\ Pa$. This represents no load and no resistance. Thus we have uniform load along the circular arch.

In shell model the above conditions come in the right-hand side of the system of equations (see section 3.2). As computational grid for the Biot's system we use triangulation with 1481 elements. For the shell model we use a Cartesian gird with 1000 points.

The results obtained from the shell model we present in the left side of Fig. 5.3. The axes are displayed in *cm*. The blue dashed line stands for the initial position of the middle line of the arch domain. With the thick red line we show the obtained middle surface after displacement.

The numerical results from the Biots's system are presented in the right side of Fig. 5.3. The colors represent the magnitude of displacement. Dark blue color stands for small displacements and dark red color stands for the largest displacements. We should note that with the given material properties and boundary loads, we observe displacements of the order of the material thickness h. These are considered to be small displacements and the linear elasticity model, which the Biot's system is based on, is valid. With linear elasticity one can simulate accurately some type of large (nonlinear) displacements. In the general case, however, nonlinear models are required to accurately capture nonlinear effects in large displacements. The axis and the magnitude of displacement are displayed in *cm*.

Like in the previous example, we obtain the same results from the numerical solutions of the shell model and the Biot's system.

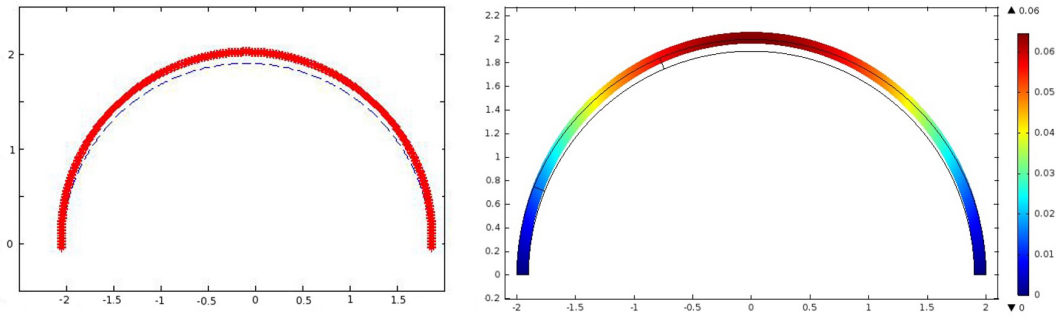

Figure 5.3: Initial and deformed state of a circular arch. Left - results obtained from the shell model, right - results obtained from the Biot's system

Non-uniformly loaded pleat

Let us now consider the geometry of a single pleat under a different loading. Instead of uniform load, we load only the middle third of the pleat's left side - see Fig. 5.4 left. We present the boundary under load Γ_1 with a blue line. Let the rest of the boundary be Γ_2. In the Biot's system we consider the following boundary conditions:

$$\mathbf{S}(\mathbf{x}) = \begin{cases} 2\ Pa\ \mathbf{n}, & \mathbf{x} \in \Gamma_1 \\ 0\ Pa\ \mathbf{n}, & \mathbf{x} \in \Gamma_2 \end{cases}, \quad P(\mathbf{x}) = \begin{cases} 2\ Pa, & \mathbf{x} \in \Gamma_1 \\ 0\ Pa, & \mathbf{x} \in \Gamma_2 \end{cases}. \tag{5.3}$$

In the linearly elastic shell model the latter conditions are accounted for in the right-hand side (see. section 3.2).

We present the numerical results from the Biot's system in the middle of Fig. 5.4. The colors represent the magnitude of displacement. Dark blue color stands for the minimal displacements and dark red stands for the maximal deformation. The axis and the magnitude of displacement are displayed in *cm*. With the particular material properties and loads, we observe displacements of the order of the poroelastic pleat's thickness h.

The numerical results from the linearly elastic shell models are presented in Fig. 5.4 right. The blue dashed line represents the initial position of the pleat's middle line and the thick red line represents the position of the pleat's middle line after deformation.

In this example the numerical results for the Biot's system and the shell model give different results. The Biot's system captures the deflection of the pleat's tip, while the shell model shows no deformation of this region. The Biot's system captures the deflection of both the left and the right side of the pleat, while the shell model gives no deformation of the right side of the pleat.

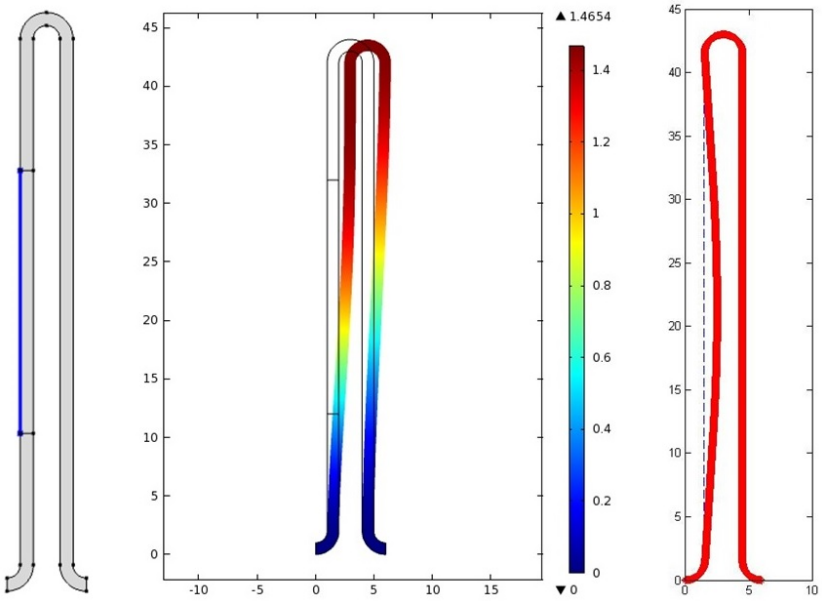

Figure 5.4: left - pleat geometry, middle - displacement obtained using the linear elasticity model, right - displacement obtained using the linearly elastic shell model

Non-uniformly loaded circular arch

To better understand the effect of a non-uniform load, let us consider the deformation the more simple domain of a circular arch. We consider the same arch geometry as presented in the earlier example in this section. In this example, however, we consider a non-uniform load on the outer boundary of the circular arch. We consider non-zero load in a 45° sector as shown in Fig. 5.5 with a blue line. Let us denote this sector with Γ_1 and the rest of the curved boundary with Γ_2. In the Biot's system we consider the following loads:

$$\mathbf{S}(\mathbf{x}) = \begin{cases} 50\ Pa\ \mathbf{n}, & \mathbf{x} \in \Gamma_1 \\ 0\ Pa\ \mathbf{n}, & \mathbf{x} \in \Gamma_2 \end{cases}, \quad P(\mathbf{x}) = \begin{cases} 50\ Pa, & \mathbf{x} \in \Gamma_1 \\ 0\ Pa, & \mathbf{x} \in \Gamma_2 \end{cases}. \tag{5.4}$$

In shell model the above conditions come in the right-hand side of the system of equations (see section 3.2). As computational grid for the Biot's system we use triangulation with 1481 elements. For the shell model we use a Cartesian gird with 1000 points.

The numerical results from the Biots's system are presented in Fig. 5.6. The colors represent the magnitude of displacement. Dark blue color stands for small displacements and dark red color stands for the largest displacements. We should note that with the given material properties and boundary loads, we observe displacements of

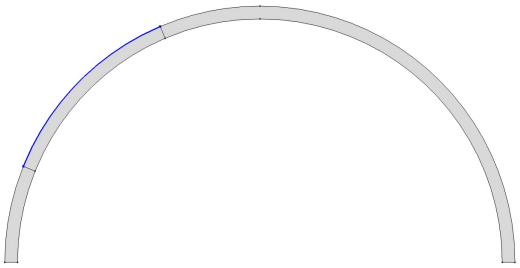

Figure 5.5: Circular arch. The blue line represents the boundary under load

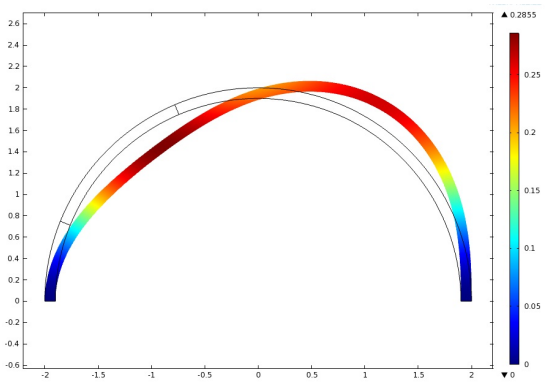

Figure 5.6: Displacement of a circular arch using the Biot's system

the order of the material thickness h. These are considered to be small displacements and the linear elasticity model, which the Biot's system is based on, is valid. With linear elasticity one can simulate accurately some type of large (nonlinear) displacements. In the general case, however, nonlinear models are required to accurately capture nonlinear effects in large displacements. The axis and the magnitude of displacement are displayed in cm. The Biot's system preserves the length of the poroelastic material.

The results obtained from the shell model we present in the left side of Fig. 5.7. The axes are displayed in cm. The blue dashed line stands for the initial position of the middle line of the arch domain. With the thick red line we show the obtained middle surface after displacement. As one can see this result is very different from the Biot's numerical solution presented in Fig. 5.6. The displacements that we observe are only towards the center of the arch. The length of the middle surface is decreased after deformation. There are two possible explanations for this phenomenon.

The first possibility is an inaccurate choice of boundary conditions. We set the displacement and the rotation of the boundary points to zero. For linearly elastic (nonporous) bodies which are strongly clamped, two boundary conditions are being set in the approximate plate models. Besides the zero displacement of the boundary point, the displacements in normal (to the boundary) direction are set to zero. Instead of

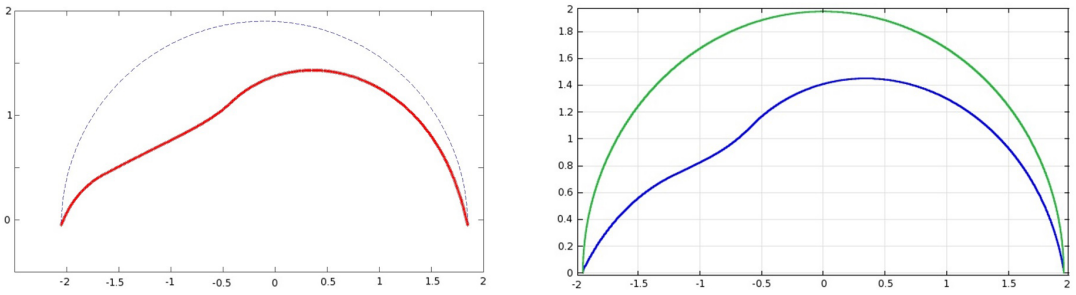

Figure 5.7: Displacement of a circular arch using the linearly elastic shell model. Left - FD, right - FEM

the last condition we set the rotation of the boundary point to zero. We perform two tests in order to clarify if our choice of boundary conditions affects the shape of the numerical results.

The first experiment we perform is to change the shell models in a small neighborhood of the boundary points in the numerical scheme. We add penalization terms $\tilde{C}_1\theta$, $\tilde{C}_2 u$, and $\tilde{C}_3 w$ to the three equations of the elastic shell model in its strong form. By choosing large enough constants $\tilde{C}_1$, $\tilde{C}_2$ and $\tilde{C}_3$, we set the boundary conditions of zero displacement through the equations. We add the condition of zero displacement in normal to the boundary direction by a boundary condition. The numerical results show the first few points next to the boundary point not to have any displacement. However, we do not see any change in the shape of the media after the displacement.

The second experiment we perform is to use COMSOL to obtain a numerical solution of the linearly elastic shell model using FEM. We use the weak formulation 3.3 of the shell model and we impose all of the necessary boundary conditions weakly. We present the results of the COMSOL simulation in the right side of Fig. 5.7. With the green line we show the initial position of the middle line. With the blue line we present the position of the middle line after deformation. The solutions obtained with the FD and FEM discretization match perfectly. For the solution presented in the right side of Fig. 5.7 we use quadratic Lagrangian FEM elements on a mesh with 100 grid points. In order to solve the linear system of equations we use the MUMPS direct solver build in COMSOL. We have also performed numerical experiments using elements of order one, three, four and five. We do not observe any change in the solution. We should note that one should carefully choose the penalizing constants in order to obtain a stable solution. This is especially important when using higher order elements. For this geometry and boundary loads we use the penalizing constants $\tilde{C}_1 = \tilde{C}_2 = \tilde{C}_3 = 10^7$.

The numerical experiments show that the difference in the shape of the solutions of the Biot's system and the shell model are not due to inaccurate representation of the

boundary conditions. The only possibility left is that for this geometry, boundary conditions and boundary loads, the solution of the linearly elastic shell model does not converge to the solution of the governing elastic system in the Biot's equations. The convergence of the shell model to the governing model depends highly on the particular choice of geometry, boundary conditions and forces applied (see [34]).

The examples presented in this section show a limitation of the shell model.

5.1.2 Validation of the plate model

In this section we test the validity of the poroelastic plate model against the Biot's system.

Different media thickness

In this subsection we validate the numerical solutions of the poroelastic plate model (3.20) against the governing Biot's system (2.12), (2.13). In subsection 5.2.2 we demonstrate the accuracy of the poroelastic plate solver. However, the poroelastic plate and shell models are an approximaiton of the Biot's system. Even when the discretization errors of the solution are small, we could have a large error from the model. For large values of the thickness of the media h the approximation models are not accurate. It is important to understand when exactly the thickness of the media is large enough to accumulate a visible error. For linear elasticity and linearly elastic shell models studies have been made. The studies show that for media with thickness less than 4% of the characteristic body length (in our case R), the shell model gives accurate solutions. For elastic media with thickness more than 4% of the characteristic length the differences between the shell model and the linear elasticity is large. This is due to a term containing $\sqrt{h}$ which is omitted in the asymptotic derivation of the linearly elastic shell models. The Biot's system is a more complex one and although it is based on linear elasticity it is important to see if this estimation holds for poroelastic bodies. This is why we perform numerical experiments comparing numerical solutions of the shell model we use against Biot's system for bodies with increasing thickness. We are also interested in the accuracy of the poroelastic plate for thin media and loads leading to displacements which we expect to observe in industrial filtering media.

For the Biot's system we consider a cylindrical poroelastic body (see Fig. 5.8 right). The poroelastic plate system is defined on the middle surface of the domain of interest which is a circle in this case (see Fig. 5.8 left). We uniformly load the elastic body. This results in a cylindrical symmetry for the system. On Fig. 5.9 we present one set of numerical solutions of the shell model and the Biot's system for a particular set of physical parameters and loads. One can see that the numerical solutions also have cylindrical symmetry. For this reason we present a comparison of the displacements obtained from the two models on a shared diameter - see Fig. 5.8.

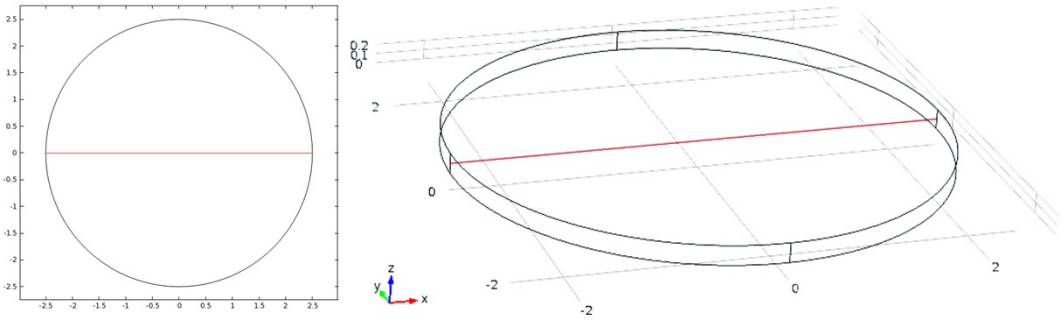

Figure 5.8: left - diameter in the circular 2D domain, right - diameter in the central surface of the 3D domain

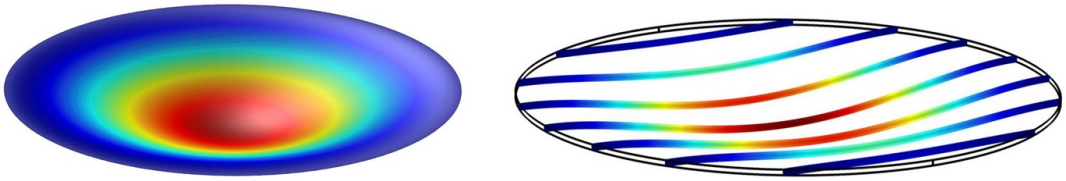

Figure 5.9: left - deformation of a thin cylinder obtained using the poroelastic plate model, right - deformation of a thin cylinder obtained using the Biot's system

In all of the examples in this subsection we consider as a geometry a cylinder with a radius $R = 2.5\ cm$. As mechanical parameters we use Young's modulus $E = 10^6\ Pa$ and Poisson's ratio $\nu = 0.33$. As relative errors we consider the following norms:

$$\hat{L}_\infty = \frac{\|\omega_{\text{plate}} - \omega_{\text{Biot}}\|_{L_\infty}}{\|\omega_{\text{Biot}}\|_{L_\infty}}, \quad \hat{L}_2 = \frac{\|\omega_{\text{plate}} - \omega_{\text{Biot}}\|_{L_2}}{\|\omega_{\text{Biot}}\|_{L_2}}. \tag{5.5}$$

Let us consider different thicknesses of the reference 3D body of a thin circular cylinder. In table 5.1 we present the relative errors for a medias with thicknesses $h = 2\%R$, $h = 4\%R$ and $h = 8\%R$. For these examples we use the following load:

$$\mathbf{S}(\mathbf{x}) = \begin{cases} 0.103079\ Pa\ \mathbf{n}, & \mathbf{x} \in \Gamma_+ \\ 0\ Pa\ \mathbf{n}, & \mathbf{x} \in \Gamma_- \end{cases}, \quad P(\mathbf{x}) = \begin{cases} 0.103079\ Pa, & \mathbf{x} \in \Gamma_+ \\ 0\ Pa, & \mathbf{x} \in \Gamma_- \end{cases}. \tag{5.6}$$

Using the relation (5.9) we chose the pressure drop in such a way that the amplitude of the displacement is around $0.1h$.

From table 5.1 one can see how the model error from the approximate plate model increases with the increase of the thickness h. In Fig. 5.10 we compare the solutions

h	$2\%R$	$4\%R$	$8\%R$
$\hat{L}_\infty$	3.0039×10^{-4}	3.9880×10^{-3}	2.4414×10^{-2}
$\hat{L}_2$	2.4468×10^{-3}	7.2843×10^{-3}	3.1715×10^{-2}

Table 5.1: Relative differences between the plate model and the 3D solution for different thicknesses h

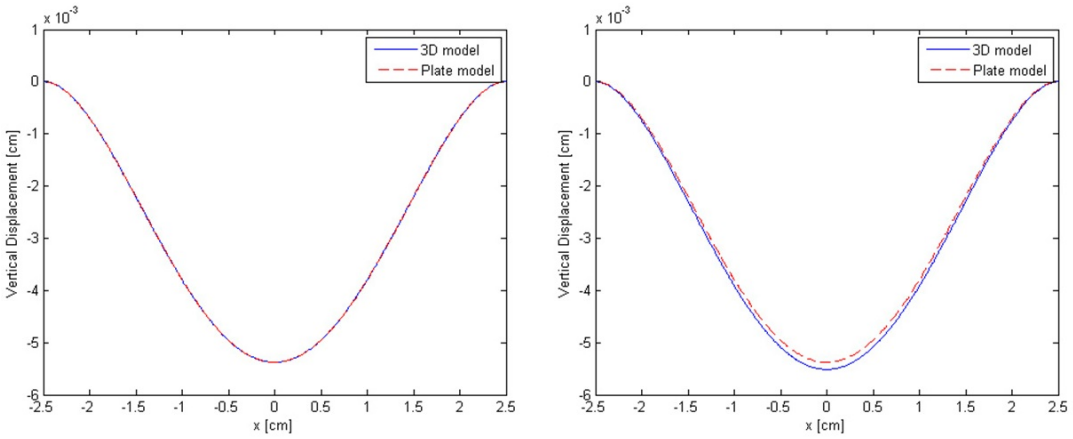

Figure 5.10: Comparison of the displacement of the middle line for Biot's system and the poroelastic plate model. The thickness of the media is: left - $2\%R$, right - $8\%R$

of the two different models for the thinnest porous media with $h = 2\%R$ on the left and $h = 8\%R$ on the right. With the blue line we present the solution of the 3D Biot's system and with the dashed red line we show the solution of th poroelastic plate model. There is no visible difference between the solutions for the media with thickness of $2\%R$. For media with thickness of $4\%R$ we also do not observe visible difference between the two models. For the thicker media with $h = 8\%R$ there is clear difference between the two solutions. However, the solution of the poroelastic plate model resembles accurately the shape of the Biot's solution. In particular industrial applications, an average (or maximal) error of $1 - 2\%$ (or even more) is within the accepted tolerance as long as the shape of the solution is similar. In such cases the poroelastic plate equations can be used instead of the Biot's system to obtain in timely efficient manner accurate solution.

Different amplitude of displacement

Let us now consider media with constant thickness $h = 2\%T$. We apply different loads giving different amplitudes of displacement. From the relation (5.9) we can see that doubling the pressure drop will result in displacement with two times larger amplitude.

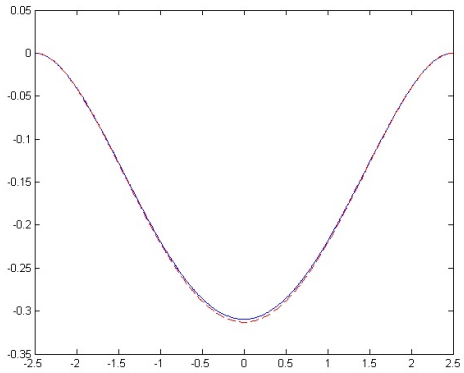

Figure 5.11: Comparison of the displacement of the middle line for Biot's system and the poroelastic plate model. The amplitude of deformation is $8h$

Clearly this is valid only for the poroelastic plate model and the solution of the Biot's system may differ. In table 5.2 we present the relative error of the poroelastic plate model for numerical experiments with different amplitudes.

$\lvert\omega(0)\rvert$	$2\%h$	$10\%h$	$50\%h$	$100\%h$
$\hat{L}_\infty$	1.0009×10^{-5}	3.0039×10^{-4}	1.1023×10^{-3}	1.8050×10^{-3}
$\hat{L}_2$	3.7971×10^{-4}	3.7953×10^{-4}	3.8689×10^{-4}	4.1400×10^{-4}

Table 5.2: Relative difference between the plate model and the 3D solution for amplitudes of displacement $\lvert\omega(0)\rvert$

For the smallest displacement we apply the loads presented in equation (5.6). For all of the other displacements we increase the load on the boundary Γ_+ accordingly (see (5.9)). For deformations with an amplitude as large as h the poroelastic plate model is giving very accurate results. For these cases there is no visible difference between the poroelastic plate model and the Biot's system. We do not consider larger displacements in our studies of dead end filters. In other applications one might experiance larger deformations. In Fig. 5.11 we present the numerical solutions of the Biot's system and the poroelastic plate model for displacements with amplitude of $6h$. With the continuous blue line we present the solution of Biot's system and with the dashed red line the solution of the poroelastic plate model.

From Fig. 5.11 one can see that for larger loads (leading to larger displacements) the approximate poroelastic plate model is not giving an accurate solution. However, the plate model is giving a solution with the same shape as the Biot's system. For particular industrial applications this model might be accurate enough.

5.2 Numerical validation of the numerical algorithms

In this section we test the accuracy of the numerical algorithms and the discretization schemes we use. As reference solutions we use available analytical solutions.

5.2.1 Validation of the Navier-Stokes-Brinkman solver

The Navier-Stokes problem (2.1) is a classical problem and analytical solutions are available for some classes of geometries and flow characteristics (see e.g. [57]). However, for general complex geometries no exact solutions are available. The Navier-Stokes-Brinkman problem is even more complex and no exact solutions have been derived for this model. In order to evaluate the accuracy of the numerical methods which we apply to solve the Navier-Stokes-Brinkman system of equations we make use of the following form of the Darcy's law (see [20])

$$Q = \frac{KA\left({p_p}^+ - {p_p}^-\right)}{\mu h}. \tag{5.7}$$

With Q we denote the total fluid discharge - the volume of fluid which is passing through a fixed cross-seciton with a surface area of A per unit of time. Woth ${p_p}^+$ we denote the effective pore pressure on the inlet side of the porous media on the surface $\delta\tilde{\Omega}_{pf}$ and with ${p_p}^-$ the the effective pore pressure on the outlet side of $\delta\tilde{\Omega}_{pf}$. We apply the Darcy's law for the full thickness of the porous media h. In general it is also valid for an arbitrary pressure drop along a given length. As we consider dead-end filtration, all of the fluid going through the inlet $\tilde{\Gamma}_{in}$ is passing through the porous media. Thus for a fixed porous media the total fluid discharge through the interface of the porous media is equal to the total fluid discharge on the interface. As we prescribe a given velocity on the inlet $\tilde{\Gamma}_{in}$ as a boundary condition (see (2.4)), we can calculate Q on the interface from the given inlet velocity. Having the thickness of the media and the permeability, we then analytically predict the pressure drop through the porous media. Recall that we consider porous media with small permeability K and continuous pressure along the interface $\delta\tilde{\Omega}_{pf}$. Therefore, the dominating pressure drop in our system is along the porous media. For this reason we compare the analytically predicted pressure drop along the porous media with the numerically obtained total pressure drop from the inlet to the outlet.

Different computational grids for a long pleat

Our aim is to create an efficient framework. We use special grids (see subsection 4.3.2) and advanced discretization techniques (see subsection 4.2.1) in order to solve

efficiently and in a robust manner the Navier-Stokes-Brinkman system of equations. It is very important to test the accuracy of the solution on different numerical grids. In this subsection we present numerical experiments for two geometries consisting of a single pleat in a rectangular domain. We consider a long pleat in this subsection and a short one in the next subsection. Both short and long pleats are used in industrial designs of filter elements. In order to see the effects of the grid on the accuracy of the solution, we fix all of the other parameters - the inlet velocity, the physical parameters of the fluid, the porous media parameters and the solver configuration.

As the first example we consider a pleat with a length of its straight part of 20 mm and thickness h of 0.5 mm. To describe the circular regions of the pleat we prescribe the inner radius r of the circular sector to 0.4 mm. To get the radius of the middle line we have to add the half thickness $\frac{h}{2}$. In this case the middle line has a radius of 0.65 mm. The inverse of this middle radius is the local curvature of the middle surface which we use in the poroelastic shell model. We position the pleat at an equal distance of 2 mm from the inlet and from the outlet of the domain Ω. We consider a fluid with a viscosity of 3.31×10^{-6} $\frac{kg}{mm\ s}$ and a density of 2.8×10^{-6} $\frac{kg}{mm^3}$. We set the inlet velocity v_{in} to 300 $\frac{mm}{s}$. In this numerical experiment we consider porous media with permeability of 3.4×10^{-5} mm^2. Remember that we consider the effective viscosity of the fluid inside the porous media to be equal to the fluid viscosity in a plain fluid region. For this set of parameters, the Darcy's law gives us an analytical pressure drop $\Delta p_{an} = 0.86125548$ kPa (we round the analytical value to its 8th digit after the decimal point). In our numerical scheme we consider the fictitious time step $\tau = 10^4$ s.

We have developed an algorithm for grid generation which allows for variation of the grid layers next to the inlet and outlet regions. We can also change the number of points on the straight and round parts of the pleat as well as the grid layers inside the porous media. For the numerical setups presented in this setup the grid regions which affect the solution the most are inside and around the porous media. For this reason we set the layers of elements next to the inlet and outlet regions to six and vary only the other parameters. Let us denote with S the number of grid vertices on the straight part of the pleat, with T the number of grid vertices along the thickness of the porous media and with A the number of grid nodes on a quarter circle of the filter tip. With N_{total} we denote the total number of grid cells for the particular grid. In table 5.3 we present the numerically obtained maximal pressure p_{max} in Ω and the minimum pressure p_{min} for different grids. We also show the relative error E_{rel} (see equation (5.8)). We consider grids with very few elements as well as very fine grids.

One can see from table 5.3 that all grids give relative difference between the numerical pressure drop and the analytical prediction of less than 0.5%. For the fluid velocity no analytical solution is available. In Fig. 5.12 we present the numerically obtained pressure field and velocity magnitude for the grid in table 5.3 with the smallest number of elements. In Fig. 5.13 we present the same data for a grid with an intermediate

number of elements $S = 20, N_{total} = 780$. In Fig. 5.14 we present the numerical solution for the finest grid from table 5.3. In all of these figures the pressure is given in kPa and the velocity magnitude is given in $\frac{mm}{s}$. The inlet is on the left side of the channel and the outlet is on the right one. As one can see the velocity solutions are very similar.

$$E_{rel} = \left| \frac{(p_{max} - p_{min}) - \left(p_p^+ - p_p^-\right)_{an}}{\left(p_p^+ - p_p^-\right)_{an}} \right| \tag{5.8}$$

S	T	A	N_{total}	$p_{max}\,[kPa]$	$p_{min}\,[kPa]$	E_{rel}
5	4	4	310	0.864032	1.1300×10^{-8}	3.223805×10^{-3}
5	4	4	336	0.864013	1.2300×10^{-8}	3.201745×10^{-3}
7	4	4	388	0.863979	1.1100×10^{-8}	3.162267×10^{-3}
10	4	4	466	0.863931	3.4000×10^{-8}	3.106535×10^{-3}
10	5	4	500	0.864050	5.5045×10^{-8}	3.244705×10^{-3}
20	5	7	780	0.863940	7.6677×10^{-8}	3.116985×10^{-3}
50	5	7	2 444	0.864424	1.1347×10^{-8}	3.678955×10^{-3}
71	5	9	3 424	0.864609	1.1054×10^{-8}	3.893758×10^{-3}
133	5	9	5 904	0.864568	1.1049×10^{-8}	3.846153×10^{-3}
201	7	9	9 488	0.864661	1.6986×10^{-8}	3.954135×10^{-3}

Table 5.3: Numerically obtained pressure drop and relative error. Different grids for a long pleat

An important result from the performed experiments is the accuracy of the solution on the grid with the fewest number of elements. With only 310 elements for the full domain and with only three grid elements along the straight part of the pleat we are able to obtain very accurate results. We achieve this accuracy as a result of the special boundary- and interface- fitted grid we use as well as the MPFA used in the FV discretization. The custom grid allows us to capture accurately the curved parts of the domain while in the same time using small number of elements for more regular regions. If one would use a Cartesian grid, a very fine grid would be needed in order to capture accurately the curved parts of the domain. This would result in a very large number of elements overall. However, the custom quadrilateral grids we use have stretched elements. Without special discretization techniques such an accurate solution is not possible.

While using as little as three elements along the straight part of the pleat gives accurate pressure drop and velocity magnitudes, this is not a practically useful grid for FPSI. Firstly, the three elements can not capture accurately the deformation of the filtering media. Secondly, the filtering media can not deform much, as this would lead to extremely stretched elements. We get accurate solutions for all of our grids

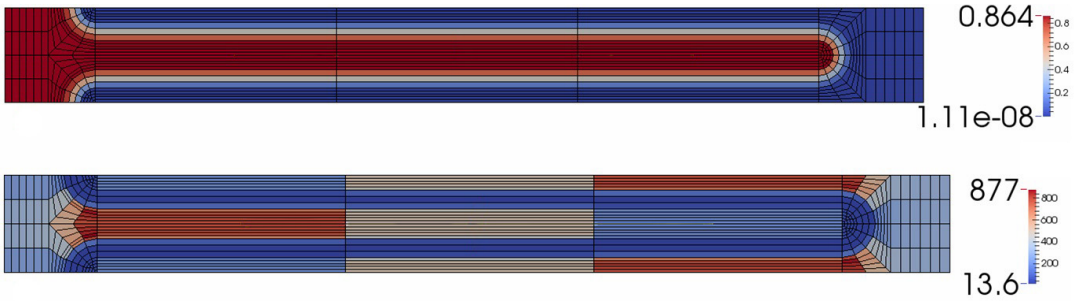

Figure 5.12: Pressure and velocity magnitude for a grid with very few elements. A long pleat

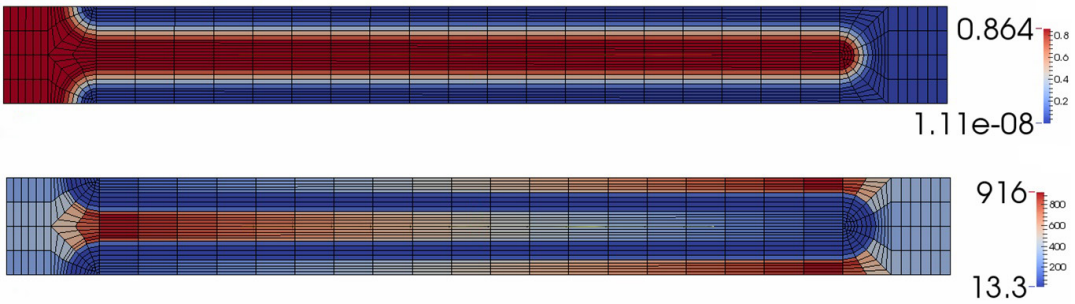

Figure 5.13: Pressure and velocity magnitude for a grid with a medium number of elements. A long pleat

with elements twenty times longer in one direction, comparing to the other. For particular geometries, fluid flows and solver parameters we can also obtain accurate solutions with elements which are fifty times longer in one direction. If the elements get stretched further we can not obtain accurate solutions anymore. This is due to the effect of the grid quality on the condition number of the linear algebraic system we got from discretization. The SAMG solver we use is a very robust one, but it still has its limitations.

Different computational grids for a short pleat

Let us now consider a different geometry of a short pleat in a rectangular channel. We reduce the length of the pleat's straight side from 20 mm to 5 mm. We do not change any of the other geometrical or physical parameters. We also consider the same fictitious time step. In this case, as the same amount of fluid is going through a smaller area of a the porous media, we have an increase in the pressure drop through the media's thickness. In this example the Darcy's law gives an analytical pressure drop of 2.69578659 kPa. In subsection 5.2.1 we present multiple grids to see the effect of changing each of the grid parameters. Due to the small difference in the

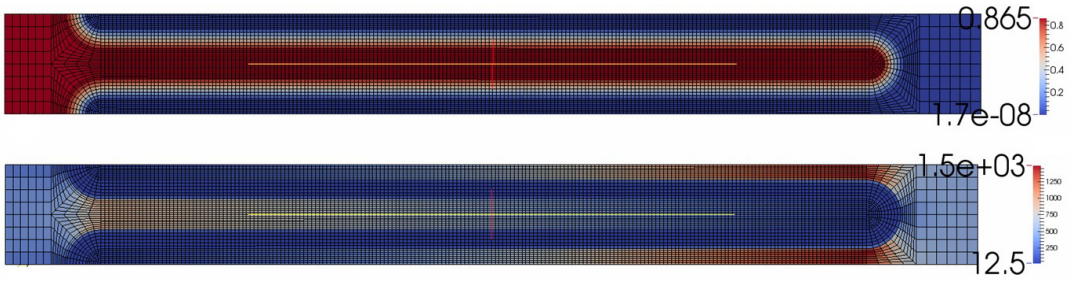

Figure 5.14: Pressure and velocity magnitude for a very fine grid. A long pleat

accuracy of grids with similar number of elements, in this subsection we vary the grid parameters more rapidly. The maximum and minimum pressure drop along with the relative difference between the numerical solution and analytical prediction we present in table 5.4.

S	T	A	N_{total}	$p_{max}\,[kPa]$	$p_{min}\,[kPa]$	E_{rel}
8	4	4	390	2.72857	2.2672×10^{-8}	1.216098×10^{-2}
30	4	5	962	2.72652	2.2672×10^{-8}	1.140054×10^{-2}
90	5	7	4 032	2.73108	1.3599×10^{-8}	1.309206×10^{-2}
150	7	8	7 244	2.73171	3.4048×10^{-8}	1.332576×10^{-2}

Table 5.4: Numerically obtained pressure drop and relative error. Different grids for a short pleat

In this numerical example the difference between the numerically obtained pressure drop and the analytical prediction is around 1%. To monitor the accuracy of the velocity we plot the velocity magnitude for different grids. We consider the solution on the finest grid as a reference solution. We present the pressure field and velocity magnitude for the roughest and finest grids from table 5.4 in Fig. 5.15 and Fig. 5.16, respectively. In these figures the pressure is presented in kPa and the velocity magnitude is given in $\frac{mm}{s}$. The inlet is on the bottom of the channel and the outlet is on the top of the channel.

The velocity magnitudes have the same characteristics in the two cases presented. Although we present selected figures in this work, we monitor the accuracy of the numerical solutions with respect to pressure and velocity in all numerical experiments we perform.

Different viscosity and permeability

So far we have presented the accuracy of the numerical solutions of the Navier-Stokes-Brinkman equations for different grids on two different geometries. In table 5.5 we

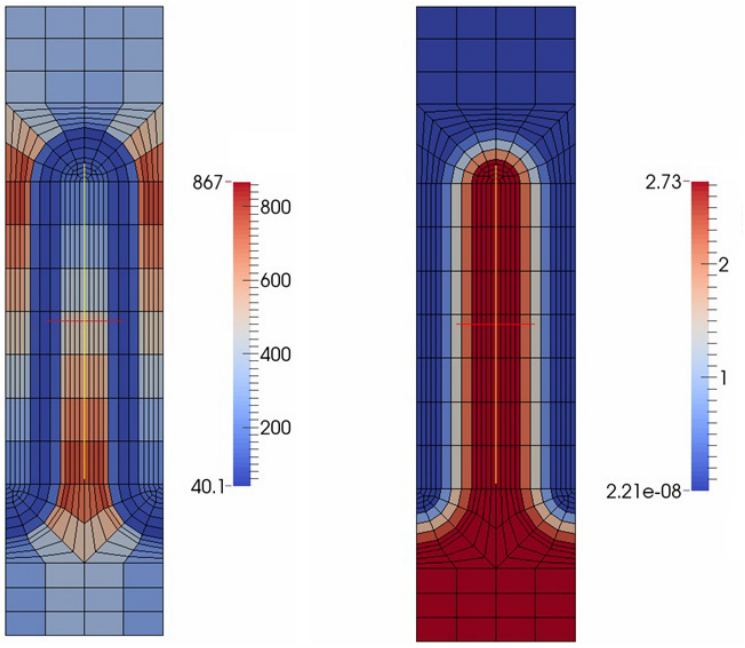

Figure 5.15: Pressure and velocity magnitude for a grid with very few elements. Short pleat

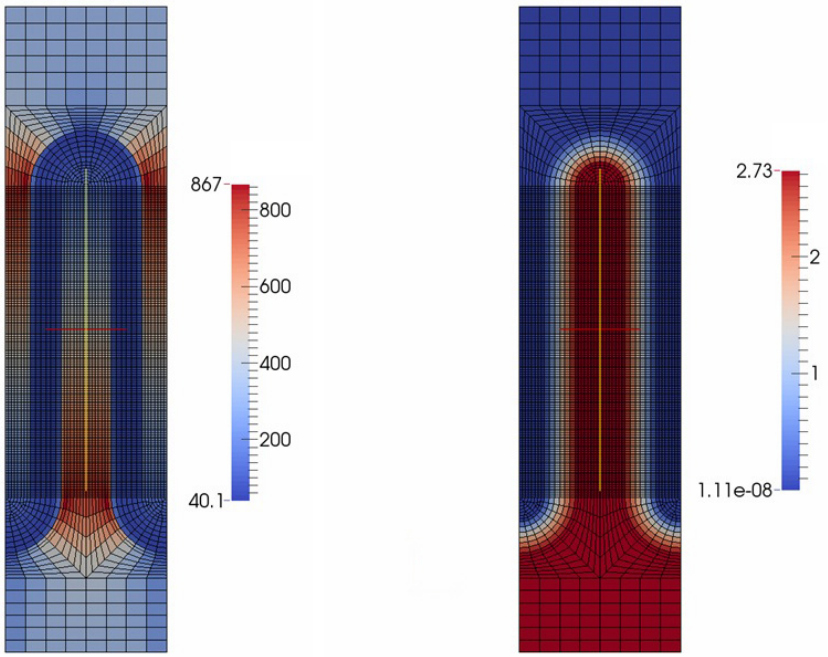

Figure 5.16: Pressure and velocity magnitude for a very fine grid. Short pleat

demonstrate the accuracy of the solution for sets of viscosities and permeabilities. We choose the geometry and grid presented in Fig. 5.13. We consider an inlet velocity of 300 $\frac{mm}{s}$, a fluid density of 2.8×10^6 $\frac{kg}{mm^3}$ and a fictitious time step $\tau = 10^5$ s. We vary the permeability and the viscosity by the same factor so that we preserve the analytical prediction of the pressure drop $\left(p_p^+ - p_p^-\right)_{an} = 0.86125548$ kPa (see equation (5.7)).

$\mu \left[\frac{kg}{mm\ s}\right]$	$K\left[mm^2\right]$	$p_{max}\left[kPa\right]$	$p_{min}\left[kPa\right]$	E_{rel}
$3.31\ 10^{-7}$	3.4×10^{-6}	0.863946	1.49×10^{-9}	3.124508×10^{-3}
$1.1\ 10^{-6}$	1.13×10^{-5}	0.863870	1.1×10^{-9}	3.036265×10^{-3}
$3.31\ 10^{-6}$	3.4×10^{-5}	0.863937	3.31×10^{-9}	3.114059×10^{-3}
$9.93\ 10^{-6}$	1.02×10^{-4}	0.863930	9.71×10^{-9}	3.105931×10^{-3}
$3.31\ 10^{-5}$	3.4×10^{-4}	0.863897	7.66×10^{-9}	3.067614×10^{-3}

Table 5.5: Numerically obtained pressure drop and relative error. Different viscosity and permeability

As one can see from the data in table 5.5, varying the permeability and the viscosity does not affect the accuracy of the solution.

Different density

The last parameter that we vary is the fluid density ρ - see table 5.6. For this numerical setup we consider the geometry and grid presented in Fig. 5.13. We set the inlet velocity to 300 $\frac{mm}{s}$, the viscosity to 3.31×10^{-6} $\frac{kg}{mm\ s}$ and the permeability to 3.4×10^{-5} mm^2. For this set of parameters the analytical prediction of the pressure drop of $\left(p_p^+ - p_p^-\right)_{an} = 0.86125548$ kPa.

$\rho \left[\frac{kg}{mm^3}\right]$	$\tau\,[s]$	$p_{max}\left[kPa\right]$	$p_{min}\left[kPa\right]$	E_{rel}
$1\ 10^{-8}$	10^3	0.864020	2.17×10^{-9}	3.209872×10^{-3}
$1\ 10^{-7}$	10^3	0.863987	1.18×10^{-8}	3.171556×10^{-3}
$1\ 10^{-6}$	10^5	0.863948	1.18×10^{-9}	3.126273×10^{-3}
$5\ 10^{-6}$	10^5	0.863926	-1.33×10^{-5}	3.100729×10^{-3}
$7.5\ 10^{-6}$	10^5	0.863933	8.87×10^{-9}	3.108857×10^{-3}
$1\ 10^{-5}$	10^5	0.863935	1.18×10^{-8}	3.111179×10^{-3}

Table 5.6: Numerically obtained pressure drop and relative error. Different density

As presented in table 5.6 we achieve good accuracy with different values of the fluid density. With the change of the density we vary also the fictitious time step τ. Remember that we use the fictitious time step as a stabilizing parameter. In order to achieve accurate results we have to choose the τ depending on the inlet velocity, the

permeability of the porous media and the fluid density. In this section we have shown consistent accuracy of the solution independent of changes in the geometry, the grid and the physical parameters. The effect of the fictitious time step on the accuracy of the solution is outside the scope of this work.

5.2.2 Validation of the elasticity solver

In subsection 5.1.2 we tested the validity of the elastic plate model (3.20) against Biot's system. In this section we measure the accuracy of the linear elasticity solver against an analytical solution of the Biharmonic equation. We also compare the computational time required to solve the discretized plate model in comparison with the discretized Biot's system.

Validation against an analytical solution

Westphal, Andrä and Schnack have derived in [48] an analytical solution for the Biharmonic equation with a constant right hand side on a circular domain. The solution is in the form of a series. Up to the knowledge of the author no analytical solutions have been derived for the more complex cases of non-uniform load or/and more complex geometries. Having the solution in a form of a series makes it hard to use the L_2 or the L_∞ norm to validate our numerical solutions. However, the analytical displacement of the center of the circular domain can be easily obtained. Let us consider the normalized displacement at the center point 0:

$$\overline{w}(0) = \frac{64D}{R^4\left(f_n^+ - f_n^-\right)} w(0). \tag{5.9}$$

With R we denote the radius of the circular domain. For the normalized displacement the analytical solution gives $\overline{w}(0) = 1$. In table 5.7 we present a comparison between a series of numerical solution and the analytical value of 1 for the normalized displacement in the center point. We consider a cylindrical domain with a radius $R = 2.5\ cm$ and a thickness $h = 0.05\ cm$. We use a material with Young's modulus $E = 2 \times 10^5\ Pa$ and Poisson's ratio $\nu = 0.33$. We load the poroelastic body uniformly

$$\mathbf{S}(\mathbf{x}) = \begin{cases} 9\ Pa\ \mathbf{n}, & \mathbf{x} \in \Gamma_+ \\ 0\ Pa\ \mathbf{n}, & \mathbf{x} \in \Gamma_- \end{cases}, \quad P(\mathbf{x}) = \begin{cases} 9\ Pa, & \mathbf{x} \in \Gamma_+ \\ 0\ Pa, & \mathbf{x} \in \Gamma_- \end{cases}. \tag{5.10}$$

In table 5.7 we present the number of elements in the different triangulations, the Degrees of Freedom (DOF) of the discretizations, the numerical normalized displace-

ments $\overline{\omega}(0)$ and the numerical errors. To obtain the triangulations we use the build-in COMSOL package. As one can see, the use of Argyris type of elements in the FEM scheme leads to degrees of freedom about six times more than the elements in use. As a numerical error we consider the difference between the analytical and numeral values of the normalized displacement in the center point. Due to the shape of the solution this is comparable to the error in *sup* norm.

Triangles	DOF	$\overline{\omega}(0)$	Error
7 516	34 439	0.9942	0.0058
16 446	74 909	0.9990	0.0010
28 702	130 355	0.9996	0.0004
44 190	200 345	0.9998	0.0002

Table 5.7: Convergence of the numerical scheme due to the mesh size

The data in table 5.7 shows superlinear numerical grid convergence. We use the results from this comparison to the analytical solution to control the discretization error in similar and more complicated geometries.

Computational efficiency of the reduced models

In our comparison with the Biot's system, the plate model has shown to be accurate for variety of plate thicknesses and deformation amplitudes. When the plate model is applicable it is important to know how much computational time we save by using it. The Biot's system is a second order system of PDEs with four unknowns defined on a 3D domain. This problem is reduced to a forth order PDE with one unknown defined on a 2D domain. The unknowns and the domain of interest are reduced which reduces the degrees of freedom in the discretized problem. On the other hand the order of the system is increased. In terms of finite elements this is a requirement for smoother elements of higher order and leads to an increase in the degrees of freedom.

Let us consider the same geometry, material parameters and loads as in the comparison of poroelastic plate model against an analytical solution. In table 5.8 we describe the setting of the numerical experiments and the computational time required to obtain a solution. For the Biot's system we use a grid with four layers of triangular prisms. We use the triangulation of the base of the cylinder as the triangulation of the domain of for the plate problem. For this setting the degrees of freedom in the approximation of the poroelastic plate model are 12.9 times less than the degrees of freedom in the discretization of the Biot's system. Note that using four layers of prisms gives an accurate solution for the simple geometry of a thin poroelastic cylinder. In more complex geometries one might need more prism layers to achieve an accurate numerical solution. In such case the DOF will decrease even more.

We perform the study of the computational efficiency on a single processor using a single core. The discretization of the poroelastic plate model gives a small number of DOF. We use a direct solver to solve the linear system resulting from the discretization of the poroelastic plate equation. The build in MUMPS solver in COMSOL shows its full potential when used on clusters with large and very large number of cores. However, due to its robustness we use it for also for this numerical experiment set on a single core.

The discretization of the Biot's system leads to a much larger algebraic system of equations. Due to memory restrictions, using a direct solver is not feasible for such a large system. To solve this system, we use the GMRES (Generalized Minimal Residual) solver build in COMSOL with a geometric multigrid preconditioner.

	Plate model	Biot's system
Mesh Elements	Triangles	Triangular prisms
Type of finite elements	C1 Argyris type	P2-P1
Number of finite elements	16 980	67 920
Degrees of freedom	74 909	967 898
Solver	Direct - MUMPS	Iterative - GMRES
Computational time	9s.	725s.

Table 5.8: Setting of the numerical experiments.

The computational times for the two numerical experiments in table 5.8 show a large increase of the computational efficiency when using the approximate poroelastic plate model instead of the Biot's system. In this particular experiment we gain a speedup of eighty times. This example demonstrates the potential of poroelastic plate and shell models. For more complex domains requiring significantly more elements we expect even further improvement in the computational time when poroelastic plate and shell models are used.

5.2.3 Validation of the iterative algorithm for FPSI

In the previous sections of this chapter we have tested the accuracy of the fluid flow solver and the elasticity solver independently. In this section we test the convergence of the iterative algorithm coupling the two systems.

Validation of the linearly elastic shell model

Let us consider the initial geometry and the initial grid presented in Fig. 4.6. In Fig. 4.1 we show the same initial geometry without the computational grid for more clear representation of the domains of interest. Let us consider a fluid with viscosity

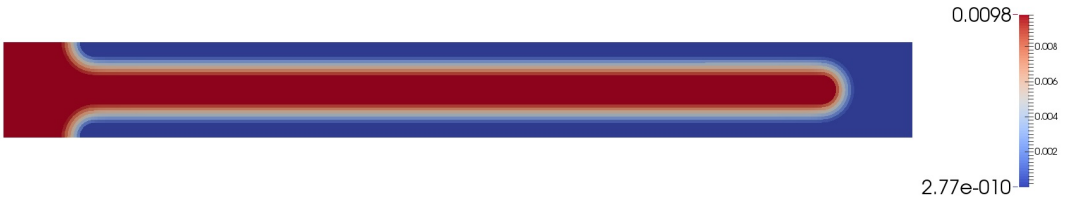

Figure 5.17: Pressure in the initial state

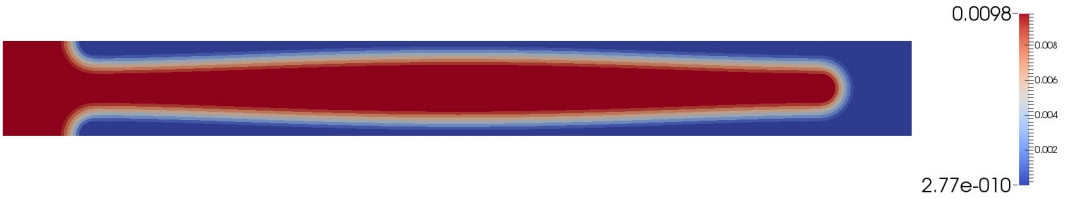

Figure 5.18: Pressure after displacement

$\mu = 3.31 \times 10^{-6}\ \frac{kg}{mm\ s}$ and density $\rho = 8.2 \times 10^{-7}\ \frac{k}{mm^3}$. We consider a poroelastic material with permeability $K = 1 \times 10^{-6}\ mm^2$, Young's modulus $E = 2 \times 10^5\ Pa$ and Poisson's ratio $\nu = 0.33$.

In Fig. 5.17 we present the pressure distribution in the initial (non-deformed) configuration. The pressure is given in kPa.

The pressure drop through the filtering media is $9.80010 \times 10^{-3}\ kPa$. We use this pressure drop to determine the load in the poroelastic shell model. The numerical solution of the poroelastic shell models gives us the displacements in the nodes on the middle line of the porous material. Using the assumption of thickness preservation, we reconstruct the displacements in all of the computational nodes in the porous material. In Fig. 4.2 we present the position of the pleat after deformation.

Having the displacements of the porous media, we stretch the grid (without remeshing). The resulting grid in the deformed configuration is presented in Fig. 4.5. A more detailed view of the right side of this grid is presented in Fig. 4.8. With the updated grid we run again the fluid solver in order to update the velocity field and the pressure distribution. In Fig. 5.18 we present the pressure distribution in the deformed configuration. The pressure is given in kPa.

The pressure drop through the filtering media after it has been deformed is $9.79378 \times 10^{-3} kPa$. This decrease is expected as the deformation of the porous media leads to increase in the filtration area. However, the decrease in the pressure drop is very small. Although the deformation of the pleat is substantial, the pressure had decreased by 0.64%.

We use the updated value of the pressure drop to numerically obtain the displacements of the porous media. As in the previous iteration, we use the poroelastic shell model. First we determine the displacements of the grid nodes in the middle surface. Then we reconstruct the domain and we stretch the computational grid. The change in the domain is so small, that in the third iteration of the flow solver we once again obtain a pressure drop of $9.79378 \times 10^{-3} kPa$.

Note that only two iterations are required to obtain the steady state solution of the FPSI problem. The third iteration we perform only to validate the convergence of the iterative scheme. We observe such a fast convergence for a wide range of inlet velocities, fluid parameters and material parameters in the problem of a single poroelastic pleat in a rectangular channel. This demonstrates the efficiency of the iterative approach we use to solve the FPSI system of equations in the case of a single pleat in a rectangular channel. It should be noted that for more complex configurations (e.g. multiple pleats in a complex domain) we do not expect always to have convergence within two-three iterations.

Validation of the poroelastic plate model

We have shown very fast convergence of the iterative scheme we use for the case of a single poroelastic pleat in a rectangular channel. However, we achieve convergence within the accuracy of the grid so fast, that we can not observe the rate of convergence. For the more simple problem of an initially flat porous media in a rectangular channel we can use a much finer grid to reduce the discretization error as close as possible to the machine error.

Let us consider a channel with a width of 30 mm and a length of 70 mm with a porous media in the middle of the channel with a thickness of $h = 1.2$ mm (see Fig. 5.19 left). Let us consider a fluid with dynamic viscosity of 2.8 $mPa\ s$ and density of 830 $\frac{kg}{m^3}$, a porous material with permeability of 3.36×10^{-11} m^2 and flexural rigidity $D = 7.0308$ $mm^3\ Pa$ and an inlet velocity of 1.5 $\frac{cm}{s}$. All of the variables are chosen to match a physical experiment which we present in the next section 5.3.

In order to achieve maximal accuracy we use a Cartesian grid for the fluid flow problem. We use a grid with 300×700 grid elements and we measure the pressure drop with sixteen digits of accuracy.

In the left side of Fig. 5.19 we present the position of porous material before and after displacement takes place. In the right side of this figure we present the pressure distribution before and after deformation.

As one can see in Fig. 5.19, the deformation of the porous media is small. The change in the pressure drop is less than 1%. However, using a very fine grid and

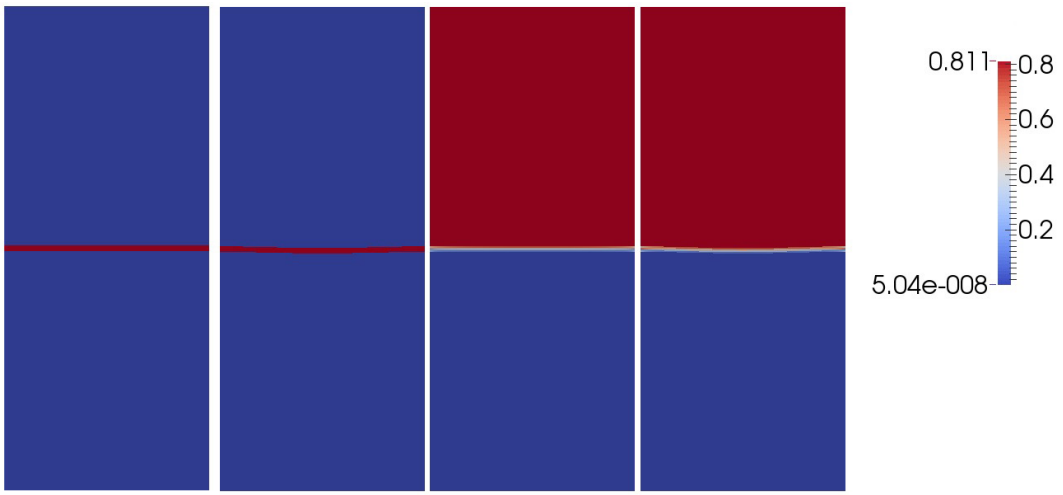

Figure 5.19: Initially flat media in a channel before and after deformation. Left - geometry, right - pressure field

saving the numerical data with very high accuracy allows us to capture the difference in pressure drop and filter deformation through multiple iterations. As a converging criteria we use the relative (to the previous iteration) change in the displacement of the central point in the filtering media. In Fig. 5.20 we present the relative change of the deformation of this point within ten iterations. We start with an iteration of number zero and present the convergence for the iterations one to nine. The x-axis of the plot is Cartesian and the y-axis of the plot is logarithmic. Fig. 5.20 shows superlinear rate of convergence of the iterative method.

5.3 Numerical validation against a physical experiment

So far we have shown the validity of the approximate mathematical models, testing them against the governing equations, and the accuracy and efficiency of our numerical methods. However, if the governing system of equations does not resemble the behavior of real physical systems, the framework that we have developed can not be applied in practical applications. For example, the Biot's system has been developed to simulate the behavior of river beds. The materials used in dead end filtration are paper-like (consisting of woven or non-woven fibers) and it is very important to understand if the Biot's system can be used to accurately simulate such a different porous material. The Navier-Stokes-Brinkman system of equations have shown to be an accurate representation for filtration processes with non-deformable media, but no studies have been done to validate this model for deformable media. For this reasons, a very important part of our study is to validate our numerical framework against a physical experiment. In this section we perform this validation.

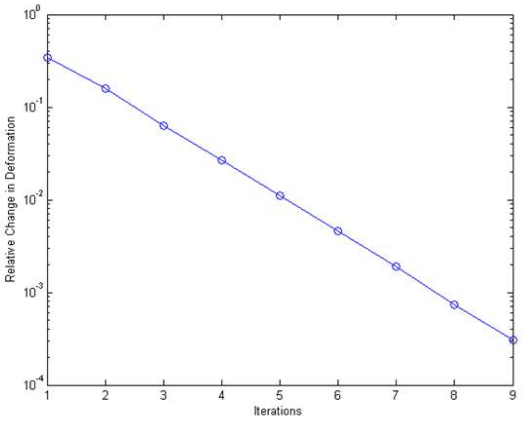

Figure 5.20: Numerical convergence of the iterative method

5.3.1 Experimental setup

To accurately measure the deformation of a filter during filtration is not an easy task. Industrial oil filters often have a metal housing. This does not allow to optically monitor the displacement of the filtering media in an industrial filter. There are different approaches to overcome this problem. One approach is to create a test bench with optically clear materials. In the physical experiments performed by the LMFA laboratory in Lyon, France, this approach has been used.

Along with an optically clear housing for the filter, also an optically clear synthetic oil has been used. This oil has dynamic viscosity of 2.8 $mPa\ s$ and density of 830 $\frac{kg}{m^3}$ at room temperatures. These values are in the range of dynamic viscosities and fluid densities of motor oils at operating temperatures. Using such an oil gives an accurate representation of industrial filters.

In this test bench a rectangular channel with an initially flat porous media has been used - see Fig. 5.21. We should note that clamping the porous material is also a complicated task. If the porous media is clamped weakly, leaks might occur. Due to weak clamping the filter may detach from the housing. If the porous media is very strongly clamped, the material fibers may break and the filter will no longer be attached to the housing. In the production of industrial oil filters with initially flat filtering media, special machines are used to bend the metal housing with the filtering media in order to achieve strong, but non-destructive clamping. For the physical experiments presented in this paper, rubber bands have been used to prevent leaks and to ensure strong clamping. The rubber band in black color and the white filtering media can be seen in the left side of Fig. 5.21.

High quality cameras are used to optically measure the displacement of the porous media - see Fig. 5.22. A laser with a cylindrical optical element is used to illuminate

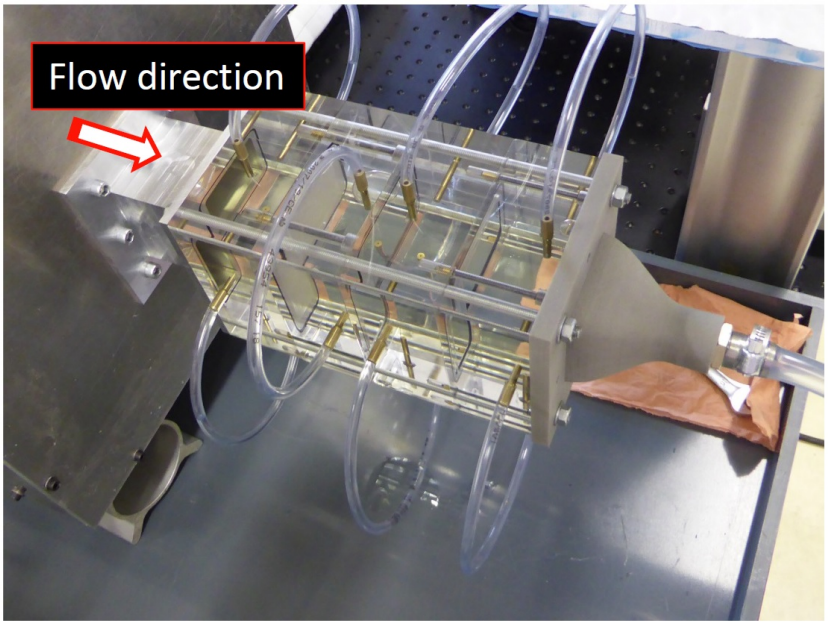

Figure 5.21: The rectangular channel in the physical experiments performed by the LMFA laboratory in Lyon, France. The photo is courtesy of LMFA

the porous media with a planar sheet of light - see the left picture in Fig. 5.22. A mirror is used in order to fully illuminate deformed filtering media. A camera situated above the channel captures an image of the illuminated part of the porous media - see Fig. 5.22 left.

Two lenses can be mounted on the high quality camera. A lens with small magnification factor (see Fig. 5.22 middle) can be used to capture a photograph of the filtering media's full width. A sample photograph captured with this lens is shown in the left side Fig. 5.23. Two images are given - the initial non-deformed state of the filter and the deformed position of the filter. It should be noted that this picture is only for illustrative purposes. For the validation of numerical against physical experiments, we consider displacements of the order of the porous media thickness h. In such case the deflection of the porous media can not be captured accurately with such a wide lens.

To capture accurately small displacements of the porous media, a lens with high magnification factor is being used - see Fig. 5.22 right. Sample images photographed with this lens are shown in the right side of Fig. 5.23. Due to the rough surface of the porous media there is no sharp edge in the picture. An image processing software is used to determine the mean displacement in a small area captured by the camera. The shape of the filtering media after deformation is measured by multiple photos in different small regions of the filter.

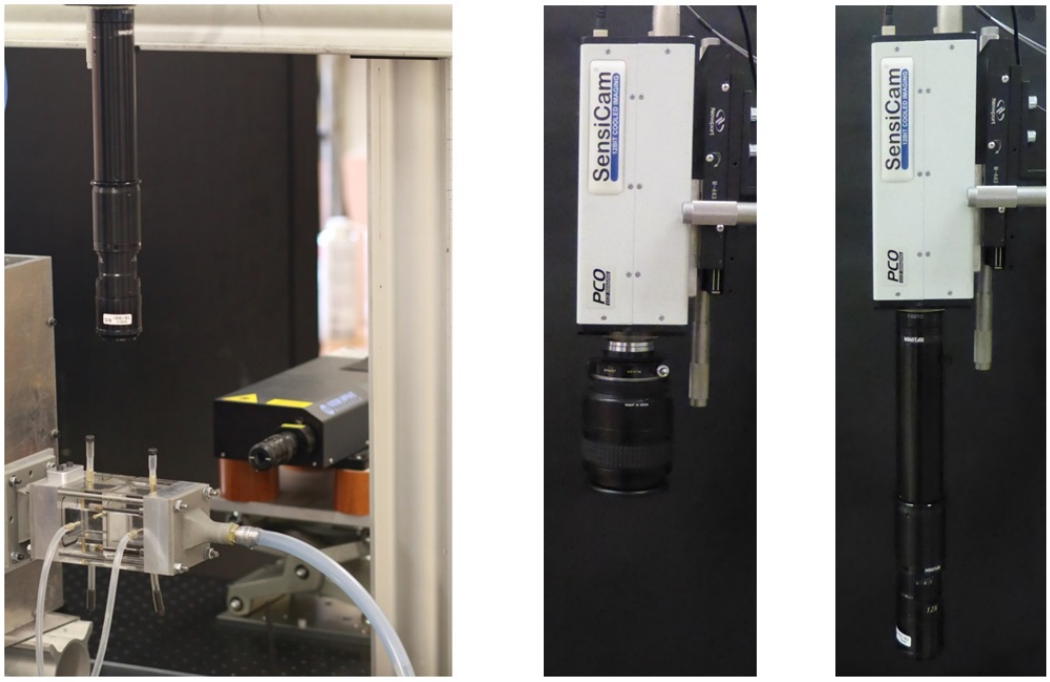

Figure 5.22: The cameras used in the physical experiments performed by the LMFA laboratory in Lyon, France. The photos are courtesy of LMFA

The deflection of the porous media clearly depends on the fluid flux through the material. The oil in the test bench is circulated by a pump. The fluid flux is measured in the pump outlet. To minimize the turbulence created by the pump, the fluid is run through multiple grids in a large container before it enters the porous media. The test bench also allows to measure the fluid pressure 3.5 cm before and after the porous media. The width of the channel is 3 cm.

The physical experiment provides the deflection of the porous media in multiple points from a cross-section. In the results presented in this work only the central cross-section is being considered. We perform numerical simulations for the same cross-section. The width of the channel in the numerical simulation is 3 cm likewise the width of the channel in the physical experiment. For the numerical experiment we consider a channel with length of 7 cm with the porous media in the middle of the channel. This way we can resemble accurately the pressure drop measured in the physical experiments.

5.3.2 Parameter identification

In order to compare the physical experiments to our numerical studies we have to know the properties of the porous material. The permeability of the filtering media is measured and controlled by the filter manufacturers. Usually the pressure drop

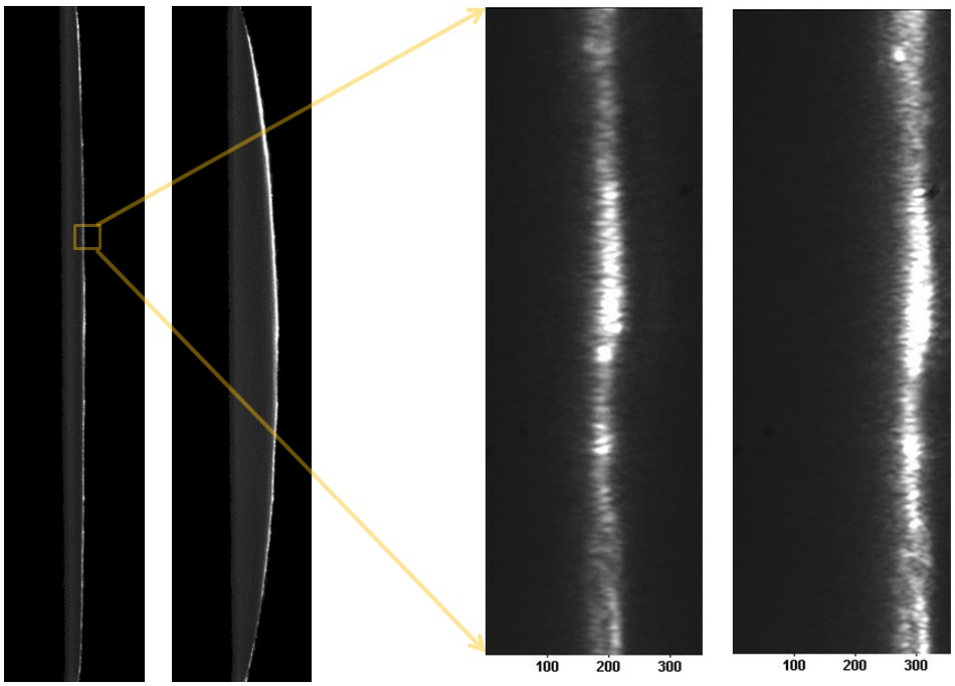

Figure 5.23: Sample deformations measured by the LMFA laboratory in Lyon, France. The photos are courtesy of LMFA

through the media is measured for a given fluid flux. Then using the Darcy law, the media permeability is calculated. The filtering material used in the physical experiments in LMFA has permeability $K = 3.36 \times 10^{-11}\ m^2$.

Measuring the mechanical properties of a saturated porous media is a complex problem. Standard test benches measuring the mechanical properties of different materials do not allow for a wet material to be measured. The liquid would simply leak out of the porous material. Note that a saturated filtering media can have mechanical properties different in orders of magnitude comparing to the same media when it is not saturated. Usually the saturated materials are much stronger. Thus, measuring the mechanical properties of the saturated porous media is a very important problem.

In this work we focus on the development of a numerical framework to solve the direct problem of filter deflection due to fluid flow. We can perform multiple direct simulations to solve the inverse problem - to find the mechanical parameters of porous material given its deflection. We have all of the parameters except of the flexural rigidity D. Note that for the initially flat filtering media we use the poroelastic plate model and the flexural rigidity is the only mechanical coefficient in the equation. From D only the ratio between the Young's modulus and Poisson's ratio can be determined. To calculate both of these mechanical parameters additional information is needed.

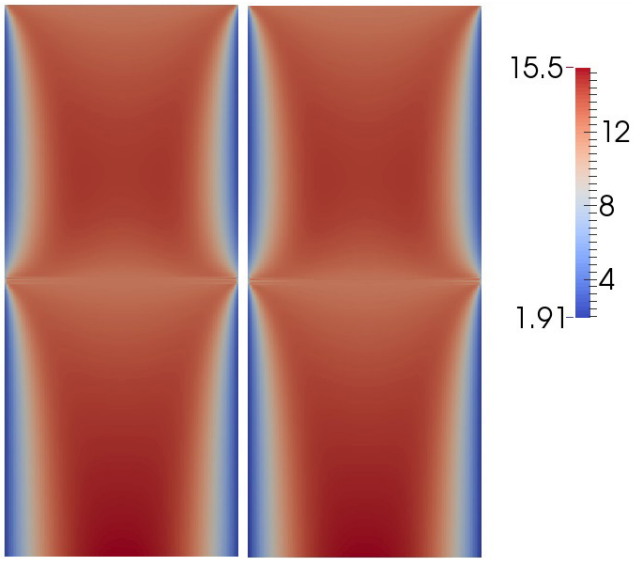

Figure 5.24: Initially flat media in a channel before and after deformation. Velocity magnitude

For inlet velocity $v_{in} = 12.0889\ \frac{mm}{s}$, taking the displacement in the central point of the filter, we determine the flexural rigidity of material to be $D = 7.0308\ mm^3\ Pa$. The numerically obtained media displacement and pressure distribution are presented in Fig. 5.19. In Fig. 5.24 we present the velocity magnitude before and after deformation. The velocity magnitude is given in $\frac{mm}{s}$.

Fig. 5.24 shows the 3.5 cm before the filtering media to be enough for Poiseuille flow to be established. For faster flows the inlet should be placed even further from the media to ensure no artificial numerical effects on the flow from the inlet boundary conditions.

5.3.3 Comparison of physical and numerical results

For a more accurate representation, in Fig. 5.25 we present the comparison between the physical and the numerical experiments in an area close to the filtering media. With the white squares we present the displacement of the porous media measured in the physical experiment. With the horizontal multicolored lines we present the numerical position of the porous media after deflection. The colors represent the numerically obtained pressure. We also plot the streamlines and the fluid pressure in the plain flow regions.

Fig. 5.25 shows very good agreement between the numerical and physical experiments. Note that we have used a measurement in only one point to determine the mechanical

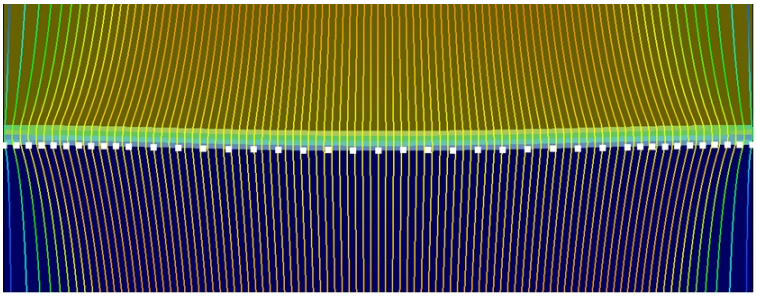

Figure 5.25: Comparison of the numerical and physical experiments for smaller displacement

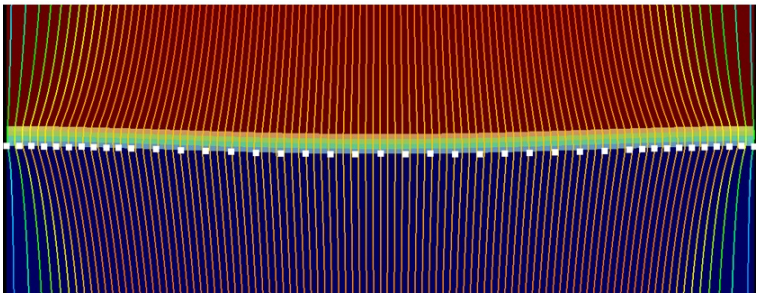

Figure 5.26: Comparison of the numerical and physical experiments for larger displacement

parameters of the media. As now we have all of the physical parameters of the system, we can compare the numerical and physical results for different inlet velocities resulting in different amplitudes of deflection. In Fig. 5.26 we present a comparison between physical and numerical results for inlet velocity $v_{in} = 15.8544\ \frac{mm}{s}$. Once again we present the data from the physical experiments with white squares.

Comparing Fig. 5.25 and Fig. 5.26 one can see an increase in the pressure drop with the increase of inlet velocity. This is a behavior predicted by the Darcy law. Even for the larger magnitude of displacement the numerical results accurately capture the deformation of the porous media due to the fluid flow through it. Note that for the second example we have not used any measurement to calculate any parameters.

In table 5.9 we compare the numerically obtained pressure drop and maximal displacement of the filtering media against physical experiments for different inlet velocities. The inlet velocity is given in $\frac{mm}{s}$, the pressure drop through the filtering media is given in Pa and the maximal displacement (the displacement of the center point) is given in μm.

Table 5.9 also shows very good agreement between the physical and numerically obtained results. Note that in the physical experiment, the camera is moved manually

Inlet velocity v_{in} $\left[\frac{mm}{s}\right]$	Numerical pressure drop	Physical pressure drop	Numerical max. displ.	Physical max. displ.
3.6553	245.271	272.9862	73.5855	73.9
7.6630	513.186	510.1056	153.9650	145.4
12.0890	809.473	793.0548	242.8558	240.8
15.8544	1064.68	1093.9374	319.4223	328.2

Table 5.9: Pressure drop in Pa and maximal displacement for different inlet velocities in μm. Numerical results and measurements from a physical experiment

along a rail to take photographs of different regions. The differences between the physical and numerical results are all within the accuracy of the experimental test bench.

From the results in this section, we can determine that the mathematical models we use accurately describe the physical phenomenon of FPSI in the case of dead end filtration.

Chapter 6

Applications

In section 5.3 we have shown one application of the FPSI framework we have developed. We can use the efficient framework to perform parameter identification for the mechanical properties of saturated porous materials. In this chapter we show further applications of the numerical algorithms developed in this work.

6.1 Determining the effects of deformation in fiters

In subsection 5.2.3 we have performed numerical simulations for the deflection of a poroelastic pleat in a rectangular channel. In Fig. 5.17 and Fig. 5.18 we have the pressure distribution before and after the deflection of the pleat. The difference in the pressure drop is not large which is the reason for the fast convergence of the iterative scheme we use. If one considers only this result, it might seem that the deformation of the porous media does not affect the fluid flow substantially.

Let us now consider the velocity field of the fluid before and after deformation takes place. In Fig. 6.1 and Fig. 6.2 we present the velocity magnitude in the initial and in the deformed configuration, respectively. In both of the figures the velocity magnitude is given in $\frac{mm}{s}$.

Figure 6.1: Velocity magnitude in the initial state

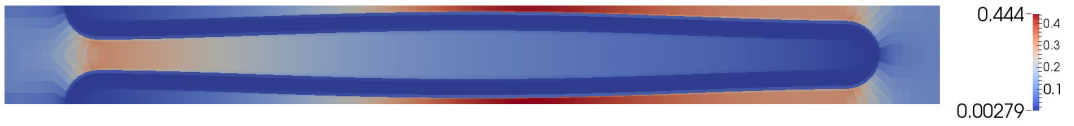

Figure 6.2: Velocity magnitude after displacement

The comparison of Fig. 6.1 and Fig. 6.2 shows a significant change in the fluid flow with the deformation of the porous media. The magnitude of the deformation is only of the order of the small thickness of the media. However, the distance from the straight part of the pleat to the top and bottom parts of the channel is also of this order. Thus, even a small change in the position of the porous media can lead to a large change of the flow distribution.

In filtration processes the flow distribution determines the path of the solid pollutant particles. A change in the fluid flow may lead to a part of the filtering media not being used for filtration of the pollutant. Such large velocities as in Fig. 6.2 may even lead to solid particles being washed out from the porous media. This numerical experiment shows us how important it is to incorporate the fluid deformation in the numerical simulation of dead-end filtration processes.

In this section we present the deflection of a singe pleat. This is just an illustration. In industrial filters many pleats are being used in a filter cartridge (see Fig. 1.1 left). This is done to increase the filtration area and to decrease the pressure drop through the filter. Increasing the filtering area increases the filtration efficiency and the life capacity of the filter. The decrease in pressure drop allows smaller and more power efficient pumps to be used to circulate the oil. Using many pleats in a filter cartridge leads to small distances between the straight parts of different pleats. Thus, we expect the deformation of pleats in a filter cartridge to have similar effect as in the example presented in this section.

By including the filter deformation in pleated filter efficiency simulations, one can accurately determine the optimal number of pleats in a fixed housing.

6.2 Simulation of a round pleated cartridge

In subsection 4.3.2 we have presented the algorithm we use to create interface- and boundary- capturing quadrilateral grids. So far we have presented numerical simulations of a single pleat in a rectangular channel. As shown in Fig. 4.11, we have extended the grid generation algorithm to round filter cartridges with multiple pleats. In Fig. 4.10 we show the full computational domain for the cross-section of a round pleated filter cartridge. In this section we present a numerical simulation for this domain.

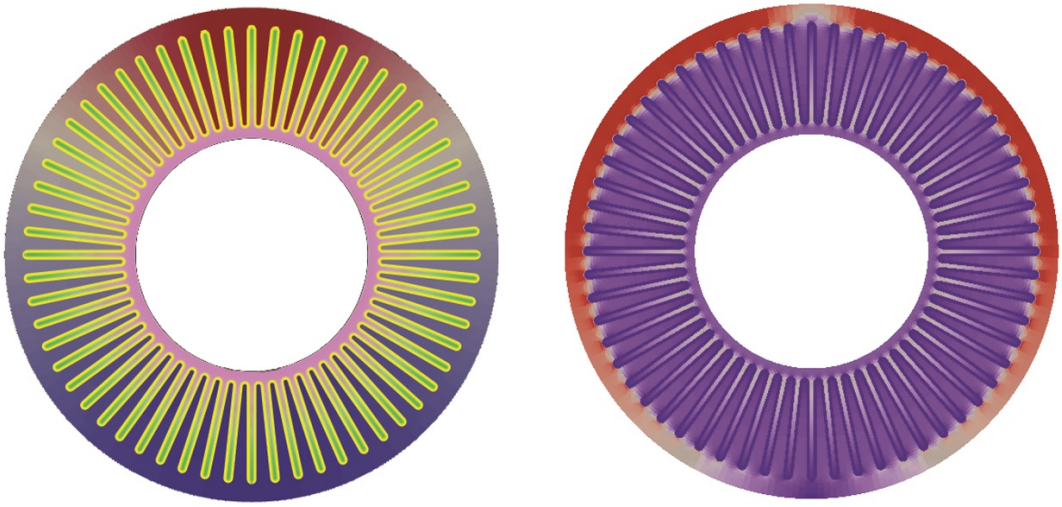

Figure 6.3: Pressure distribution (left) and velocity magnitude (right) for a cross-section of a filter with 60 pleats

We consider a narrow inlet at the top side of the filter housing. This is representative for a cross-section near a pipe inlet on the side of a cylindrical filter housing. As an outlet we consider the inner circular boundary of the domain. In Fig. 6.3 we present the pressure distribution and the velocity magnitude for one set of physical parameters and inlet velocity. We have used synthetic (non-physical) fluid and material parameters to demonstrate qualitatively the behavior of such filters.

On the left side of figure 6.3 we present the pressure distribution in the inlet and outlet region of the filter element cross-section. With yellow we present the filtering media. With colors from red (high pressure) to blue (low pressure) we present the pressure distribution in the inlet region of the porous media. The pressure near the inlet is high and it is decreasing towards the lower side of the filter. In the outlet region we present the pressure distribution with colors from green (high) to purple (low). In the outlet region the pressure distribution has a radial symmetry. This leads to a non-uniform load of the filter pleats.

As the shell models have shown to be inaccurate for non-uniform load, we have not performed numerical simulations for the deformation of the pleats in this example. In this case the governing Biot's system should be used to determine the deformation of the filtering media.

In the right side of Fig. 6.3 we present the numerically obtained magnitude of the fluid velocity. As we use porous media with small permeability, the flow distribution along the filtering media is close to uniform. This leads to a fast fluid flow near the inlet and slower fluid flow in the part of the filter further away from the inlet.

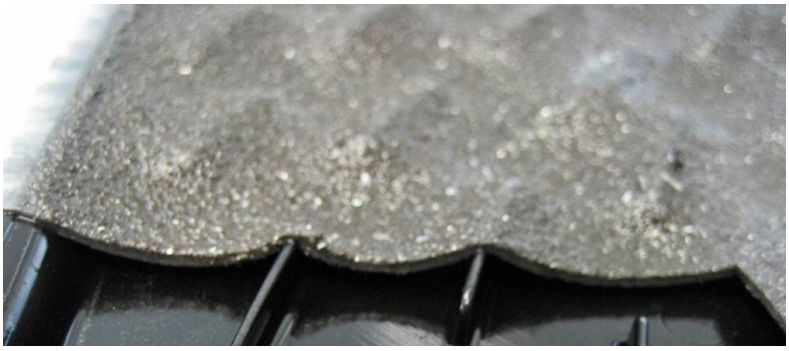

Figure 6.4: Bending of a filter under extreme loading conditions. The photo is courtesy of IBS Filtran

The example presented in this section shows how we can use the grid generation algorithm developed in this work to simulate physically relevant domains.

6.3 Poroelastic plates in complex geometries

In section 5.3 we have shown the accuracy of the poroelastic plate in FPSI simulations for simple domains. In this section we demonstrate how the poroelastic plate model can be used in more complex domains.

In Fig. 6.6 we present the deflection of an initially flat filtering media due to extreme operating conditions. The media in this figure is being supported by a rib structure like the one presented in the right side of Fig. 1.1. Due to a fatal break in an automatic car transition the filter has been clogged with contaminant. This clogging has increased the pressure drop through the filter which leads to the deflection of the porous material. Although the deflection of the porous material is comparable to the small thickness of the material, the channels underneath the filter have been reduced, which changes the operation of the filter element. In extreme cases the deflection of the porous media might even lead to a rupture. The supporting ribs in such filters are placed along the stream lines of the oil in order to reduce the resistance of the filter element. The example presented in Fig. 6.6 shows that monitoring the deflection of the porous media is also an important factor for the positioning of the rib structure.

In Fig. 6.6 we present a numerical simulation of the deformation of porous media supported by a rib structure similar to the one presented in Fig. 6.6. Comparing the two figures one can see similar qualitative behavior. To numerically obtain the displacement of the porous media we used the poroelastic plate model. Using the assumption of thickness preservation, we reconstructed the 3D porous media which we present in Fig. 6.6. On the left and right side of the domain we have used the strong clamping boundary condition to represent the strong clamping of the filter

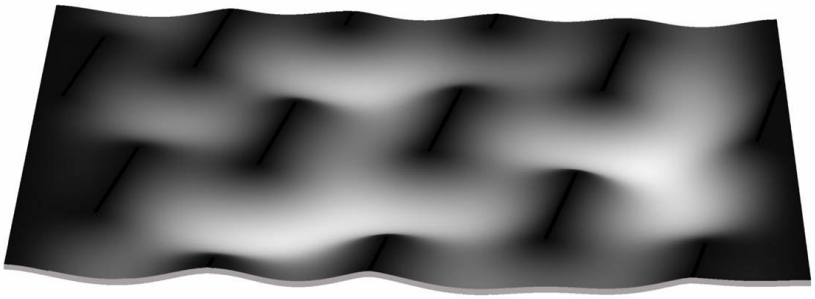

Figure 6.5: Numerical simulation of bending of a filter under extreme loading conditions

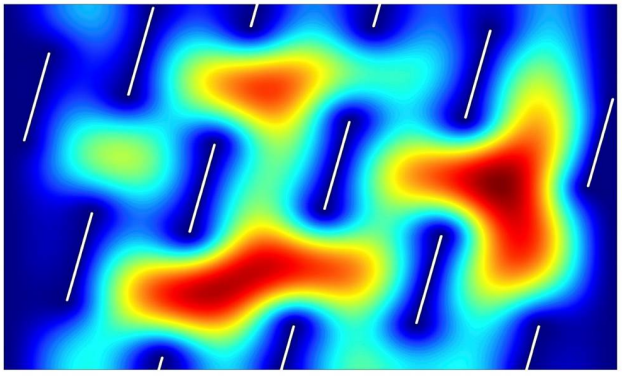

Figure 6.6: Numerical simulation of bending of a filter under extreme loading conditions. View from top

housing. In the near and further boundary of the domain we have used symmetry boundary conditions to demonstrate that we can simulate a part of the filter housing and obtain qualitatively accurate results. As the ribs support the porous media only from one side, we use weak clamping boundary conditions on the rib edges.

In Fig. 6.6 we present the displacement of the porous media by using a red to blue color legend. The red color stands for large deformation and the blue color stands for small deformation.

Fig. 6.6 shows that a nearly uniform distribution of the ribs can lead to regions with large deformation and regions with small deformation. As we use the approximate poroelastic plate model to calculate the deformation of the porous media, we obtain the numerical result within seconds. Such a fast simulation can be used by a production engineer to find a better placement for the ribs concerning the mechanical stability of the fingering media. For even further improvement of the filter operation, this fast method can be used in a multi-criteria optimization considering both the deflection of the porous media and the resistance of the ribs for the fluid flow.

The results presented in this section show how the poroelastic plate model can be used for industrial problems.

Chapter 7

Summary

This thesis provides an efficient numerical framework for the fluid-porous structure interaction (FPSI) in the context of dead-end filtration. The main contributions of this work are the following:

- Formulation of mathematical models which accurately represent the physical phenomenon of FPSI in dead-end filtration.
- Incorporation of poroelastic plate and shell models in the FPSI mathematical models.
- Development of a robust customized numerical algorithm for the mathematical models describing these FPSI problems.
- Validation of the approximate mathematical models.
- Validation of the numerical methods used to solve the mathematical models.
- Validation of the numerical framework against a physical experiment.
- Application of the numerical framework and the numerical methods for industrially relevant simulations.

In the formulation of the mathematical models for FPSI in dead-end filtration an important modeling aspect has been resolved. In previous works on FPSI modeling only flows parallel to the plain fluid-porous media interface have been considered. In this work we have posed interface conditions resolving accurately the FPSI phenomenon for flows predominantly perpendicular to this interface. Also instead of using the Darcy model, the Navier-Stokes-Brinkman system of equations has been used in order to increase the robustness and accuracy of the numerical methods based on the FPSI mathematical models.

To increase the computational efficiency for the simulations of thin filters, poroelastic plate and shell models have been incorporated in the mathematical models. It should be noted that this work is also the first to numerically validate the poroelastic plate and the linearly elastic shell models against the governing Biot's system. We have demonstrated the benefits of the approximate models and also their limitations.

In the comparison with physical experiments we have shown the mathematical models and the numerical algorithms to be accurate in the simulation of real-life systems. We have demonstrated how the FPSI numerical framework can be used to identify the mechanical properties of a saturated porous media, which is an important practical application. We have also demonstrated the increase in the filter simulation accuracy when the filter deformation is accounted for. We have shown how the grid generation techniques developed in this work and the numerical algorithms we use can be applied in the simulation of pleated and initially flat industrial filters.

Due to the advanced modeling and numerical techniques used in this work, the resulting FPSI framework is robust and computationally efficient.

The boundary- and interface- capturing Navier-Stokes-Brinkman solver we use is limited to 2D. The work in this thesis can be extended by adding 3D functionality to the flow solver. In a general 3D geometry, a general linearly elastic shell should be used instead of the cylindrical elastic shell we have presented. The grid generation techniques developed in this work can be used to create 3D grids for filters with cylindrical symmetry. Such a development of a general 3D framework would allow for accurate simulations of filters which incorporate non-symmetrical inlets and outlets.

Another way to further develop the studies of this thesis is to include equations describing the particle deposition in the FPSI framework. The deformation of the filter takes very short time. Thus, it has a clear effect on the fluid flow and therefore on the deposition of particles. For long periods of time the deposition of the contaminant on the filter can lead to a change in the fluid flow. Thus, for more accurate long-time simulations of dead end filters, a two-way coupling between the filter deformation and the particle deposition should be included.

Nomenclature

Ω	total computational domain
$\partial\Omega$	the external boundary of Ω
$\Omega_p, \tilde{\Omega}_p$	porous media domain before and after deformation, respectively
$\partial\Omega_p, \partial\tilde{\Omega}_p$	the boundaries of Ω_p and $\partial\tilde{\Omega}_p$, respectively
$\Omega_f, \tilde{\Omega}_f$	free fluid flow domain before and after deformation
$\partial\Omega_{pf}, \partial\tilde{\Omega}_{pf}$	fluid-porous structure interface respectively before and after deformation
$\hat{\Omega}_p$	the middle surface of porous media
$\partial\hat{\Omega}_p$	the boundary of $\hat{\Omega}_p$
Γ_{weak}	part of $\partial\hat{\Omega}_p$ with supported weakly
Γ_{strong}	part of $\partial\hat{\Omega}_p$ with supported strongly
Γ_{symm}	symmetrical part of $\partial\hat{\Omega}_p$
T	mapping of Ω_f on $\tilde{\Omega}_f$
F	gradient of the mapping T
$\tilde{\mathbf{v}}_f$	fluid velocity in the deformed configuration
$\tilde{p}_f$	fluid pressure in the deformed configuration
μ	dynamic viscosity of the fluid
$\bar{\mu}$	effective dynamic fluid viscosity in the porous region
ρ	fluid density
t	time variable
$\tilde{\Gamma}_{wall}$	no-slip boundary
$\tilde{\Gamma}_{in}$	inlet boundary
$\tilde{\Gamma}_{out}$	outlet boundary
K	permeability of the porous domain
σ_p	stress tensor of a porous material
$\mathbf{u}_p$	vector of displacements in the porous media
p_p	effective pore pressure in the porous media
$\hat{\lambda}$	first Lamé constant
$\hat{\mu}$	second Lamé constant
α	effective stress coefficient
β	the inverse of the Biot's modulus
$\mathbf{x}$	a point in Ω

$\mathbf{n}$	normal vector
$S(\mathbf{x})$	given vector function
$P(\mathbf{x})$	given scalar function
I	identity operator or identity matrix
$Oxyz$	orthonormal coordinate system
x, y, z	point components in $Oxyz$
$\bar{z}$	rescaled z-component
h	thickness of the porous media
ε	a small parameter
θ	rotation of the line, perpendicular to the middle surface of a 2D elastic or poroelastic media
u	tangential component of the displacement of the middle surface of a 2D elastic or poroelastic media
w	normal component of the displacement of the middle surface of a 2D or 3D elastic or poroelastic media
b	curvature
L	length of the middle line in a cylindrically symmetric poroelastic media
ϕ	test function for θ
ψ	test function for u
ζ	test function for w
H	Hilbert space in which the test functions ϕ, y and z are defined in the case of poroelastic shell
$\hat{H}$	Hilbert space in which the test function z is defined in the case of the poroelastic plate
$\rho(\theta, u, w)$	function describing flexural deformation
$\gamma(u, w)$	function describing membrane deformation
$\tau(\theta, u, w)$	function describing shear deformation
$f_{0,1}(\phi, y, z)$	effective boundary loads and mass forces in the elastic shell model
σ_f	stress tensor in the plain fluid domain
σ_{f+}, σ_{f-}	stress tensor in the plain fluid domain on the positive and negative interface, respectively
$\mathbf{n}_+, \mathbf{n}_-$	normal vector on the positive and negative interface
$\mathbf{t}_+, \mathbf{t}_-$	tangential vector on the positive and negative interface
$p_0^{1,2}, p_e^{1,2}$	rescaled interface loads in the elastic shell model
$q_0^{1,2}, q_e^{1,2}$	rescaled effective mass forces in the elastic shell model
D	flexural rigidity
B	elasticity parameter
N	effective stress resultant
M	bending momentum
ν	Poisson's ratio
x_i	point in a regular grid

n	number of points in a regular grid
θ_i, u_i, w_i	approximation in x_i for θ, u and w, respectively
a_i	approximation of b in x_i
$\left(p_{0,e}^2\right)_i$	approximation of p_0^2 and p_e^2 in x_i
Γ_0	$\Gamma_{weak} \cup \Gamma_{strong}$
Γ_n	$\Gamma_{strong} \cup \Gamma_{symm}$
Γ_{n2}	$\Gamma_{weak} \cup \Gamma_{symm}$
Γ_1	boundary under load
Γ_2	boundary under no load
r	radius of a circular domain
$\overline{w}$	analytical solution for w
$\hat{L_2}$	L_2 norm
$\hat{L}_\infty$	L_∞ norm
Q	total fluid discharge
A	surface area
p_p^+	effective pore pressure on the inlet side of the porous media
p_p^-	effective pore pressure on the outlet side of the porous media
N_{total}	total number of grid cells
p_{max}	maximal numerical pressure
p_{min}	minimal numerical pressure
E_{rel}	relative error

Acronyms

FPSI	Fluid-Porous Structure Interaction
FSI	Fluid-Structure Interaction
NURBS	Non-Uniform Rational B-Splines
ALE	Arbitrary Lagrangian Eulerian
FDM	Fictitious Domain Method
FV	Finite Volume
FD	Finite Difference
FEM	Finite Element Method
MPFA	Multi- Point Flux Approximation
MUMPS	Multifrontal Massively Parallel Sparse
GMRES	Generalized Minimal Residual

Bibliography

[1] Farhat C, Lesoinne M, Tallec P (1998), Load and motion transfer algorithms for fluid/structure interaction problems with non–matching discrete interfaces: Momentum and energy conservation, optimal discretization and application to aeroelasticity, Computer Methods in Applied Mechanics and Engineering, Vol. 157, 95–114.

[2] Kamakoti R, Shyy W (2004), Fluid–structure interaction for aeroelastic applications, Progress in Aerospace Sciences, Vol. 40, 535–558.

[3] Garelli L, Paz R, Stort M (2010), Fluid–structure interaction study of the start–up of a rocket engine nozzle, Computers & Fluids, Vol. 39, 1208–1218.

[4] Bazilevs Y, Calo V, Zhang Y, Hughes T (2006), Isogeometric fluid–structure interaction analysis with applications to arterial blood flow, Computational Mechanics, Vol. 38, 310–322.

[5] Loon R, Anderson, Vosse F (2006), A fluid–structure interaction method with solid-rigid contact for heart valve dynamics, Journal of Computational Physics, Vol. 217, 806–823.

[6] Bazilevs Y, Hsu M–C, Zhang Y, Wang W, Liang X, Kcamsdal T, Brekken R, Isaksen J (2010), A fully–coupled fluid–structure interaction simulation of cerebral aneurysms, Computational Mechanics, Vol. 46, 3–16.

[7] Bazilevs Y, Hsu M–C, Scott M (2012), Isogeometric fluid–structure interaction analysis with emphasis on non–matching discretizations, and with application to wind turbines, Computer Methods in Applied Mechanics and Engineering, Vol. 249, 28–41.

[8] Hsu M–C, Akkerman I, Bazilevs Y (2012), Wind turbine aerodynamics using ALE–VMS: validation and the role of weakly enforced boundary conditions, Computational Mechanics, October 2012, Vol. 50, 499–511.

[9] Lee Y–J, Jhan Y–T, Chung C-H (2012), Fluid-structure interaction of FRP wind turbine blades under aerodynamic effect, Composites Part B: Engineering, Vol. 43, 2180–2191.

[10] Kalro V, Tezduyar T (2000), A parallel 3D computational method for fluid-structure interactions in parachute systems, Computer Methods in Applied Mechanics and Engineering, Vol. 190, 321–332.

[11] Crosetto P, Deparis S, Gourestey G, Quarteroni A (2011), Parallel Algorithms for Fluid-Structure Interaction Problems in Haemodynamics, SIAM Journal on Scientific Computing, Vol. 33, 1598–1622.

[12] Richter T (2010), Numerical Methods for Fluid-Structure Interaction Problems, Universität Heidelberg.

[13] Iliev O, Kirsch R, Lakdawala Z, Rief S, Steiner K (2015), Modeling and Simulation of Filtration Processes, Currents in Industrial Mathematics, 163–228.

[14] Badia S, Quaini A, Quarteroni A (2009), Coupling Biot and Navier–Stokes equations for modeling fluid–poroelastic media interaction, Journal of Computational Physics, Vol. 228, 7986–8014.

[15] Bukač M, Yotov I, Zakerzadeh R, Zunino P (2014), Partitioning strategies for the interaction of a fluid with a poroelastic material based on a Nitsche's coupling approach, Computer Methods in Applied Mechanics and Engineering.

[16] Bukač M, Zunino P, Yotov I (2013), Explicit partitioning strategies for the interaction between a fluid and a multilayered poroelastic structure: an operator–splitting approach, arXiv:1308.4454v1 [math.NA].

[17] Temam R(1979), Navier-Stokes Equations: Theory and Numerical Analysis, AMS Chelsea Pub.

[18] Wendt J (2009), Computational Fluid Dynamics: An Introduction, Springer.

[19] Heywood J, Rannacher R, Turek S (1996), Artificial boundaries and flux and pressure conditions for the incompressible Navier–Stokes equations, International Journal for Numerical Methods in Fluids, Vol. 22, 325–352.

[20] Whilaker S (1986), Flow in porous media I: A theoretical derivation of Darcy's law, Transport in Porous Media, Vol. 1, 3–25.

[21] Guta L, Sundar S (2010), Navier–Stokes–Brinkman system for interaction of viscous waves with a submerged porous structure, Tamkang Journal of Mathematics, Vol. 41, 217-243.

[22] Iliev O, Laptev V (2004), On Numerical Simulation of Flow Through Oil Filters, Computation and Visualization in Science Computing and Visualization in Science archive, Vol. 6, 139–146.

[23] Richter T (2013), A Fully Eulerian Formulation for Fluid–Structure–Interaction Problems, Journal of Computational Physics, Vol. 233, 227–240.

[24] Biot M (1955), Theory of elasticity and consolidation for a porous anisotropic solid, Journal of Applied Physics, Vol. 26, 182–185.

[25] Biot M (1963), Theory of stability and consolidation of a porous medium under initial stress, Journal of Mathematics and Mechanics, Vol. 12, 521–542.

[26] Hanspal N, Wagnode A, Nassehi V, Wakemann R (2009), Development of a predictive mathematical model for coupled stokes/Darcy flows in cross-flow membrane filtration, Chemical Engineering Journal.

[27] Showalter R (2010), Poroelastic Filtration Coupled to Stokes Flow, Control theory of partial differential equations, Lecture Notes in Pure and Applied Mathematics, Vol. 242, 229–241.

[28] Cao Y, Gunzburger M, Xiaolong H, Hua F, Wang X, Zhao W (2010), Finite Element Approximations for Stokes-Darcy Flow with Beavers-Joseph Interface Conditions, SIAM Journal on Numerical Analysis, Vol. 47 (6), 4239–4256.

[29] Bars M, Worster M(2006), Interfacial conditions between a pure fluid and a porous medium: implications for binary alloy solidification, Journal of Fluid Mechanics, Vol. 550, 149–173.

[30] Marciniak-Czochra A, Mikelić A (2012), Effective pressure interface law for transport phenomena between an unconfined fluid and a porous medium using homogenization, SIAM: Multiscale modeling and simulation, Vol. 10 (2), 285–305.

[31] Carraro T, Goll C, Marciniak-Czochra A, Mikelić A (2013), Pressure jump interface law for the Stokes–Darcy coupling: Confirmation by direct numerical simulations, Journal of Fluid Mechanics, Vol. 732, 510–536.

[32] Naghdi P (1945), On the theory of thin elastic shells, Quarterly of Applied Mathematics, Vol. 14, 369–380.

[33] Naghdi P (1972), The theory of shells and plates, Mechanics of Solids, Vol. 2., C.Trusdell, ed. (Springer-Verlag, Berlin), 425–640.

[34] Zhang S (2001), A linear shell theory based on variational principles, Doctor of Philosophy thesis, The Pennsylvania State University.

[35] Li L, Schulgasser K, Cederbaum G (1998), Large deflection analysis of poroelastic beams, International Journal of Non-Linear Mechanics, Vol. 33 (1), 1–14.

[36] Yang X, Wang C (2007), A nonlinear mathematical model for large deflection of incompressible saturated poroelastic beams, Applied Mathematics and Mechanics, Vol. 28 (12), 1587–1595.

[37] Aavatsmark I (2007), Multipoint flux approximation methods for quadrilateral grids, 9th International Forum on Reservoir Simulation.

[38] Iliev O, Kirsch R, Lakdawala Z, Printsypar G (2014), MPFA algorithm for solving Stokes-Brinkman equations on quadrilateral grids, Finite Volumes for Complex Applications VII-Elliptic, Parabolic and Hyperbolic Problems, Springer Proceedings in Mathematics & Statistics, Vol. 78, 647–654.

[39] Taber L (1992), A theory for transverse deflection of poroelastic plates, Journal of Applied Mechanics, Vol. 59, 628–634.

[40] Taber L, Andrew P (1996), Poroelastic plate and shell theories, Mechanics of Poroelastic Media, 323–337.

[41] Marciniak-Czochra A, Mikelić A (2012), A Rigorous Derivation of the Equations for the Clamped Biot–Kirchhoff–Love Poroelastic plate, arXiv:1211.6456 [math.AP].

[42] Mikelić A, Tambača J (2015), Derivation of a poroelastic flexural shell model, arXiv:1504.06097v1.

[43] Füllenbach T, Stüben K (2002), Algebraic multigrid for selected PDE systems, Proceedings of the Fourth European Conference on Elliptic and Parabolic Problems, Rolduc (The Netherlands) and Gaeta (Italy), World Scientific, New Jersey, London, 399–410.

[44] Förster M, Kraus J (2011), Scalable parallel AMG on ccNUMA machines with OpenMP, Computer Science - Research and Development, Vol. 26, 221–228.

[45] Thum P, Guvanasen V (2013), The Algebraic Multigrid Method (AMG) for the Acceleration of Coupled Surface and Subsurface Flow and Transport Simulations, MODFLOW and MORE, Colorado School of Mines, Golden, Colorado.

[46] http://www.scai.fraunhofer.de/en/business-research-areas/nuso/products/samg.html, accessed on 01.03.2016.

[47] Argyris J, Fried I, Scharpf D (1968), The TUBA family of plate elements for the matrix displacement method, The Aeronautical Journal, Vol. 72, 701–709.

[48] Westphal T, Andrä H, Schnack E (2001), Some fundamental solutions for the Kirchhoff, Reissner and Mindlin plates and a unified BEM formulation, Engineering Analysis with Boundary Elements.

[49] Saksono P, Dettmer W, Peric D (2007), An adaptive remeshing strategy for flows with moving boundaries and fluid–structure interaction, International Journal for Numerical Methods in Engineering, Vol. 71, 1009–1050.

[50] Baaijens F (2001), A fictitious domain/mortar element method for fluid–structure interaction, International Journal for Numerical Methods in Fluids, Vol. 35, 743–761.

[51] Glowinski R, Pan T, Hesla T, Joseph D, Periaux J (2001), A Fictitious Domain Approach to the Direct Numerical Simulation of Incompressible Viscous Flow past Moving Rigid Bodies: Application to Particulate Flow, Vol. 169, 262–426.

[52] Loon R, Anderson P, Vosse F, Scherwin S (2007), Comparison of various fluid–structure interaction methods for deformable bodies, Computers & Structures, Vol. 85, 833–843.

[53] Versteeg H, Malalasekera W (1996), An Introduction to Computational Fluid Dynamics: The Finite Volume Method Approach, Prentice Hall.

[54] Chow P, Cross M, Pericleous K (1996), A natural extension of the conventional finite volume method into polygonal unstructured meshes for CFD application, Applied Mathematical Modeling, Vol. 20, 170–183.

[55] Rogers S, Kwak D, Kiris C (1991), Steady and unsteady solutions of the incompressible Navier-Stokes equations. The American Institute of Aeronautics and Astronautics Journal, Vol. 29, 603–610.

[56] Marshall J, Adcroft A, Hill C, Perelman L, Heisey C (1997), A finite-volume, incompressible Navier Stokes model for studies of the ocean on parallel computers, Journal of geophysical research, Vol. 103, 5753–5766.

[57] Drazin P, Riley N (2006), The Navier-Stokes Equations. A Classification of Flows and Exact Solutions, London Mathematical Society Lecture Note Series, Vol. 334.

[58] Dedering M, Iliev D, Iliev O, Kirsch R, Lakdawala Z, Lance M, Michard M, Mikelić A (2013), Modeling and Simulation of Fluid-Porous-Structure Interaction (FPSI) on the Filter Element Scale, Proceedings of the FILTECH 2013 Conference.

[59] Ilev D, Iliev O, Kirsch R, Lakdawala Z, Zemitis A, Starikovicius V (2014), Mathematical Modeling and Numerical Simulation of Filter Elements, Proceedings of the Conference on Fuel Filtration Shanghai 2014, 111–120.

[60] Iliev D, Iliev O, Kirsch R, Mikelić A, Printsypar G, Calo V (2015), Efficient simulations of poroelastic deformations in pleated filters, Proceedings of the FILTECH 2015 Conference.

[61] Grosjean N, Iliev D, Iliev O, Kirsch R, Lakdawala Z, Lance M, Michard M, Mikelić A (2015), Experimental and numerical study of the interaction between fluid flow and filtering media on the macroscopic scale, Separation and Purification Technology, Vol. 156, 22–27.

[62] Iliev O, Iliev D, Kirsch R (2015), On Computer Simulation of Fluid-Porous Structure Interaction Problems for a Class of Filtration Problems, Large-Scale Scientific Computing, Lecture Notes in Computer Science, Vol. 9374, 30–41.

Declaration

This thesis is submitted to the Department of Mathematics of the Kaiserslautern University of Technology for the degree of Doctor of Philosophy. It has been composed by myself and has not been submitted in any previous application for any degree.

The work presented (including data and data analysis) was carried out by the author except when specifically stated otherwise. Some results and data analysis in this thesis have been published by the author in the publications [58], [59], [60], [61] and [62]. The author has performed the poroelasticity and the FPSI numerical simulations presented in these papers.

In this work we develop and validate an efficient numerical framework for the complex multyphysical problem of fluid interacting with a thin poroelastic structure in the context of filtration processes. The efficiency of the framework is achieved by using advanced modeling and numerical simulation techniques. The validity of the framework is demonstrated by comparison with analytical and numerical solutions as well as with physical experiments

ISBN 978-3-8396-1152-4

9 783839 611524

FRAUNHOFER VERLAG